Evaluation and Repair of Existing Bridges in Extreme Environments

KOREY POUGH M.Sc.
DARION MAYHORN, M.Sc.
GARY S. PRINZ, Ph.D., P.E.
ROYCE W. FLOYD, Ph.D., P.E.

SPTC14.1-58-F

Southern Plains Transportation Center
201 Stephenson Parkway, Suite 4200
The University of Oklahoma
Norman, Oklahoma 73019

DISCLAIMER

The contents of this report reflect the views of the authors, who are responsible for the facts and accuracy of the information presented herein. This document is disseminated under the sponsorship of the Department of Transportation University Transportation Centers Program, in the interest of information exchange. The U.S. Government assumes no liability for the contents or use thereof.

TECHNICAL REPORT DOCUMENTATION PAGE

1. REPORT NO.	2. GOVERNMENT ACCESSION NO.	3. RECIPIENTS CATALOG NO.
SPTC14.1-58-F		

4. TITLE AND SUBTITLE	5. REPORT DATE
Evaluation and Repair of Existing Bridges in Extreme Environments	January 26, 2016
	6. PERFORMING ORGANIZATION CODE
7. AUTHOR(S)	8. PERFORMING ORGANIZATION REPORT
K. Pough, D. Mayhorn, G. S. Prinz, and R. W. Floyd,	
9. PERFORMING ORGANIZATION NAME AND ADDRESS	10. WORK UNIT NO.
Donald G. Fears Structural Engineering Laboratory School of Civil Engineering and Environmental Science The University of Oklahoma 303 E. Chesapeake St. Norman, OK 73019	11. CONTRACT OR GRANT NO. DTRT13-G-UTC36
12. SPONSORING AGENCY NAME AND ADDRESS	13. TYPE OF REPORT AND PERIOD COVERED
Southern Plains Transportation Center 201 Stephenson Pkwy, Suite 4200 The University of Oklahoma Norman, OK 73019	Final August 2014 – September 2016
	14. SPONSORING AGENCY CODE

15. SUPPLEMENTARY NOTES

Co-PI Organization:
Department of Civil Engineering (CVEG)
Steel Structures Research Laboratory (SSRL)
4190 Bell Engineering Center
Fayetteville, AR 72701

Matching Funds:
Oklahoma Department of Transportation SP&R 2256
University of Arkansas faculty startup funds

16. ABSTRACT

The research described in this report consisted of analysis and experimental testing of steel bridge details susceptible to fatigue and end regions of precast prestressed concrete girder ends subjected to reinforcement corrosion. Locations most affected by fatigue were identified and detailed analyses were conducted for four bridges. The Goodman fatigue evaluation showed that skewed bridge construction is more damaging to the steel cross-frame-to-girder component fatigue life than non-skewed construction. A localized pre-stressed carbon fiber reinforced polymer retrofit was developed that has the potential to extend the life of steel bridges having details susceptible to fatigue damage. Analyses and experimental testing successfully demonstrated the potential of this simple retrofit. A number of common deterioration items in the end region of girders were identified in through field investigations of precast, prestressed concrete girder bridges. A series of scaled prestressed concrete girder ends were subjected to an accelerated corrosion environment and were then comparatively shear tested with girder ends not subjected to corrosion. The results of these tests were inconclusive, but preliminarily indicated that minor corrosion did affect strand bond, but not shear capacity of these specimens.

17. KEY WORDS	18. DISTRIBUTION STATEMENT
Corrosion, Shear, Carbon Fiber Reinforced Polymer, Fatigue, Connections	No restrictions. This publication is available at www.sptc.org and from the NTIS.

19. SECURITY CLASSIF. (OF THIS REPORT)	20. SECURITY CLASSIF. (OF THIS PAGE)	21. NO. OF PAGES	22. PRICE
Unclassified	Unclassified	199	

SI* (MODERN METRIC) CONVERSION FACTORS

APPROXIMATE CONVERSIONS TO SI UNITS				
SYMBOL	**WHEN YOU KNOW**	**MULTIPLY BY**	**TO FIND**	**SYMBOL**
LENGTH				
in	inches	25.4	millimeters	mm
ft	feet	0.305	meters	m
yd	yards	0.914	meters	m
mi	miles	1.61	kilometers	km
AREA				
in^2	square inches	645.2	square millimeters	mm^2
ft^2	square feet	0.093	square meters	m^2
yd^2	square yard	0.836	square meters	m^2
ac	acres	0.405	hectares	ha
mi^2	square miles	2.59	square kilometers	km^2
VOLUME				
fl oz	fluid ounces	29.57	milliliters	mL
gal	gallons	3.785	liters	L
ft^3	cubic feet	0.028	cubic meters	m^3
yd^3	cubic yards	0.765	cubic meters	m^3
NOTE: volumes greater than 1000 L shall be shown in m^3				
MASS				
oz	ounces	28.35	grams	g
lb	pounds	0.454	kilograms	kg
T	short tons (2000 lb)	0.907	megagrams (or "metric ton")	Mg (or "t")
TEMPERATURE (exact degrees)				
°F	Fahrenheit	5 (F-32)/9 or (F-32)/1.8	Celsius	°C
ILLUMINATION				
fc	foot-candles	10.76	lux	lx
fl	foot-Lamberts	3.426	candela/m^2	cd/m^2
FORCE and PRESSURE or STRESS				
lbf	poundforce	4.45	newtons	N
lbf/in^2	poundforce per square inch	6.89	kilopascals	kPa

APPROXIMATE CONVERSIONS FROM SI UNITS				
SYMBOL	**WHEN YOU KNOW**	**MULTIPLY BY**	**TO FIND**	**SYMBOL**
LENGTH				
mm	millimeters	0.039	inches	in
m	meters	3.28	feet	ft
m	meters	1.09	yards	yd
km	kilometers	0.621	miles	mi
AREA				
mm^2	square millimeters	0.0016	square inches	in^2
m^2	square meters	10.764	square feet	ft^2
m^2	square meters	1.195	square yards	yd^2
ha	hectares	2.47	acres	ac
km^2	square kilometers	0.386	square miles	mi^2
VOLUME				
mL	milliliters	0.034	fluid ounces	fl oz
L	liters	0.264	gallons	gal
m^3	cubic meters	35.314	cubic feet	ft^3
m^3	cubic meters	1.307	cubic yards	yd^3
MASS				
g	grams	0.035	ounces	oz
kg	kilograms	2.202	pounds	lb
Mg (or "t")	megagrams (or "metric ton")	1.103	short tons (2000 lb)	T
TEMPERATURE (exact degrees)				
°C	Celsius	1.8C+32	Fahrenheit	°F
ILLUMINATION				
lx	lux	0.0929	foot-candles	fc
cd/m^2	candela/m^2	0.2919	foot-Lamberts	fl
FORCE and PRESSURE or STRESS				
N	newtons	0.225	poundforce	lbf
kPa	kilopascals	0.145	poundforce per square inch	lbf/in^2

*SI is the symbol for the International System of Units. Appropriate rounding should be made to comply with Section 4 of ASTM E380.

ACKNOWLEDGEMENTS

This report presents the results of a research project sponsored the U.S. Department of Transportation under Grant Award Number DTRT13-G-UTC36. The research was conducted through the Southern Plains Transportation Center led by University of Oklahoma. The portion of the research related to concrete bridges was performed at Fears Structural Engineering Laboratory at the University of Oklahoma and the portion related to steel bridges at the Steel Structures Research Laboratory (SSRL) at the University of Arkansas. Concrete materials were donated by Dolese Bros. in Oklahoma City. The authors would like to acknowledge additional students who worked on the project in various capacities including Troy Bowser, Connor Casey, Cameron Murray, Alexandria Stumps, and Stephen Tanksley. The assistance of Fears Lab technician Mr. Mike Schmitz was also invaluable. Although many individuals contributed to the research findings presented herein, the authors accept full responsibility for the conclusions presented.

EVALUATION AND REPAIR OF EXISTING BRIDGES IN EXTREME ENVIRONMENTS

Final Report

January 2017

Korey Pough, M.Sc., Graduate Research Assistant
Darion Mayhorn, M.Sc., Graduate Research Assistant
Gary S. Prinz, P.E., Ph.D., Assistant Professor
Royce W. Floyd, P.E., Ph.D., Assistant Professor

Southern Plains Transportation Center
201 Stephenson Pkwy, Suite 4200
The University of Oklahoma
Norman, OK 73019

TABLE OF CONTENTS

LIST OF FIGURES

LIST OF TABLES

EXECUTIVE SUMMARY

Many bridges within the United States (U.S.) are currently classified as either structurally deficient or functionally obsolete. The vast majority of bridges in the U.S. are constructed with either steel or concrete structural systems and a reinforced concrete deck. Aging or deterioration of the nation's bridge infrastructure is a significant issue that requires attention, especially for bridges subject to extreme environments and a changing climate. Causes for much of this deterioration can be attributed to two main factors, 1) corrosion, and 2) metallic fatigue, both of which work together to reduce the strength and serviceability of bridge components over time. In many cases, strengthening of the locally affected bridge components using localized retrofits is an economical and fast alternative to complete bridge replacement. The objective of this research was to increase the understanding of corrosion effects in prestressed concrete bridges and longevity of existing steel bridges subjected to corrosion induced deterioration and metallic fatigue.

The steel bridges portion of the research was conducted in two parts. Part 1 began with an investigation of common bridges types within region 6 and a selection of four distinct bridges for analysis. Next, detailed finite element models simulating all bridge connection geometries were analyzed, considering the American Association of State Highway and Transportation Officials (AASHTO) Fatigue I Load Model. Finally, stress analyses were conducted and local stress ranges were characterized to determine the location of fatigue critical connection details within each bridge. In part 2, localized fatigue retrofits capable of extending the steel component fatigue life were developed using pre-stressed carbon fiber reinforced polymer (CFRP) materials. Part 2 began with the development of the retrofit configuration, then a fatigue evaluation was conducted on the critical fatigue detail in each bridge based on the Goodman fatigue criterion and the retrofit configuration. Finally, the retrofit was tested on a welded diaphragm to girder connection detail in a laboratory experiment.

The Goodman fatigue evaluation showed that skewed bridge construction is more damaging to the steel cross-frame-to-girder component fatigue life than non-skewed construction. Using the Goodman criterion, the pre-stress force required to shift a structural detail from a state of finite fatigue life to infinite fatigue life increases linearly with the applied stress range; however, the magnitude of the pre-stressing force is dependent

on the size of the steel member cross-section. Laboratory tests were successful in shifting the mean stress in an instrumented steel beam using the localized pre-stressed CFRP retrofit. Although this experiment only provides a preliminary evaluation of the retrofit performance, the results indicate that the retrofit is capable of reducing the mean stress of structural details therein improving fatigue performance.

The concrete portion of this research project was divided into two sections: lab experiments and field inspections. Lab experiments to accelerate corrosion in end regions of half-scale AASHTO Type II girders that replicate girders from a bridge taken out of service in 2013 (I-244 bridge over the Arkansas River in Tulsa County) were conducted. Nine girders were constructed with an emphasis on consistency with the original design and engineering properties. One end region of each girder was exposed to an accelerated corrosion process. Three different levels of corrosion exposure were applied to the nine girders to illustrate varying environmental conditions. Six of the girders were shear tested with end zone deterioration. Shear tests resulted in measured shear values less than the design shear capacity for each girder. The corroded ends of the members exhibited larger measured shear strengths for the conditions tested. The exact significance of these results is unclear, and further research including additional deterioration levels is necessary. All of the shear failures included the effects of strand slip and the tests of corroded ends indicated that strand slip occurred prior to cracking, while the tests of the control ends indicated cracking prior to strand slip. This result indicates that corrosion may affect bond of the prestressing steel to concrete.

Concurrently with the lab experiments, efforts were placed on inspecting similar bridges to those used in the research project (bridges with AASHTO Type II prestressed girders constructed in the 1960s and 1970s) to identify varying levels of visible corrosion deterioration. During the inspections, various deterioration characteristics were found at multiple sites. Those deterioration characteristics included: corroded bearing plates; corroded anchor bolts and nuts; spalling above the support; exposed rebar and prestressing strands; diagonal cracking of the back corner of the girder; vertical cracking along the girder and diaphragm interface; diagonal cracking from the top flange and web interface; and diaphragm deterioration. These common deterioration characteristics did not appear to correlate directly with the superstructure ratings.

1. INTRODUCTION

1.1. OVERVIEW

Many bridges within the United States (US) are currently classified as either structurally deficient (due to deterioration) or functionally obsolete (due to inconsistencies between past and present code requirements). A structurally deficient status may describe a bridge that has corroded elements or contains a structural defect (such as a crack) that requires repair. A functionally obsolete status describes the nature of a bridge in today's society. This status may be given to a bridge that contains narrow shoulders or lane widths, inadequate clearance for oversize vehicles, or does not meet current load carrying requirements. Of the more than 607,000 total US bridges, approximately 30% are currently classified as either structurally deficient or functionally obsolete (NACE, 2012).

The vast majority of bridges in the US are constructed with either steel or concrete structural systems and a reinforced concrete deck. The status of steel bridges found within region 6 (Arkansas, Oklahoma, Louisiana, New Mexico, and Texas) of the Federal Highway Administration (FHWA) is similar to this national trend. Figure 1-1 (a) shows the count and percentage of highway steel bridges within region 6 that are currently classified as structurally deficient, functionally obsolete, or not deficient and Figure 1-1(b) provides a more detailed breakdown by FHWA region 6 states. From Figure 1-1(b) the majority of steel bridges within Oklahoma classify as either structurally deficient or functionally obsolete (over 3100 of the total 4869 bridges). Arkansas has over 1000 steel bridges classified as either deficient or obsolete. Figure 1-2 shows similar information for concrete bridges in region 6. The percentage of structurally deficient and functionally obsolete concrete bridges is smaller than for steel bridges, but will increase as bridges continue to age. It should be noted that while a there are significantly more concrete bridges in region 6, a large number of these bridges are culverts. It should also be noted that the data in Figures 1-1 and 1-2 were collected from the National Bridge Inventory (NBI) database [1], which archives U.S. bridge information provided by state agencies. All data available in the NBI database were collected from each state Department of Transportation (DOT) in 2012, indicating that estimations of structurally deficient bridges may be

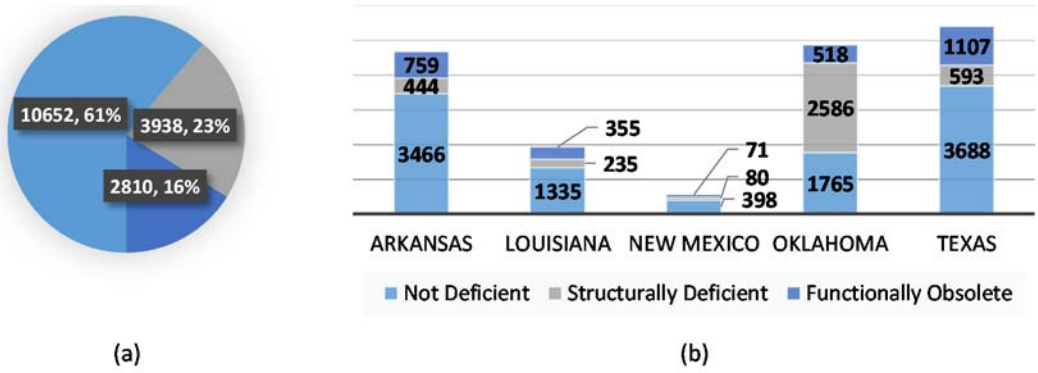

Figure 1-1: Status of steel highway bridges in region 6 (a) overall and (b) by state

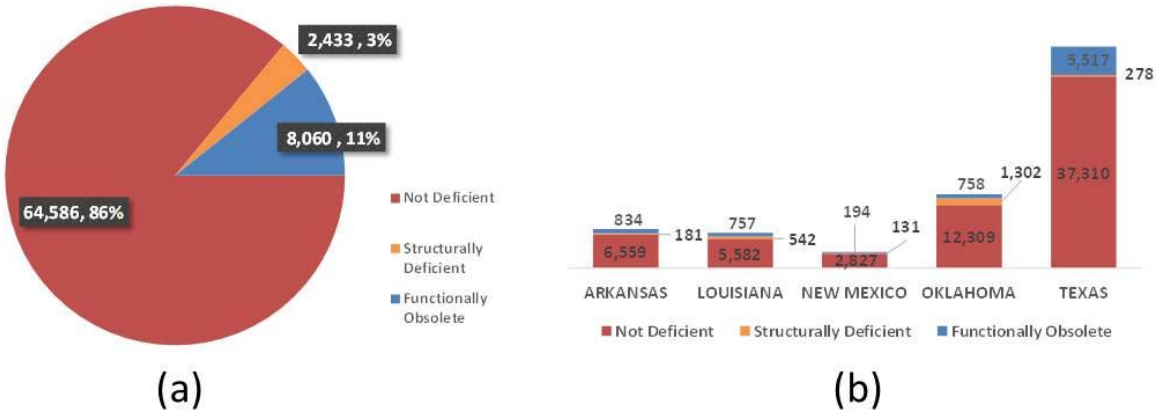

Figure 1-2: Status of concrete highway bridges in region 6 (a) overall and (b) by state

non-conservative. Only highway bridges are considered in this research (pedestrian and railway bridges are not included in the compiled data).

Along with natural impacts to our infrastructure, nationwide, it is simply aging. Much of the infrastructure was constructed over 65 years ago, and is now nearing the end of its expected design life. Increased scrutiny on public spending, along with the magnitude of concerns (i.e., deterioration of, and increased demand on infrastructure), creates a disastrous recipe when considering replacement of much of the aging infrastructure. Aging or deterioration of the nation's bridge infrastructure is a significant issue that requires attention. Causes for much of this deterioration can be attributed to two main factors, 1) corrosion, and 2) metallic fatigue, both of which work together to reduce the strength and serviceability of bridge components over time. As a result, many

steel bridges are nearing or have reached their design fatigue lives, with cracks either existing or nearing initiation. In many cases, strengthening of the locally affected bridge components using localized retrofits is an economical and fast alternative to complete bridge replacement; however, such retrofits must be resilient to further corrosion and fatigue damage.

The objective of this research is to increase the understanding of corrosion effects in concrete bridges and longevity of existing steel bridges subjected to corrosion induced deterioration and metallic fatigue. The work is broken into segments focused on concrete and steel bridges independently, then tied back together in the conclusions. The steel portion of the work was accomplished by developing corrosion resistant retrofits using pre-stressed Carbon Fiber Reinforced Polymer (CFRP) materials to reinforce critical fatigue locations within steel components. CFRP is a promising retrofit material due to its strength to weight ratio, fatigue performance, and corrosion resistance. The concrete portion of the work was accomplished through experimental tests of prestressed concrete beams subjected to a corrosive environment and inspections of in-service bridges exhibiting corrosion damage.

1.2. STEEL BRIDGES

The steel portion of the research was conducted in two parts. Figure 1-3 shows a flow chart of the research plan. In part 1 (Figure 1-3(a)), fatigue critical zones within common steel bridge components are identified and analyzed. Part 1 begins with an investigation of common bridges types within region 6 and a selection of four distinct bridges for analysis. Next, detailed finite element models simulating all bridge connection geometries are analyzed, considering the American Association of State Highway and Transportation Officials (AASHTO) Fatigue I Load Model. Finally, stress analyses are conducted and local stress ranges are characterized to determine the location of fatigue critical connection details within each bridge. In part 2 (Figure 1-3(b)), fatigue retrofits capable of extending the steel component fatigue life are developed using pre-stressed CFRP materials. Part 2 begins with the development of the retrofit configuration. Next, a fatigue evaluation is conducted on the critical fatigue detail in each bridge based on the Goodman fatigue criterion and the retrofit configuration. Finally, the retrofit is tested on a welded diaphragm to girder connection detail in a laboratory experiment.

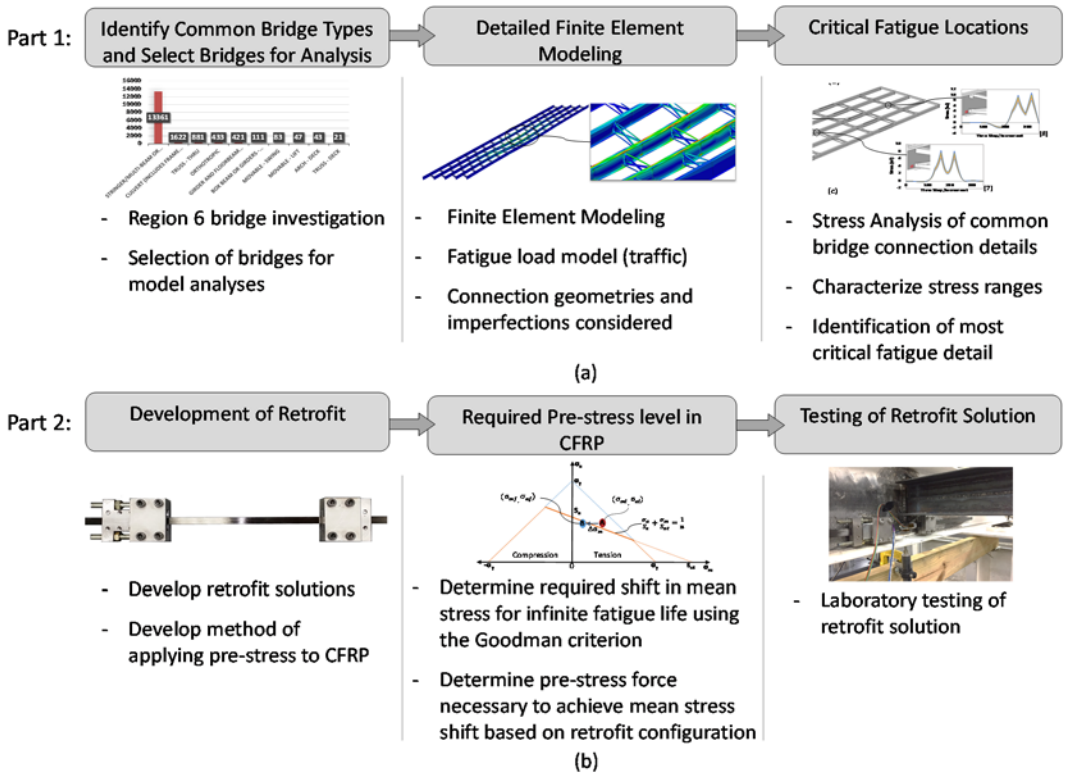

Figure 1-3: Description of steel bridge research plan (a) Part 1: Identify fatigue critical zones (b) Part 2: Develop retrofit solutions

1.3. CONCRETE BRIDGES

The concrete portion of this research project is divided into two sections: lab experiments and field inspections. Lab experiments to accelerate corrosion in girder end regions of prestressed concrete girders took place over the course of the research project. The prestressed girders used were approximately half-scale AASHTO Type II girders that replicate girders from a bridge taken out of service in 2013 (I-244 bridge over the Arkansas River in Tulsa County) and tested by other graduate students in the research group. This bridge was representative of a large number of aging bridges in the state of Oklahoma. Two different girder designs were examined, corresponding to the different prestressing strand configurations used in the bridge. Nine girders were constructed with an emphasis on consistency with the original design and engineering properties. One end region of each girder was exposed to an accelerated corrosion process. Three different levels of corrosion exposure were applied to the nine girders to illustrate varying environmental conditions (e.g., 2 months of exposure to two girders to be tested in the deteriorated state and one to be retrofitted in a later effort). Six of the

girders were shear tested with end zone deterioration, and a retrofit of fiber-reinforced polymer sheets was considered for the remaining three girders. For the six girders tested, the shear testing helps provide an understanding of the effects of end region deterioration on strand anchorage and shear capacity. Concurrently with the lab experiments, efforts were placed on visiting and inspecting similar bridges to those used in the research project (prestressed concrete bridges with AASHTO Type II girders constructed in the 1960s and 1970s) to identify varying levels of visible deterioration due to corrosion. Together, the observations from the field inspections and the lab experiments were used to analyze the effects of corrosion on ends of precast, prestressed concrete girders to inform recommendations for in-situ rehabilitation based on the level of deterioration.

For prestressed concrete girders, the end zones play an integral part in the overall function of the design. In the end zones of pretensioned girders, the load is transferred to the beam through bond between the prestressing strands and the concrete. This force distribution process, coined the prestress transfer, requires higher concentrations of mild steel reinforcement in the end zone region to resist bursting stresses resulting from the prestress transfer as well as high shear loading. Along with being important for the prestress transfer process, the end zone region is subjected to the largest shear demand. Finally, the end zone regions are subjected to high compressive stress resulting from the prestressing force, specifically areas past the transfer length where the full prestress is applied, since the moments due to dead load in these regions are small.

Bridges designed 30-50 years ago typically used the AASHTO Standard Specifications to design prestressed girders. In the past, AASHTO recommended a “quarter-point rule” for shear design, which often produced a potentially less conservative design than the current specifications. The “quarter-point rule” considered the critical section for shear to be at one quarter (1/4) of the span length, and all sections between the end and the quarter-point were designed using the applied shear from the quarter-point. The current AASHTO Load and Resistance Factor Design (LRFD) Specifications are more conservative and specify that the critical section for shear be closer to the supports than the quarter-point of the span, at d_v, the effective shear depth from the face of the support. This change in design codes has a large impact on shear demand from the quarter span point to the nearest end. Thus the adequacy of the end

zone regions of older bridges for shear is influenced by the previous, less conservative design code. Prestressed concrete girders require high percentages of mild steel reinforcement in girder end zones to resist shear loading and bursting stresses from the prestress transfer. These regions are particularly important because any damage in this region could have a lasting impact on the girder's overall strength, including shear capacity. The girder end zone region's high percentage of steel provides more susceptibility to corrosion since this region is often near the joints of the bridge deck which provides a path for seepage and chlorides from deicing salts to reach the girder ends.

Along with natural impacts to our infrastructure, nationwide, it is simply aging. Much of the infrastructure was constructed over 65 years ago, and is now nearing the end of its expected design life. Increased scrutiny on public spending, along with the magnitude of concerns (i.e., deterioration of, and increased demand on infrastructure), creates a disastrous recipe when considering replacement of much of the aging infrastructure. In order to still be effective in maintaining the infrastructure, planners are looking at rehabilitation as a viable option.

2. LITERATURE REVIEW

2.1. FATIGUE IN STEEL BRIDGES AND REVIEW OF AASHTO SPECIFICATION

Fatigue is a phenomenon wherein a material is weakened due to repeated loading. The stresses that develop as a result of these repeated loads cause cracks that, as the repeated load conditions persist, can propagate to a critical size and cause structural failure. Bridges are common civil engineering structures that are prone to fatigue cracking. Fatigue is a significant concern, and component failure can result from applied stresses far below the static strength of the component materials.

Fatigue performance is controlled by the presence of pre-existing cracks or crack-like discontinuities, which often occur at welded connections or other areas of stress concentration [2]. As a result, the crack initiation phase often takes little or no time during the structure lifespan. While early steel bridges were constructed using built-up bolted or riveted connections, in the 1950's welding became a more popular bridge fabrication method due to ease of construction and its ability to create a rigid joint between elements. However, welding had two primary concerns regarding fatigue

strength: 1) Welding introduces a more severe initial crack situation than bolting or riveting due to more critical stress concentrations and flaws [2]; and 2) The continuity between structural elements makes it possible for a crack in one element to propagate into an adjoining element [2]. Common bridge details that are susceptible to fatigue are identified in the specification for the design of steel bridges prepared by the American Association of State Highway and Transportation Officials (AASHTO) (AASHTO, 2012).

Common bridge components and details that are prone to fatigue cracking are grouped into eight categories called detail categories. Each detail category (A, B, B', C, C', D, E, and E') contains a unique fatigue tolerance based on the expected loading conditions. The AASHTO (2012) fatigue consideration specifies that each bridge detail must satisfy Equation 2-1:

$$\gamma(\Delta f) \leq (\Delta F)_n \qquad \text{Equation 2-1}$$

where γ is the fatigue load factor; (Δf) is the nominal live load stress range due to the passage of a fatigue truck; and $(\Delta F)_n$ is the nominal fatigue resistance. A fatigue load factor (γ) of 1.5 is used for Fatigue I load combinations (infinite fatigue life) while 0.75 is used for Fatigue II load combinations (finite fatigue life).

The nominal fatigue resistance $(\Delta F)_n$ is calculated based on the fatigue load combination for either infinite life (Equation 2-2) or finite life (Equation 2-3).

$$\text{Fatigue I:}\quad (\Delta F)_n = (\Delta F)_{TH} \qquad \text{Equation 2-2}$$

$$\text{Fatigue II:}\quad (\Delta F)_n = \left(\frac{A}{N}\right)^{\frac{1}{3}} \qquad \text{Equation 2-3}$$

$(\Delta F)_{TH}$ in Equation 2-2 is the constant amplitude fatigue threshold or fatigue limit. This value represents the allowable stress range for more than two million load cycles on a redundant load path structure. A bridge detail that experiences a stress range below this value will theoretically provide an infinite fatigue life. The constant A is specific to the detail category. Values for the constant A and $(\Delta F)_{TH}$ are given in Table 2-1 while N is the number of expected load cycles and is given by Equation 2-4.

$$N = (365)(75)n(ADTT)_{SL} \qquad \text{Equation 2-4}$$

In Equation 2-4, n is the number of stress cycles per truck passage; the value of n is given in the AASHTO specifications and is dependent upon span length and distance

Table 2-1: Constant A and $(\Delta F)_{TH}$ for AASHTO detail categories. (AASHTO, 2012)

Detail Category	Constant A, times 108 (ksi)	$(\Delta F)_{TH}$ (ksi)
A	250.0	24.0
B	120.0	16.0
B’	61.0	12.0
C	44.0	10.0
C’	44.0	12.0
D	22.0	7.0
E	11.0	4.5
E’	3.9	2.6

along the span. $(ADTT)_{SL}$ is the single-lane average daily truck traffic. Equation 2-3 is shown graphically in Figure 2-1 for each detail category.

The horizontal sections of the curves provided in Figure 2-1 represent the fatigue threshold $(\Delta F)_{TH}$. Values below this threshold represent a safe stress range for the corresponding number of cycles. The fatigue design life is considered to be 75 years in the overall development of the AASHTO 2012 specifications.

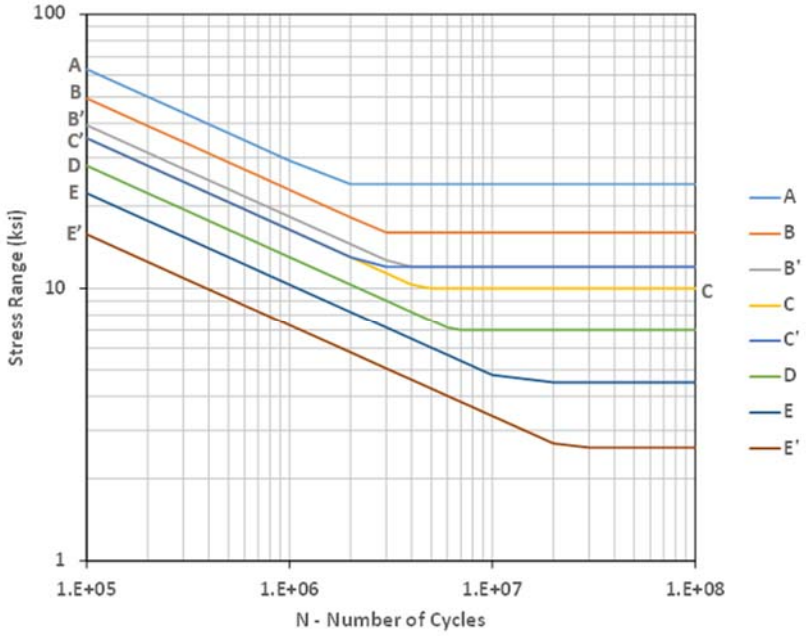

Figure 2-1: S-N Curves for each detail category

Although the current AASHTO code calls for a 75 year fatigue design life, this number has been lower in past specifications. The bridge service life was increased from

50 years to 75 years in the 1998 AASHTO specification [4]. As a result, many steel bridges in the U.S. are approaching their original design life and will need to be examined and maintained to extend their service life. Additionally, many of these bridges may be classified as functionally obsolete if its original design does not meet the current specification requirement. Figure 2-2 shows the distribution of steel highway bridges by age in region 6.

The data provided in Figure 2-2 were collected up to 2013. From Figure 2-2, nearly 70 percent of bridges within FHWA region 6 were designed for a 50 year fatigue design life (assuming that all bridges constructed before 1998, 15 years old as of 2013, were designed for 50 years). Additionally from Figure 2-2, nearly 40 percent of FHWA region 6 bridges are currently at or have exceeded their original design lives. Figure 2-3(a) shows the ages of stringer/multi-girder bridges within region 6 having a high daily truck traffic. These bridges have a functional classification of Principal Arterial as defined by the FHWA and are generally located along an interstate, freeway, expressway or another major roadway. Figure 2-3(b) shows the status of the principal arterial bridges. From Figure 2-3(a), 60 percent (40 years of age or greater) of principal arterial bridges are nearing or have exceeded their original design life. With ever increasing traffic, fatigue damage rates will likely increase.

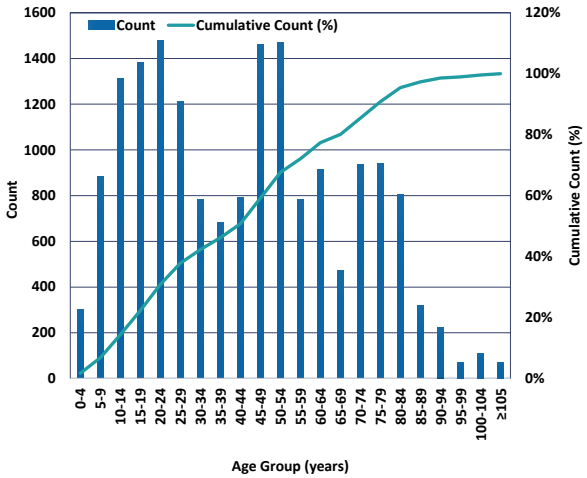

Figure 2-2: Age of steel highway bridges in region 6

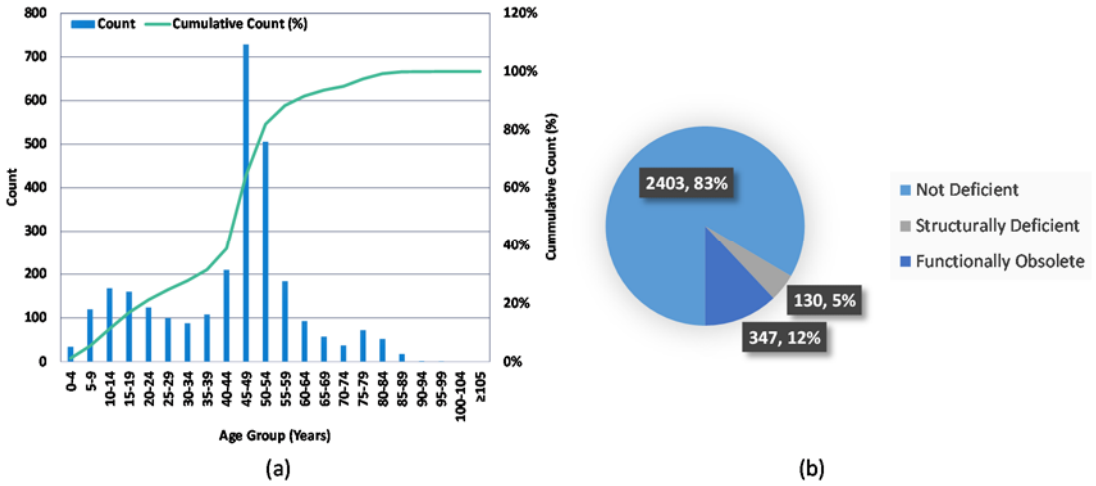

Figure 2-3: (a) Age of principal arterial multi-girder bridges in region 6, (b) status of principal arterial bridges in region 6

2.2. INFLUENCE OF CORROSION-FATIGUE

Corrosion-fatigue is simply characterized as fatigue in a corrosive environment. The combined influence of alternating stresses and an aggressive environment causes fatigue failure to occur at lower stress ranges and a lower number of cycles than fatigue in non-corrosive environments [4]. Figure 2-4 shows two S-N curves for a typical metal in both air and seawater. In a corrosive environment the stress level associated with infinite life is lowered or completely removed; therefore there is no fatigue limit in a corrosion-fatigue setting.

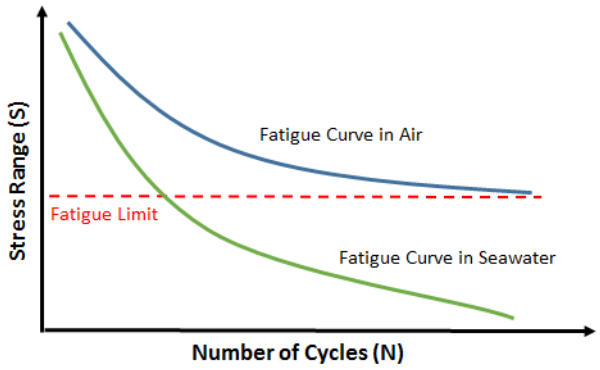

Figure 2-4: S-N Curve for typical metal in air and in seawater.

Corrosion fatigue damage typically accumulates in four stages: (1) cyclic plastic deformation, (2) micro-crack initiation, (3) small crack growth to linkup and coalescence, and (4) macro-crack propagation [4]. The damage mechanisms associated with corrosion fatigue are dependent upon a variety of metallurgical and environmental (thermal and chemical) factors (hydrogen embrittlement; film rupture, dissolution, etc.); however, control of corrosion fatigue can be accomplished by either lowering the cyclic stresses or reducing stress concentrations in the structural components. More information on corrosion fatigue can be found in Gangloff [4].

2.3. REVIEW OF FATIGUE RETROFIT METHODS

In order to mitigate fatigue damage, localized repair and retrofitting techniques can be used to redistribute stresses within structural components while reducing stress concentrations. Many different techniques are used to repair fatigue cracks or retrofit critical fatigue details, including weld surface treatments, hole-drilling, installation of splice plates, and post-tensioning [5]. A brief description of each of these techniques is discussed below. A more detailed discussion of other common repair and retrofit methods can be found in Dexter & Ocel [5].

2.3.1. Weld Surface Treatment

Weld surface treatments are intended to increase the fatigue resistance of un-cracked welds by improving the geometry around the weld toe. Weld surface improvements may include reshaping by grinding, gas tungsten arc (GTA) re-melting, and impact treatments as described below. When the weld surface treatment is done properly, the fatigue life can be reset, implying that the effects of fatigue damage are completely removed [5].

Grinding: Eliminates small cracks by removing (grinding away) a small amount of structural material.

Gas Tungsten Arc: Cracks are repaired by re-melting the metal along the weld without adding new filler material.

Impact Treatments: Reduces the effective tensile stress range by introducing residual compressive stress near the weld toe. Figure 2-5 shows the result of an impact treatment on a weld toe

Figure 2-5: Impact treatment and geometry improvement of a weld toe [5]

2.3.2. Hole-Drilling in Steel Components

Hole-drilling involves making a through thickness hole into a structural component at the tip of a crack to prevent propagation. The drilled hole helps to lessen the stress concentration at the crack tip by redistributing the stresses in the structural detail. Hole diameters must be large enough to successfully arrest the crack and are typically in the range of 2 in. to 4 in. for steel structures [5]. In addition to being the correct size, the hole must also be positioned properly so that the crack tip is contained. Figure 2-6 pictures the hole-drilling method and identifies the best location to position the hole.

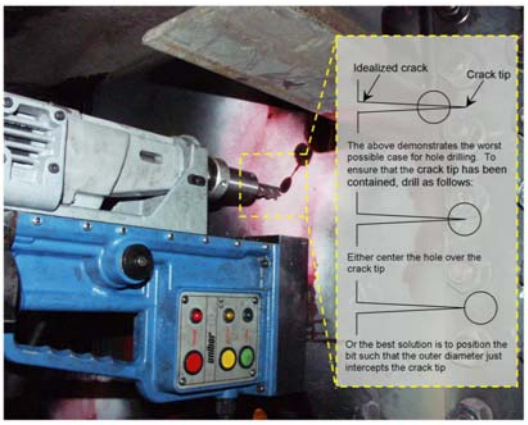

Figure 2-6: Hole-drilling and proper positioning for crack containment [5]

2.3.3. Splice Plates

Splice plates are often used as a repair method to provide continuity to a cracked section. They can also be used to restore strength to corroded elements. The concept of the splice plate is to increase the cross sectional area of a component which consequently reduces locally applied stress ranges. Figure 2-7 shows an example of a splice plate repair. The dotted line represents the crack growth beneath the splice plate while the circle shows the location of the hole drilled to remove the crack tip. Splice plates can be installed by welding or through the use of high strength bolts. According to the AASHTO specifications, a bolted connection may be considered as a category B detail, while a welded connection may result in a category D or E condition; indicating that a bolted connection has higher fatigue resistance (AASHTO, 2012).

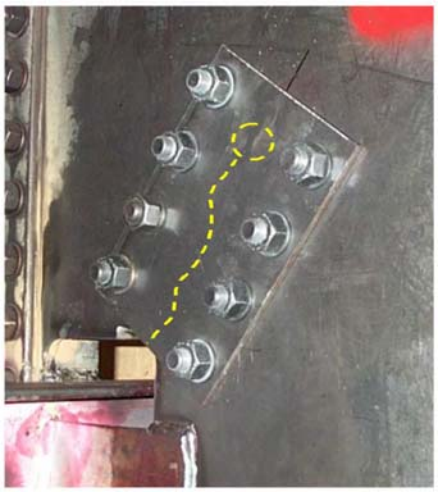

Figure 2-7: Splice plate installed using high strength bolts [5]

2.3.4. Post-Tensioning

Post-tensioning is a repair or retrofit strategy intended to reduce tensile stresses around fatigue prone regions. In order for fatigue cracks to propagate, the crack must be able to open and close as alternating stresses are applied to the structure.
Post-tensioning is a crack closure technique that introduces initial compressive stresses to an element, shifting the applied stress range into a more compressive regime.

Several options are available for applying post-tensioning forces including the use of pre-stressing strands, post-tensioning bars, or high strength threaded rods; however, proper corrosion protection must be applied to the system to ensure long term durability [5]. Post tensioning is the retrofit strategy that was used in the research described in this report using CFRP as the post-tensioned or pre-stressed material. Compared to typical post-tensioning material (strands, bars, or threaded rods) made of steel, CFRP is corrosion resistant and contains other properties that make it an ideal retrofit material.

2.4. OVERVIEW OF CFRP AND REVIEW APPLICATIONS IN STRUCTURAL RETROFITS

CFRP has a high strength-to-weight ratio which makes it viable for a wide range of applications. Several types of CFRP exist with varying elastic moduli and tensile strengths which further broadens the use of CFRP. Table 2-2 shows the five types of CFRP available. Today, CFRP is used in the development of aircrafts, automobiles, sporting goods, and infrastructure systems. In concrete structures, CFRP has proven to be an effective retrofit material by restoring the strength of weakened components. In concrete, thin CFRP sheets are often wrapped around concrete structures in order to improve tensile strength, restrict buckling, or improve the ductility of components that have lost mass due to deterioration.

Table 2-2: Types of CFRP bases on modulus of elasticity and tensile strength [6]

Type	Property	Value
Ultra High Modulus (UHM)	Modulus of elasticity:	> 65400 ksi (450 GPa)
High Modulus (HM)	Modulus of elasticity:	51000-65400 ksi (350-450 GPa)
Intermediate Modulus (IM)	Modulus of elasticity:	29000-51000 ksi (200-350 GPa)
High tensile, Low Modulus (HT)	Tensile strength: Modulus of elasticity:	> 436 ksi (3 GPa) < 14500 ksi (100 GPa)
Super High Tensile (SHT)	Tensile strength:	> 650 ksi (4.5 GPa)

CFRP use in steel structures is a more recent application and has not yet been widely used in construction. Figure 2-8 compares the stress strain curve of mild steel and CFRP. As shown in Figure 2-8, CFRP has an elastic modulus similar to mild steel but

much greater ultimate strength. This property contributes to the fatigue resistance of CFRP by enabling it to withstand greater mean stresses and stress amplitudes than steel. The corrosion resistance of CFRP makes it ideal for repair and retrofit efforts in steel structures, while its high strength to weight ratio (less than 1/3 weight of steel) allows it to add considerable strength and negligible weight to a component. One limiting property of CFRP is that it exhibits a brittle state of failure due to the lack of a well-defined yield point. In design, a safety factor is used to account for the brittle nature of the material.

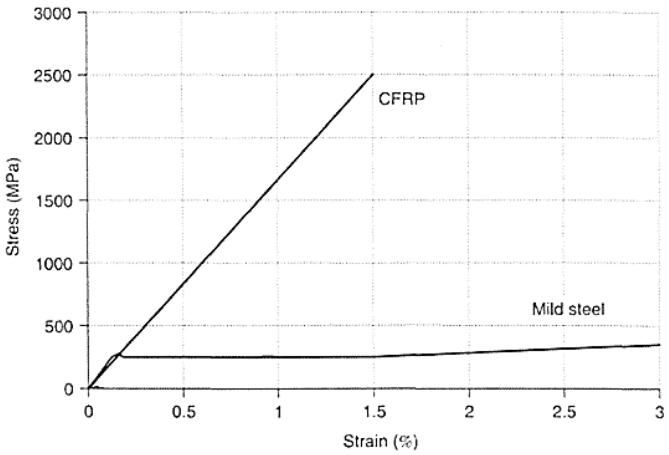

Figure 2-8: Stress-strain curve for CFRP and mild steel [7]

Although CFRP is not a commonly used retrofit material for steel structures, it has been shown to improve the flexural strength and fatigue performance of steel components in several studies [8, 9, 10, 11, 12, 13]. Flexural strengthening of steel components typically involves reinforcing tensile components subjected to bending, while fatigue strengthening involves reducing the applied stress range or mean stress in structural elements. In both cases the installation of CFRP on critical details helps to limit strains, therein reducing the stresses in structural details.

Fatigue testing is often performed under fully reversed loading with an applied mean stress of zero; however, in many real-life fatigue applications the mean stress is non zero. Some fatigue analysis procedures that account for the mean stress correction include the Goodman, Gerber, Morrow, and Soderberg models. The fatigue analysis model that will be used in this work is the Goodman approach. This method will be

discussed further in Section 3.3.2, but is demonstrated in a recent research study by Ghafoori et al. (2015). In Ghafoori et al. (2015), a riveted steel railway bridge was retrofitted with un-bonded pre-stressed CFRP plates. The retrofit system was developed where CFRP plates are eccentrically applied to the bridge girder, and a pre-stress was applied to the CFRP to shift the mean stress of the bridge component into a state of infinite fatigue life. Similar to other reported data, this study shows that applying a pre-stress to CFRP material greatly increases the effectiveness of the retrofit. CFRP pre-stress level and thickness are two key parameters that influence the performance of the retrofit.

In the research described in this report a localized retrofit using pre-stressed CFRP strips was developed to reinforce critical fatigue details within steel bridge components. As indicated in the AASHTO specifications, critical fatigue details are commonly located near welded joints. The retrofit developed in this study will focus on critical components near welded and bolted connections seen in steel stringer/multi-girder bridges within region 6.

2.5. CORROSION IN PRESTRESSED CONCRETE BRIDGES

2.5.1. Overview

For prestressed concrete girders, the end zones play an integral part in the overall function of the design. In the end zones of pretensioned girders, the load is transferred to the beam through bond between the prestressing strands and the concrete. This force distribution process, coined the prestress transfer, requires higher concentrations of mild steel reinforcement in the end zone region to resist bursting stresses resulting from the prestress transfer as well as high shear loading. Along with being important for the prestress transfer process, the end zone region is subjected to the largest shear demand. Finally, the end zone regions are subjected to high compressive stress resulting from the prestressing force, specifically areas past the transfer length where the full prestress is applied, since the moments due to dead load in these regions are small. The girder end zone region’s high percentage of steel provides more susceptibility to corrosion since this region is often near the joints of the bridge deck which provides a path for seepage and chlorides from deicing salts to reach the girder ends. These regions are particularly

important because any damage in this region could have a lasting impact on the girder's overall strength as well as shear capacity.

New bridges, though continuously exposed to the elements, are expected to last approximately 75 years. As mentioned for steel brides, this design life was previously 50 years. Many concrete bridges in region 6 have reached or will soon reach their design life. Similarly to the discussion on age of steel bridges in region 6 provided in Section 2.1, the distribution of concrete bridge age within region 6 is provided in Figure 2-9. This figure shows that nearly 70 percent of concrete bridges within FHWA region 6 were designed for a 50 year design life (assuming that all bridges constructed before 1998, 15 years old as of 2013, were designed for 50 years). Additionally from Figure 2-9, nearly 30 percent of FHWA region 6 bridges are currently at or have exceeded their original design life. An important factor in life expectancy of concrete bridges is the effect of corrosion on concrete and appurtenant embedded materials. Corrosion can quickly deteriorate a structure, causing it to lose its strength and designed purpose. Corrosion in the aforementioned end zone regions has the potential to affect shear capacity through deterioration of the concrete and affecting the transfer of prestress by decreased bonding between the strands and the concrete.

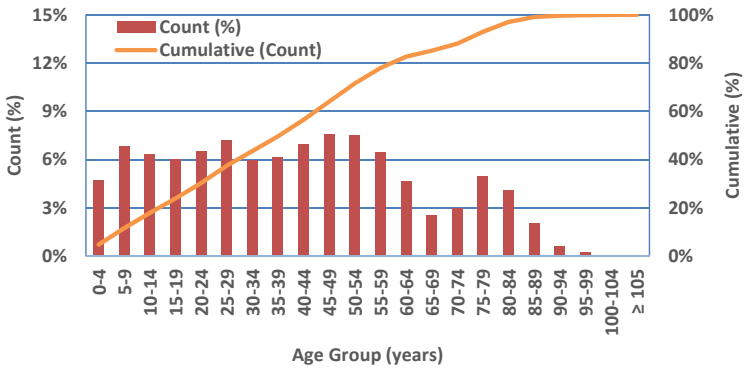

Figure 2-9: Distribution of concrete bridge age within region 6

Corrosion is the natural process by which metals are drawn to exist in their more-natural metallic compound state (e.g., oxide). In order for corrosion to take place there are three necessary components: an electrolyte, oxygen, and a material capable of supplying electrons. The reaction typically starts at the surface of the metal where a

visible aspect of corrosion typically described as rusting occurs. Once the steel embedded in concrete begins to corrode, and deteriorate, it expands since the corrosion products occupy a larger volume than the original metal. This expansion causes cracking which allows the steel to be exposed to even more elements (e.g., air, water) to further accelerate the corrosion process. Corrosion impacts the concrete member in many ways, with one being the loss of strength of the steel embedded in the concrete as it deteriorates. It is important to note that corrosion of steel occurs fastest in steel that is stressed, such as prestressing strands in a prestressed concrete beam. In order to prevent corrosion, reinforcing steel in most structures is now coated with materials (typically epoxy) to prevent, or at least, delay the corrosion process. For bridges constructed in the mid-1900s, which are now reaching their design lives, an epoxy was not applied to reinforced steel, and almost certainly never applied to prestressed strands.

For decades, engineering researchers have been developing methods to mitigate the occurrence and effects of corrosion in prestressed concrete structures. As defined by Fasl et al. [14], “corrosion is an electrochemical process that causes localized or uniform section loss in a metallic element, reducing the element’s cross-sectional area and overall strength.” Corrosion of steel in concrete, as discussed, can cause many concerns including cracking, delamination, and spalling of the concrete. In perfect conditions, the steel embedded in concrete is protected from elements causing corrosion by the alkalinity of the surrounding concrete. However, the following are major factors that influence the susceptibility of steel to corrosion: permeability of the concrete, degree of cracking, drainage, environmental conditions, surface treatment, structural geometry, concrete quality, and concrete cover [15, 16]. Loss of concrete cover and infiltration of chlorides will reduce the effectiveness of the protective alkalinity. According to Chou and Hover [17], industry and governing bodies in building codes and specifications reflect this concern by requiring concrete cover and chloride control. One major consequence of corrosion in concrete is the potential for reduction of the live load capacity. This capacity is impacted by both the reduction of the steel cross-section and loss of bonding between the concrete and steel. In a study focused on deterioration of prestressed concrete bridge beams, Bruce et al. [18] concluded that corrosion in prestressing strands reduces the structural performance of a beam faster than corrosion exhibited in conventional reinforced beams

because a larger proportion of the steel cross-section is lost. Szilard [19] emphasized that prestressing steel is also subjected to significantly higher stresses with smaller diameters in relation to conventional reinforcement.

Vu et al. [20] found that concrete cover and water-cement ratio (*w*/*c*) were good predictors for performance of chloride contaminated concrete related to cracking. The researchers found that generally “the rate of crack propagation decreases as concrete quality increases.”

2.5.2. Susceptibility of Bridges to Corrosion

Chlorides are particularly damaging for concrete and appurtenant embedded materials. Mukherjee and Rai [21] state that “corrosion of steel reinforcement, both prestressing tendons and non-prestressed rebars, caused by infiltration of de-icing agents, is one of the primary sources of a structure’s deterioration.” Song and Shayan [22] hypothesized that chlorides could be introduced to concrete through some of the following methods: use of chloride as an accelerant; use of water containing chloride, contaminated aggregates, sea salt spray; and use of chemicals and de-icing salts. A survey of bridges used in salt de-icing environments illustrated that the majority of chloride-induced corrosion over time was due to “chloride-laden water” from the bridge deck that trickled through expansion joints, cracks in the deck concrete overlay, and inadequately designed concrete cover [23]. Smith and Virmani [24] of the Federal Highway Administration noted the ability to minimize the number of deck joints as a means to reduce the availability of seepage paths for chlorides to reach a bridge’s superstructure and substructure. The report notes that “bridges as long as 850 m (2800 ft) have been constructed without joints except at the abutments” [24]. This provides evidence that the 21st century design engineer must take care to not only create a beautiful system, but one that will also stand the test of time and the environment.

While researching chloride ion distribution in 20-year-old prestressed concrete girders in Minnesota, Coggins and French [16] found that the only evidence of strand corrosion was observed at the ends of the beams. In these cases, “the mortar coating had spalled from the strand ends due to weathering or drainage at the deck joints.” They also found that chloride levels were higher on the side of interior beams facing oncoming traffic than exterior beams of the same direction through a detailed examination and performing

a chloride ion penetration analysis on samples from girders [16]. The authors concluded that girders facing oncoming traffic contained greater concentrations of chlorides since “oncoming traffic carries salts toward the bridge in a mist or spray form.” The authors attributed the exterior beam to have lower chloride concentrations due to the salts being washed away from the exposed face by rain.

2.5.3. Reduced Capacity of Corroded Members

Several recent studies have investigated the capacity of decommissioned bridge beams with corrosion damage. Rogers et al. [25] performed destructive tests on 19 decommissioned pretensioned concrete bridge beams from a 1969 bridge that had corroded pretensioned reinforcement. The researchers found that the 40-year old beams exhibited chloride-induced corrosion from sea spray. The results from the destructive tests indicated that “the most severely corroded beam sustained 69% of the load of an equivalent good-condition beam.” ElBatanouny et al. [26] found that pitting corrosion in prestressed strands caused a reduction in residual capacity in only 140 days - concluding that crack width was an important factor in “the formation and intensity of pitting in terms of pit depth.” By load testing, ElBatanouny et al. [26] found that the most corroded member had a tested capacity of 86.7% when compared to the original control specimen.

Pape and Melchers [27] found that as the degree of corrosion loss in the prestressing strands increased, the maximum capacity of the girder decreased linearly. In determining the performance of three 45-year-old corroded prestressed concrete beams, the researchers concluded that using current design theory, estimated material properties, and neglecting cracking and corrosion damage, ultimately overestimates the actual capacity of the beams. In one beam, Pape and Melchers (2013) found that a 64% loss in prestressing cross-sectional area due to corrosion at the failure location contributed to a 49% reduction in original, theoretical design capacity.

Cai and Miao [28] stated that load capacity degradation is “due to the increasing age of the structural components and the aggressive environment bridge structures are exposed to.” Abosrra et al. [29] found that the first day of corrosion acceleration caused a slight increase in steel/concrete bond strength, but after 7 and 15 days of corrosion acceleration, there was significantly reduced steel/concrete bond strength.

2.6. FACTORS INFLUENCING PRESTRESSED CONCRETE SHEAR CAPACITY

The end zones of prestressed concrete girders play an integral part of the overall function of the design. The end zone regions are where the prestress transfer from the steel to the concrete takes place. The prestress changes the stress state in the concrete, and as a result the prestress ultimately affects the shear capacity. The transfer length defines the extent of the bonding between the concrete and prestressing strands where less than the full prestress is applied to the beam. This transfer length, should it be reduced, could have adverse impacts on the shear capacity by changing the state of stress from that which was used to calculate the shear capacity at a given section. Also in the end zone regions, it is typical to have transverse steel reinforcement stirrups that provide additional shear capacity beyond that provided by the concrete. Ultimately, corrosion impacting the bonding of the prestressing strands in this region, or the deterioration of the transverse steel, can reduce the shear capacity of the girder.

2.7. EFFECT OF CRACKING AT THE END OF PRESTRESSED MEMBERS

The possibility arises for cracking at the ends of prestressed concrete during fabrication, when tensile stresses caused by the prestress force exceed the tensile strength of the concrete. A study performed for the Oklahoma Department of Transportation (ODOT) described “Y” cracking of the bottom flange to be the most serious form of end-region cracking. “Y” cracks are described as splitting cracks that “form at or near the bottom flange-web interface and are oriented vertically at the end face of the girder” [30]. Figure 2-10 shows an example of “Y” cracks on the end face of a girder.

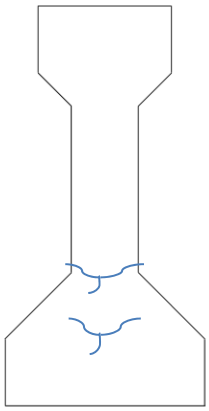

Figure 2-10: Example of "Y" cracks

The report states that “Y” cracks result from a “combination of lateral eccentricity of prestressing force and propagation of horizontal web-splitting cracks”, which “create planes of weakness adjacent to columns of prestressing steel ends in the bottom flange.” The report also states that “quantification of the increase in transfer length or corrosion of reinforcement due to end-region cracking has proven difficult, as have the in-place effects of such corrosion on structural capacity.” The literature review for this study showed that “debonding up to 25 percent of strands has the most significant effect on reducing end-region stress concentration and “Y” cracking.” The behavior of end zones is of interest, as other state DOTs are investigating cracking at prestressed girder ends [31].

The ODOT study also found that end-region cracking that parallels the prestressed reinforcement “is more likely to affect structural capacity than cracking perpendicular to the reinforcement” [30]. The authors go on to state that loss of confining bond, leads to “longer transfer length or increased strand corrosion along the crack.” Researchers found that corrosion of primary bottom prestressing strands was more likely to affect structural capacity than corrosion of draped strands or mild steel reinforcement. The greatest amount of moisture from deicing salts typically drips onto the girder end face.

2.8. METHODS TO REPAIR AND STRENGTHEN PRESTRESSED CONCRETE GIRDERS

It is particularly important for maintenance of aging infrastructure to determine rehabilitation methods for a structure when complete replacement may not be a feasible option. As stated by Cai and Miao [28], bridges are the “backbones of the highway system [and] must be maintained and preserved to ensure safety to the traveling public.” Almusallam [32] stated that the “degree of reinforcement corrosion and the resulting decrease in the load-carrying capacity of both steel bars and the structural component need to be evaluated to assess the residual strength of concrete and formulate repair strategies.” The NCHRP 654 report [33] recommends that cracks less than 0.012 inches width need not be repaired, with incremental repair strategies for cracks of widths greater than 0.012 inches. Those repair strategies could include epoxy injection and application of surface sealants. However, the NCHRP 654 report recommends “different acceptable crack widths based on severity of the bridge’s exposure conditions, with a width limit of 0.007 in. in girders subject to deicing chemicals.”

Ideally, before repair, one would want to know how to prevent an issue with their infrastructure. In general, corrosion prevention methods can be divided into electrical and non-electrical methods. Pritzl et al. [34] consider non-electrical methods to include “coatings, sealers, and corrosion inhibiting admixtures.” The researchers stated that cathodic protection is an electrical approach “that can be used to prevent corrosion by shifting the reinforcing steel into a protected state.” Pritzl et al. [34] found that “surface treatments (coatings) applied to the end zones of precast/prestressed concrete bridge girders at the time of construction can successfully prevent beam end corrosion.” Darwin et al. [35] found that methods to reduce corrosion of reinforcing steel were divided into two categories: methods that slow the initiation of corrosion, and methods that lengthen the corrosion period. Darwin et al. [35] defines the corrosion period as “the time between the initiation of corrosion and the end of service life.” The primary corrosion protection systems used for bridges have involved epoxy-coated reinforcement, and increased cover over reinforcing bars since the mid-1970s [35]. Mukherjee and Rai [21] proposed that replacing metallic reinforcement and strands with fiber reinforced polymer (FRP) materials may be a more positive solution. The researchers state that FRP material “significantly increases the bridge life” and the increased costs of the non-metallic reinforcement may be justified.

One repair material that has proven successful for repair of structural damage is FRP. Some of the major benefits of FRP include: “high strength to weight ratio, high fatigue endurance, excellent corrosion resistance, low thermal expansion, and the ease of fabrication, manufacturing, handling, and installation” [28]. FRP is available in many forms, the two most common are laminates and bars. Cai and Miao [28] found that structural systems strengthened with externally bonded FRP laminates “combine the benefits of mechanical properties of FRP composites, the compressive characteristics of concrete, and the ductility and deformation capacity of steel” – thereby improving the load capacity of the structure. A technical bulletin by the International Federation for Structural Concrete [36] discussed design advantages of using externally bonded FRP reinforcement in reinforced concrete structures. Those advantages included: delaying crack formation in the shear span, improving serviceability and durability due to reduced

cracking, improving the shear resistance of members, and achieving “greater structural efficiency as the neutral axis remains at a lower level in the prestressed case” [36].

ElSafty [37] explored the potential of carbon fiber reinforced polymer (CFRP) systems for impact-damaged girders. While ElSafty [37] was concerned with flexural capacity of impact-damaged girders, there is potential for the CFRP retrofit to improve shear capacity of girders exhibiting induced deterioration as well. ElSafty [37] concluded that CFRP systems “can be designed to restore lost flexural capacity, possibly enhance the original capacity and maintain the desired failure mode.” He concluded that the outcome of the project would contribute to “savings of millions of dollars in repairing damaged prestressed concrete girders.”

Higgins et al. [38] focused on the use of CFRP systems for increasing shear strength of reinforced concrete girders. They found that repair systems for shear using discrete CFRP strips “provided a significant increase in ultimate strength capacity compared to unrepaired members.” They also cautioned that repairing for shear using CFRP “must recognize the impact of the increased shear capacity on the flexural demands to prevent anchorage failures at poorly detailed flexural bar cutoff and anchorage locations” [38]. Higgins et al. [38] concluded that it was possible to increase a member’s shear strength using a “targeted repair approach applying CFRP material only to a critical section rather than over the entire member.” It was also concluded that the addition of longitudinal CFRP strips “did not increase shear capacity due to debonding and bending of fibers at the poorly constrained diagonal cracks” [38].

CFRP U-wraps are another potential application of CFRP material for repair. CFRP U-wraps are when the FRP is applied continuously around the sides and bottom face of the beam in a “U shape.” Ray et al. [39] suggest that CFRP U-wrapped anchors should be placed close to the initiation point of debonding so that its resistance can be activated before significant debonding has occurred. The researchers include that debonding initiates from a flexural or flexural-shear crack that forms near the load application point; the crack propagates downward at a 30 degree angle, where the U-anchor should be placed to maximize the total load-carrying capacity.

The ability to better design structures to mitigate the effects of corrosion is important. However, in order to do so, more research is necessary on prestressed

concrete and corrosion, and opportunities are needed to perform in-situ rehabilitation. The research described in this report is intended to expand on the current body of knowledge surrounding corrosion of prestressed concrete girders due to extreme environments, with particular focus on how end zone deterioration ultimately affects the girder's shear capacity.

3. ANALYTICAL INVESTIGATION INTO STEEL BRIDGE COMPONENT FATIGUE

3.1. SELECTION OF BRIDGES FOR ANALYSIS

3.1.1. Identification of Common Bridge Types

A variety of steel bridge construction types (stringer/multi-girder, truss, culvert, arch, suspension, etc.) exist within region 6; however, stringer/multi-girder construction types are the most common. Figure 3-1 shows the frequency of steel highway bridge construction types within region 6. Note that only the ten most frequent construction types are shown. Stringer/Multi-girder bridges make up 13,361 (76.7%) of the 17,400 total steel highway bridges in the region 6. With the highest quantity of constructed bridges being of stringer/multi-girder construction, and in order for the retrofits to have the greatest impact, it was decided to consider only stringer/multi-girder type constructions in this study.

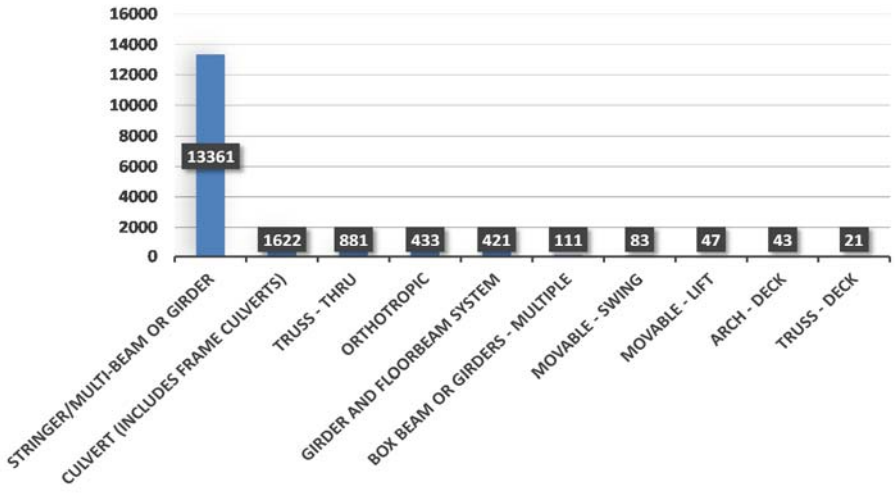

Figure 3-1: Frequency of region 6 steel highway bridge construction types

3.1.2. Chosen Designs for Study Models

Bridges chosen for this study are aimed to be representative of the stringer/multi-girder construction within region 6. Stringer/Multi-girder steel bridges can generally be classified by geometry (skew or non-skew), cross-frame configuration (diaphragm or cross-frame), and support conditions (simply supported or continuous). Four region 6 bridges containing a combination of these design features are evaluated in this work. In addition to these construction details, the selected bridges also vary in span length to determine the effect of span length on the location of critical fatigue regions. All of the selected bridges have a functional classification of principal arterial (interstate, freeway, expressway or other major roadway) to ensure that this study is relevant to bridges that are frequently travelled. Table 3-1 summarizes the construction details for each of the bridges evaluated in this study.

Table 3-1: Construction details for selected bridges.

State	Name	Length (ft)	No. Long. Girders	No. of Spans	Lanes	Cross-Frame Config.	Skew	Span Type
AR	A-3956	120	7	3 @ 40 ft	2	Diaphragm	None	Simply Supported
AR	A-3958	456	5	6 @ 76 ft	2	Diaphragm	30°	Simply Supported
TX	T-130	130	5	Cont.	2	Cross- Frame	None	Continuous
AR	A-6243	240	5	Cont.	2	Cross- Frame	44°	Continuous

Note: 1 ft = 0.3048 m

3.2. MODELING TECHNIQUES

3.2.1. Geometry/Element Type

Construction documents for each bridges evaluated in this work were provided by state DOTs within region 6. Detailed three-dimensional (3D) models simulating the geometry of each bridge were developed using ABAQUS. The global boundary conditions of the bridge models simulate the support conditions seen in the constructed bridge. Four-node linear shell elements were used to model all geometries and connection regions. Shell elements provide analytical results for the top and bottom face of each element, while solid elements provides analytical results through the thickness of the element. Shell elements were used in the analysis to reduce the computational cost.

While the simulated bridge connection regions assume a rigid (zero rotation) assembly, actual bolted connections within the bridge may act as semi-rigid joints (allowing small rotations). Bolted regions within the cross-frame configurations were excluded from all models for simplicity.

Mesh size can affect the accuracy and computational expense of the finite element analysis. Typically, smaller element size is associated with greater accuracy and higher computational expense. The general mesh size used for bridges A-3958, T-130, and A-6243 is 2 in. x 2 in. A smaller mesh size of 1 in. is used for bridge A-3956 because the girder cross-section is much smaller (W21 vs. W30, W36, and W48). These mesh sizes allow for 15 to 25 elements within the beam web height.

The bridges were analyzed statically using a linear equation solver. The linear solver uses a sparse, Gauss elimination method where the storage of equations occupies a large portion of the disk space during the calculations [40]. Table 3-2 shows the number of elements and nodes considered in the analysis, as well as the number of equations and approximate computational time necessary to complete the analysis. Not surprisingly, the computation time increases significantly as both the model size increases, and the element size decreases. Computational time was further reduced on the simply supported bridges (A-3956, and A-3958) by considering only one span length. Note that the computational time also depends on the number of processes running and the computer memory available.

Table 3-2: Number of elements, nodes, equations, and computational time for static analyses

Bridge	Span Length	Typical Element Size	No. of Elements	No. of Nodes	No. of Equations/ Unknowns	Comp. Time
A-3956	40 ft	1 in.	156,727	160,234	956,952	2.92 hrs.
A-3958	76 ft	2 in.	78,533	80,966	484,176	2.17 hrs.
T-130	130 ft	2 in.	140,190	146,008	873,528	5.50 hrs.
A-6243	240 ft	2 in.	384,814	403,546	2,377,992	31.90 hrs.

A picture and description of each bridge is given in the following, along with the bridge model showing the cross-frame configuration, and typical element mesh size used during the analysis.

Bridge A-3956

Bridge A-3956 is pictured in Figure 3-2(a). This bridge was constructed in 1968, services Interstate-540, and crosses over Flat Rock Creek near Van Buren, Arkansas. The ABAQUS model, diaphragm details and mesh size for bridge A-3956 are shown in Figure 3-2(b). Bridge A-3956 is non-skewed and carries two lanes of traffic along three simply supported spans of 40 ft each. This bridge was classified as structurally deficient in the 2013 NBI database. The seven longitudinal girders (W21x62) are spaced at 6 ft – 3 in. and contain cover plate attachments welded to the bottom flanges. Longitudinal girders are connected by one row of C shape diaphragms (C12x20.7) bolted to steel gusset plates (not-shown), then welded at the girder mid-span.

Bridge A-3958

Bridge A-3958 is pictured in Figure 3-3(a). Bridge A-3958 was also constructed in 1968. This bridge was classified as structurally deficient in the 2013 NBI database and was recently reconstructed in 2014. The analysis of this bridge is based on the design prior to reconstruction; however, the results of this study will be applicable to the many existing bridges that have an identical or similar design. The bridge services Interstate-540 and crosses over a railroad track near Van Buren, Arkansas. The ABAQUS model, diaphragm details and mesh size for bridge A-3958 are shown in Figure 3-3(b). Bridge A-3958 has a skewed geometry and carries two lanes of vehicular traffic along six simply supported spans of 76 ft each. The five longitudinal girders (W36x160) are spaced at 6 ft – 6 in. and contain cover plates attachments welded to the bottom flanges. Longitudinal girders are connected by C shape diaphragms (C15x33.9) staggered along the span. Diaphragms are bolted to steel plates (not-shown), then welded at the girder mid-span.

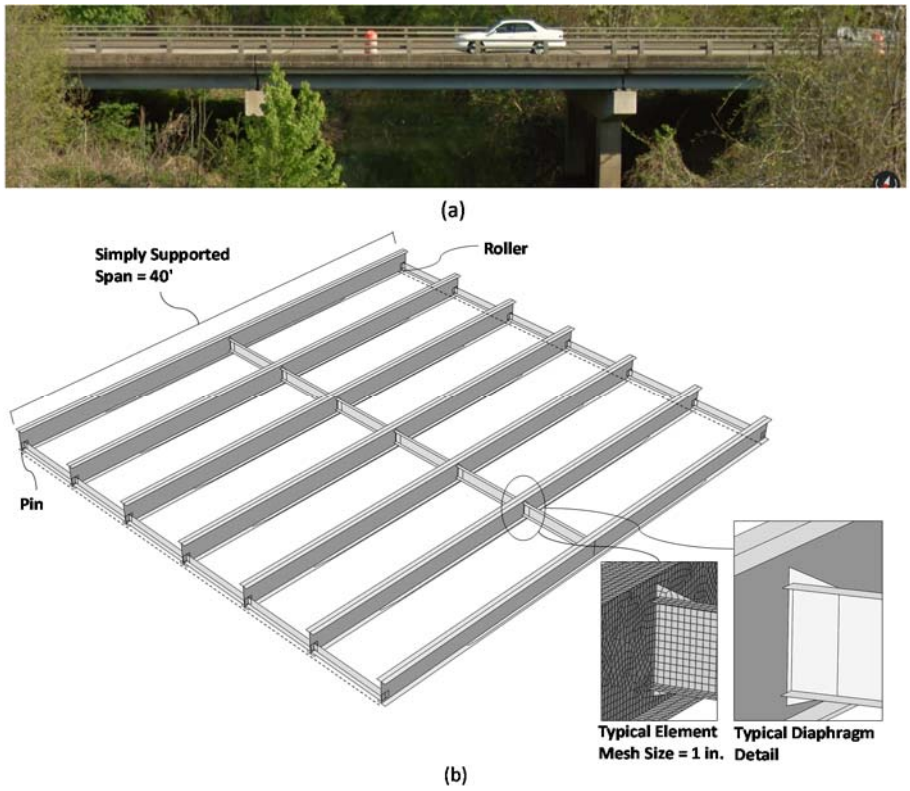

Figure 3-2: Bridge A-3956 (a) elevation picture [41] (b) ABAQUS model

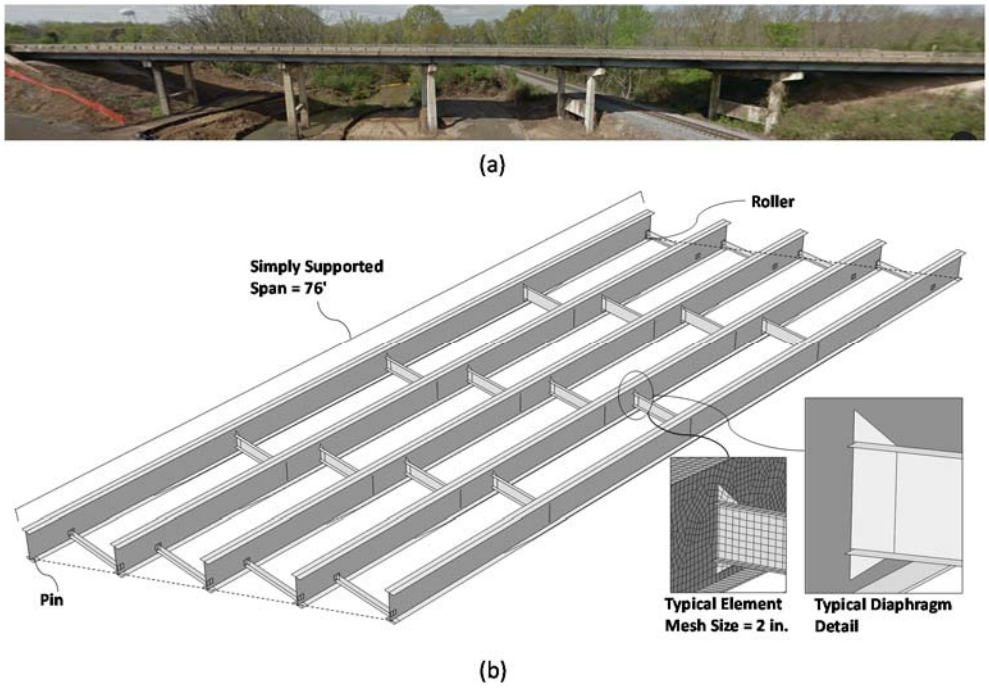

Figure 3-3: Bridge A-3958 (a) elevation picture [41] (b) ABAQUS model

Bridge T-130

Bridge T-130 is pictured in Figure 3-4(a). Bridge T-130 was constructed in 1968 and was classified as functionally obsolete in the 2013 NBI database. The bridge services Interstate-35 and crosses over Highway-56 Creek near Moore, Texas. The ABAQUS model, diaphragm details and mesh size for bridge T-130 are shown in Figure 3-4(b). Bridge T-130 is non-skewed and carries two lanes of vehicular traffic along a continuous span of 130 ft (40 ft ~ 50 ft ~ 40 ft). The bridge is pinned at the two interior supports and contains expansion shoes (rollers) on both ends of the structure. The five longitudinal girders (W30x108) are spaced at 9 ft – 0 in. and contain cover plate attachments welded to the top and bottom flanges above the interior supports. Longitudinal girders are connected by three types of cross-frames: cross-frame details A and B (shown in Figure 3-4(b)) are installed alternatively along the bridge span. The third cross-frame detail is located above the two end supports; the stresses in this detail are minimal, therefore, the close up detail is excluded from Figure 3-4(b). Cross-frame details A and B are both welded to the longitudinal girders. Detail A consists of three L-shapes welded in an “X” configuration, while detail B consists of one T-shape and three L-shapes welded in a “K” configuration.

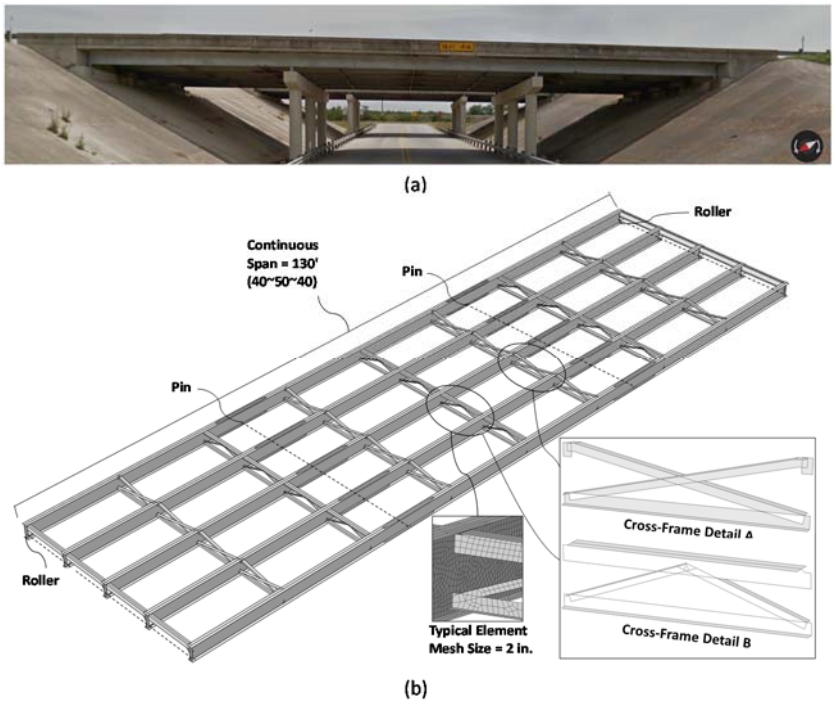

Figure 3-4: Bridge T-130 (a) elevation picture [41] (b) ABAQUS model

Bridge A-6243

Bridge A-6243 is pictured in Figure 3-5(a). Bridge A-6243 was constructed in 1994 and was given a not-deficient status in the 2013 NBI database. This bridge is located along Interstate-49 and crosses over Highway-265. The ABAQUS model, diaphragm details, and mesh size for bridge A-6243 are shown in Figure 3-5(b). The bridge has a skewed construction and carries two lanes of vehicular traffic along a continuous span of 240 ft (70 ft ~ 100 ft ~ 70 ft). The bridge is fixed at the center supports and contains expansion shoes (rollers) on both ends of the structure. The five longitudinal built-up plate girders have a web depth of 48 in., flange width of 12 in., and are spaced at 9 ft -0 in. Transverse stiffeners are welded to the web of the longitudinal girders at the location of each cross-frame. The cross-frames (shown in Figure 3-5(b)) are made up of four L-sections that are welded to gusset plates then bolted (not shown) to the web stiffeners.

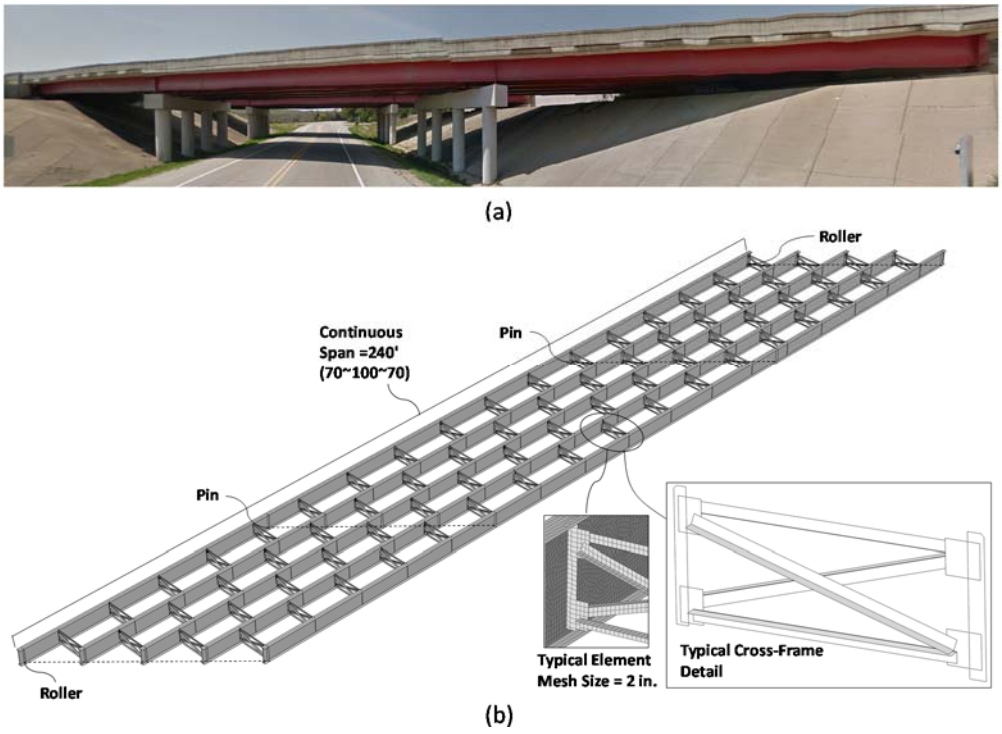

Figure 3-5: Bridge A-6243 (a) elevation picture [41] (b) ABAQUS model

3.2.2. Materials & Loading

Because the fatigue loadings occur under service loadings, elastic steel material properties are used in the ABAQUS analysis. Typical values of Young's modulus (E=29000 ksi) and Poisson's ratio (v=0.3) were considered in the model.

The AASHTO fatigue truck served as the loading condition for each of the bridge models. The characteristics of the fatigue truck are shown in Figure 3-6. The fatigue truck consists of an 8,000 lb front axle spaced 14 ft from the 32,000 lb mid axle, with the mid axle spaced 30 ft from the 32,000 lb rear axle. As indicated in the 2012 AASHTO specifications, a dynamic load allowance factor (*IM*) of 1.15 is applied to each axle weight to account for wheel load impact from moving vehicles. Additionally, a fatigue load factor (γ) of 1.5 is applied to each of the axle weights in order to analyze the bridges using the AASHTO Fatigue I load combination (infinite fatigue life) (see Section 2.1).The global models were also analyzed using hypothetical load factors of 1.65, 1.75, 1.85, and 2.0 (total of five analyses per bridge) in order to determine the effect of increased traffic loads on the local stress range and overall fatigue performance of bridge components.

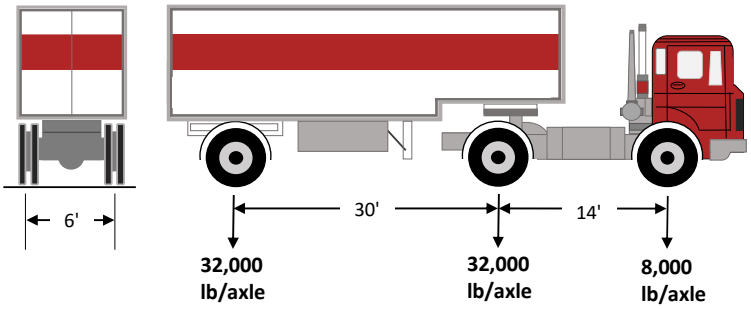

Figure 3-6: Characteristics of the AASHTO fatigue design truck HS 20-44

All of the models were loaded with the assumption that the fatigue truck was traveling in the right vehicular lane. The truck loading was divided amongst the girders supporting the traffic lane based on the tributary area of the girders. Figure 3-7 shows a schematic of the bridge lanes and girders for bridges T-130 and A-6243. As shown in Figure 3-7, the truck travels between girders C and D when driven in the right lane. Based on the tributary area for each girder, the wheel loads were divided equally between girders C and D in the ABAQUS model. Note that bridges A-3956 and A-3958 have a

different lane layout and girder spacing, therefore, the load is applied differently. All of the bridges have a lane width of 12 ft, however, bridges A-3956 and A-3958 have a girder spacing of 6 ft – 3 in. and 6 ft – 6 in. respectively. Due to the smaller girder spacing and the change in bridge layout, the right traffic lane is supported by three consecutive girders. Based on this configuration, the middle of the three girders carries twice the load (1/2 of axle weight) of the outer two girders (1/4 of axle weight each).

Sequences of statically applied loads simulate the truck passage along the bridge span. Figure 3-8 shows the truck wheel loading scheme used in the ABAQUS models. Vertical loads corresponding to the individual wheel loads are activated and deactivated in series to simulate a moving load. The process of activating and deactivating are overlapping such that the ramping up coincides with the ramping down of the previous load. The load increments are spaced at 6 in. along the entire bridge span for all of the bridge models.

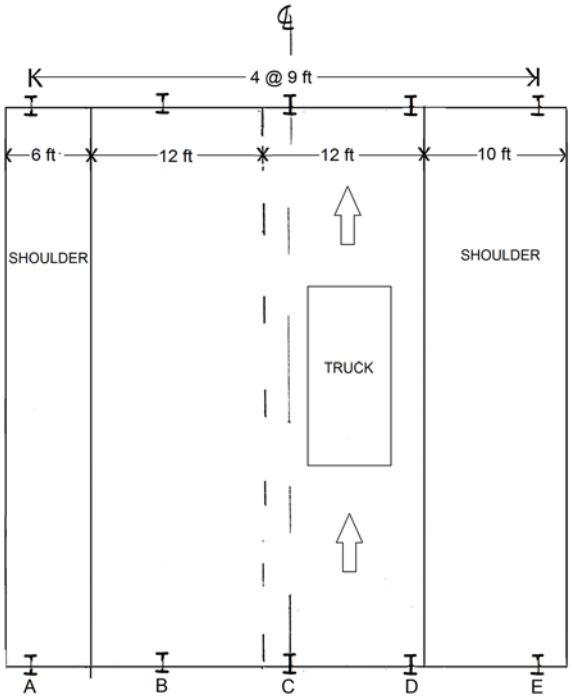

Figure 3-7: Schematic of bridge lanes and girders for bridges A-6243 and T-130

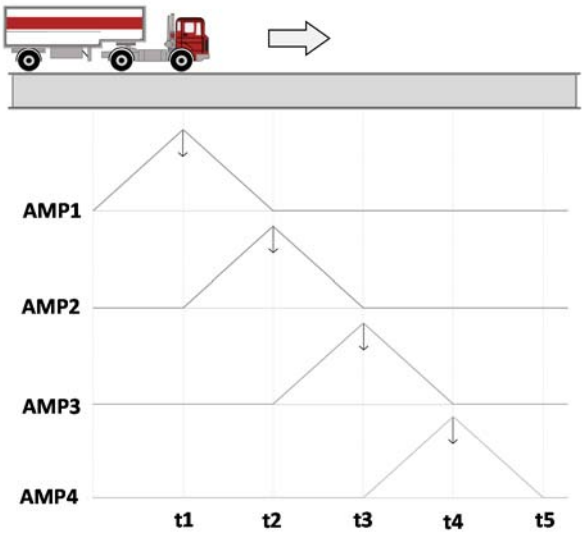

Figure 3-8: Wheel loading scheme

3.3. DETERMINATION OF FATIGUE DAMAGE

This section discusses the approach used to analyze the fatigue damage in critical bridge components.

3.3.1. Miner's Total Damage

Miner's rule is a commonly used cumulative damage model to evaluate fatigue performance in structural components. In Miner's total damage approach, fatigue damage is inversely proportional to the fatigue capacity at each applied stress range; furthermore, higher stress ranges result in greater fatigue damage. Miner's rule is shown in Equation 3-1

$$\sum \mathrm{D_i} = \sum \frac{\mathrm{n_i}}{\mathrm{N_i}} \qquad \text{Equation 3-1}$$

where D_i, n_i, and N_i are the damage, number of cycles and number of cycles to failure for each applied stress range, *i*. N_i is given by Equation 3-2

$$N_i = A(\Delta\sigma)^{-3} \qquad \text{Equation 3-2}$$

where A is the detail category constant (see Table 2-1) and $\Delta\sigma$ is the applied stress range. The individual cycles, n_i, and the applied stress range, $\Delta\sigma$, are determined using the rain-flow cycle counting procedure described in Appendix A.

In this work, Miner's rule is used to determine the location of bridge details susceptible to fatigue damage. The stress histories in bridge details are determined using ABAQUS and the resulting fatigue damage is compared for various locations along the span.

3.3.2. Modified Goodman Fatigue Analysis

The AASHTO steel bridge specification considers stress range (S-N curve) as the main parameter to evaluate fatigue. The modified Goodman criterion criteria provides a more accurate fatigue assessment by considering the localized effects of mean stress, stress amplitude, and the steel material properties. For a given stress cycle, the mean stress (σ_m) and the stress amplitude (σ_a) are expressed by Equation 3-3 and Equation 3-4

$$\sigma_m = \frac{\sigma_{max}+\sigma_{min}}{2} \quad \text{Equation 3-3}$$

$$\sigma_a = \frac{\sigma_{max}-\sigma_{min}}{2} \quad \text{Equation 3-4}$$

where σ_{max} and σ_{min} are the maximum and minimum stresses in a given stress history. A sample stress history denoting the variables the σ_m, σ_a, σ_{max}, and σ_{min}, is shown in Figure 3-9(a). Figure 3-9(b) show a constant life diagram (CLD) representing the modified Goodman criteria. The modified Goodman line is represented by a straight line acting through $\sigma_a = S_e$ and $\sigma_m = S_{ut}$. S_e and S_{ut} are the fatigue endurance limit and ultimate tensile strength of the material, respectively. The Goodman line is given by Equation 3-5

$$\frac{\sigma_a}{S_e} + \frac{\sigma_m}{S_{ut}} = \frac{1}{n} \quad \text{Equation 3-5}$$

where n is a factor of safety. A procedure for calculating S_e is presented in [42]. For steel, the endurance limit can be estimated as

$$S'_e = \begin{cases} .5\,S_{ut} & S_{ut} \le 200ksi \\ 100\ ksi & S_{ut} > 200ksi \end{cases} \quad \text{Equation 3-6}$$

The prime mark on S'_e refers to rotating-beam specimens prepared and tested in laboratory conditions. It is unreasonable to expect the actual endurance limit of a structural material, S_e, to match the values obtained in laboratory conditions; therefore, Marin [43] identified factors to quantify the effects of surface conditions, size, loading, temperature and miscellaneous items. The Marin equation is given by

$$S_e = k_a k_b k_c k_d k_e k_f S'_e \quad \text{Equation 3-7}$$

where k_a, k_b, k_c, k_d, k_e, and k_f, are respectively, the surface condition, size, load, temperature, reliability, and miscellaneous effects modification factors. The procedure to calculate S_e, and the Marin factors is shown in Appendix B.

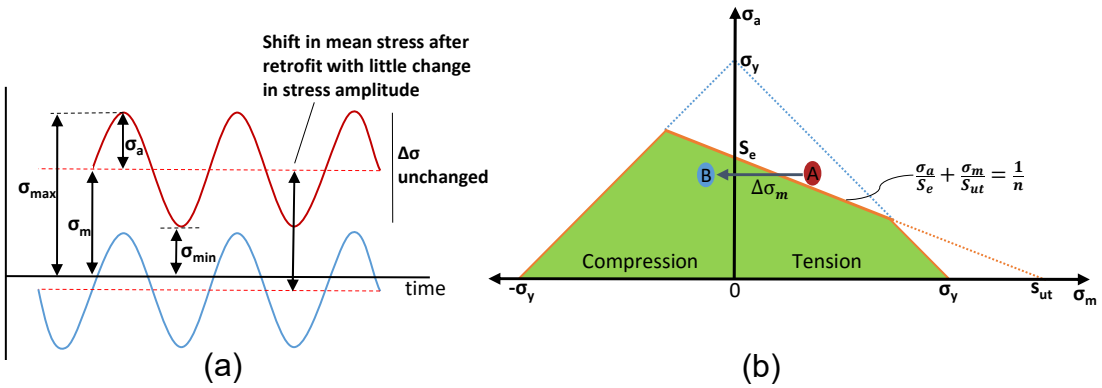

Figure 3-9: (a) Sample stress history (b) CLD representing the modified Goodman criteria

Using the modified Goodman criteria, a point σ_m and σ_a corresponding to a location above the curve is representative of finite fatigue life, where as a location below the curve is indicative of infinite fatigue life (safe region). A detail that contains finite fatigue life (point A in Figure 3-9(b)) can be shifted to a state of infinite fatigue life (point B in Figure 3-9(b)), by either reducing the stress amplitude or reducing the mean stress. Reducing the stress amplitude of critical fatigue details may require adjustments to the cross-section (hole-drilling, splice plates, etc.) or the loading conditions; however, reducing the mean stress can be achieved through post-tensioning techniques by shifting the stress range into a more compressive regime. Figure 3-9(a) shows the shift in mean stress with Figure 3-9(b) illustrating the corresponding shift on the Goodman diagram. The retrofit developed in this work utilizes pre-stressed CFRP strips to reduce the mean stress of bridge details into the safe region, extending the component life indefinitely.

4. RESULTS AND DISCUSSION FROM MODEL ANALYSES

4.1. VALIDATION OF MODELING TECHNIQUES

In addition to the evaluation of the four bridges described earlier, a validation study is included in this work to verify that the modeling techniques used are satisfactory. The validation study was conducted on bridge A-6243, and uniaxial strain gauges were

installed on the actual bridge superstructure to record strain measurements for comparison with results from the FEM analysis. Figure 4-1 shows a picture of the (a) actual cross-frame compared with the (b) modeled cross-frame. The dimensions of the model closely match the actual dimensions of all the structural components, as they were taken from the actual design drawings.

The bridge was instrumented with three uniaxial strain gauges. Figure 4-2 shows the location and a picture of each of the installed strain gauges. Gauge 1 is located on the central girder below the cross frame detail approximately 23 ft from the end support of the

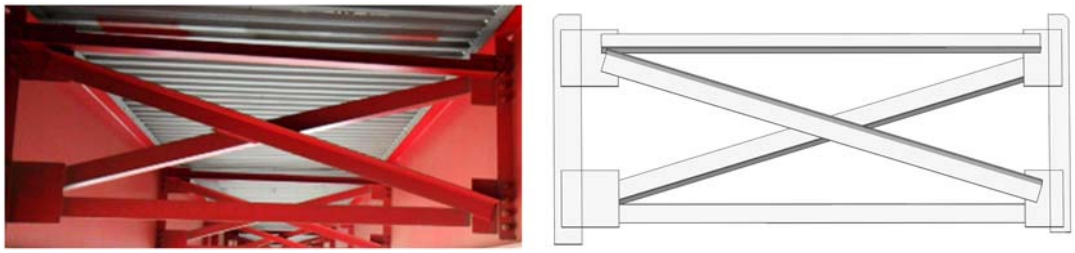

Figure 4-1: (a) Actual cross-frame detail and (b) modeled cross-frame with rendered shell thickness

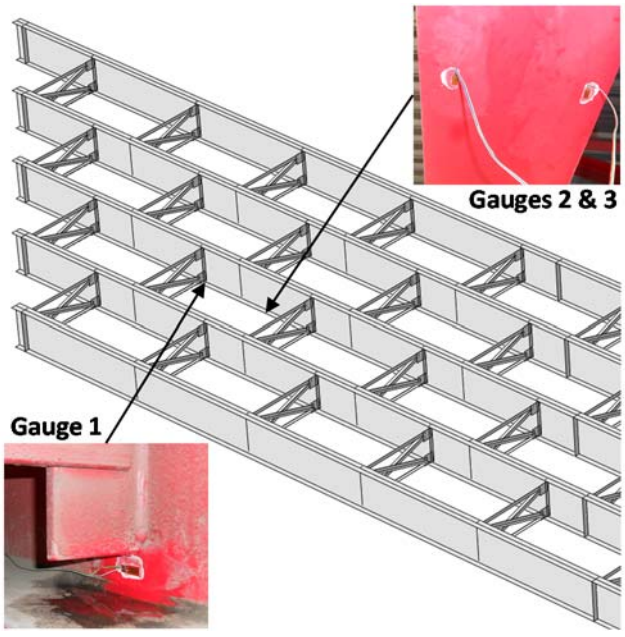

Figure 4-2: Location and picture of installed strain gauges

structure. Gauges 2 and 3 are located on the bottom of the tension flange of the central girder approximately 32 ft – 7 in. from the end support. In order to obtain accurate and precise strain measurements, the installation surface is typically cleaned and prepared prior to bonding of the strain gauge, where the surface is stripped of any paints or coatings, then cleaned to remove stagnant dust particles. During this validation study however, the gauges were applied above the coated steel in an effort to preserve the corrosion protection on the bridge girders.

The University of Arkansas vibroseis truck served as the controlled traffic condition on the bridge. During the field test and FEM analysis, the truck was driven across the bridge in the right lane of the two lane bridge. A schematic of the lanes and location of the girders was shown previously in Figure 3-7. Figure 4-3 shows a picture of the vibroseis truck, axle spacing, and the individual wheel loads used in both the bridge loading and ABAQUS simulation. The two axles are spaced at 16 ft – 6 in. A wheel load of 3,800 lb acts on both the driver and passenger front tires, while wheel loads of 7480 lb and 7290 lb act on the rear driver and rear passenger tires, respectively.

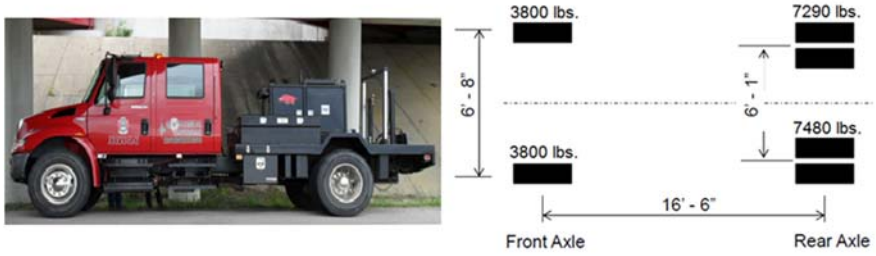

Figure 4-3: Vibroseis truck axle weights and individual wheel loads

In the validation study, the bridge is analyzed dynamically as opposed to statically in order to better simulate the truck passage when compared with the experimental readings. Table 4-1 shows the number of elements and nodes considered in the dynamic analysis, as well as the number of equations and approximate computational time necessary to complete the analysis. By specifying a larger element size of 3 in., the computation cost was reduced to about half the expense necessary for the static analysis. The dynamic analysis is conducted using the Hilber-Hughes-Taylor time integrator. The Hilber-Hughes-Taylor is an implicit integration approach where the

Table 4-1: Number of elements, nodes, equations, and computation time for dynamic analysis

Bridge	Span Length	Typical Element Size	No. of Elements	No. of Nodes	No. of Equations/ Unknowns	Comp. Time
A-6243	240 ft	3 in.	165,142	175,530	1,050,888	17.67 hrs.

operator matrix must be inverted, and a set of simultaneous nonlinear dynamic equations must be solved at each time increment; this solution is done iteratively using Newton's method [40].

Sequences of dynamically applied loads simulate the truck passage along the bridge span. This is similar to the static analysis, where vertical loads corresponding to the individual wheel loads are activated and deactivated in series to simulate a moving load (see Figure 3-8); however, the dynamic analysis considers inertial effects and vibrations of the bridge from previous time-steps. Two percent Rayleigh damping from the first and second vibration modes was considered in the analysis.

A truck speed of 63 mph was recorded during the strain measurements and used in the dynamic analysis. Figure 4-4(a-c) shows the strain measurements recorded during the truck passage compared with the results of the FEM simulation for gauges 1, 2, and 3, respectively. The recorded real-time strain data for each of the gauges is shown by the solid line, while the FEM results for the corresponding location is shown by the dotted line.

From Figure 4-4, the FEM results overestimate the strain values by about 20-40 μin./in. for each of the strain gauge locations. This error may be the result of two primary modeling issues:

(1) The concrete bridge deck was excluded from the FEM. The concrete deck may significantly increase the stiffness of the bridge section, consequently reducing the strain calculated in the bridge girders. It is important to note that the deformations are measured on a very small scale; therefore, a small change in the cross-section of structural elements may significantly affect the FEM analysis. Inclusion of the concrete deck also may have doubled the computational cost of the analysis.

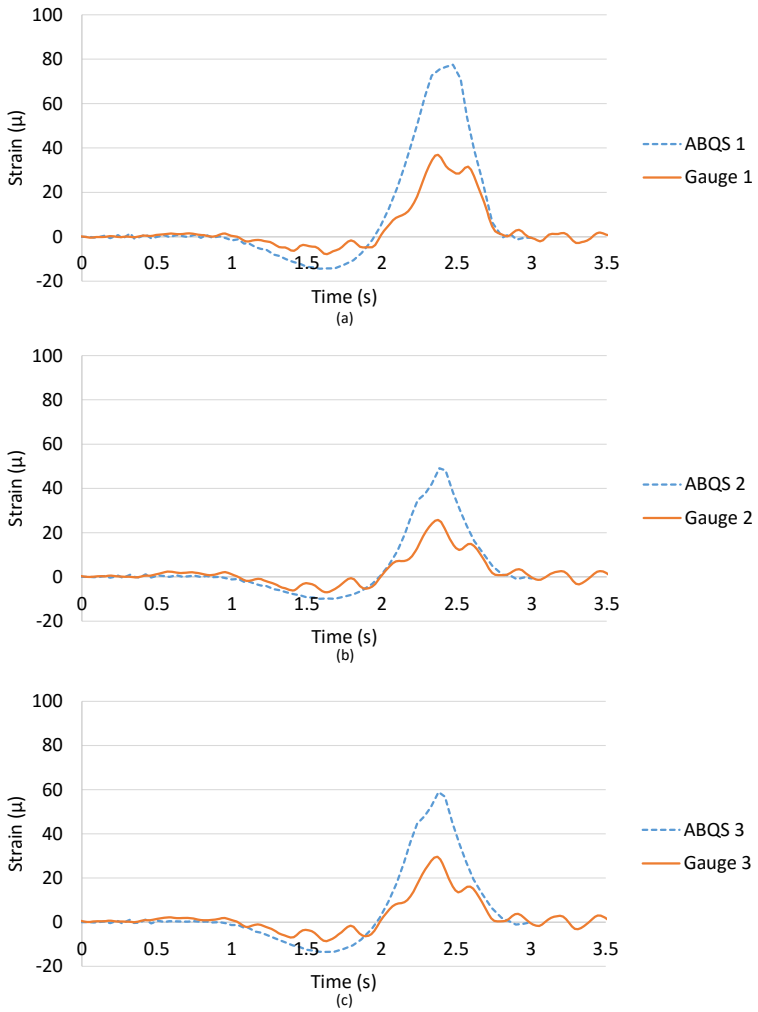

Figure 4-4: Comparison of strain gauge measurements with FEM results at (a) gauge 1, (b) gauge 2, and (c) gauge 3 locations

(2) The model assumes that the truck weight was distributed equally amongst the girders under the traffic lane. This assumption was made based on the tributary area of the girders supporting the traffic lane. In the actual structure the truck may not have been centered in the traffic lane, which may cause the load to be distributed unevenly to the girders. Additionally, the inclusion of a concrete deck may have helped to distribute the truck load to other girders.

Some other causes of error may include the following: Strain gauges were installed above the coated steel as opposed to being installed to the bare steel. A mesh and element size of 3 in. was used in the FEM analysis. This mesh can be further refined

to produce more accurate results in local areas having higher strain gradients. Comparing the predicted and measured responses, it is determined that the ABAQUS model reasonably computed the local strains observed during testing.

4.2. DETERMINATION OF CRITICAL FATIGUE REGIONS

In steel structures, critical fatigue regions typically occur near the welded connection of components. The presence of the weld creates concentrated stresses at the weld toe during loading cycles and can eventually initiate fatigue cracks. Figure 4-5 shows the von Mises stress distribution in bridge A-6243 when the truck is at mid-span. In this bridge, concentrated stresses can be seen in two locations: 1) welded connection between the transverse stiffener and top flange of the girder, and 2) welded connection between the bottom of the transverse stiffener and the girder web. For the four bridges analyzed in this work, locations with high stress concentrations are investigated further to determine the applied stress range and accumulated fatigue damage.

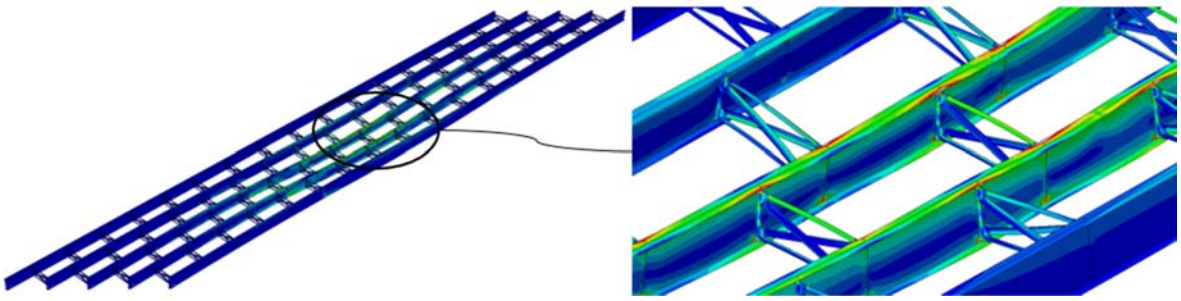

Figure 4-5: von Mises stress distribution at mid-span in bridge A-6243
(Note: Deflections are scaled 30 times)

To determine the location of critical fatigue components, stress cycles in structural details were compared at various locations along the bridge span. The bridge models were analyzed assuming a fatigue 1 load combination for five different load factors ranging from 1.5 (actual AASHTO fatigue 1 load factor) to 2.0 (hypothetical load factor). Various load factors are considered to determine the effect of an increased load on the local stress range and overall fatigue performance of the bridge detail.

Figure 4-6 shows the resulting stress cycles from the maximum in plane stress component due to the five considered load factors (1.5, 1.65, 1.75, 1.85, and 2.0) and

location of the details most susceptible to fatigue in each bridge. At least two structural details were identified for each bridge based on the stress range and detail category. As expected, the cross frame or diaphragm detail subjected to the highest stress range is located midway between supports for each bridge (see location 2, 5, 7, 8, and 9). These locations all contain welded connections between the bottom of the cross-frame configuration and the web of the longitudinal girder. Location 4 (see Figure 4-6(b)) is positioned on the opposite side of the weld between the diaphragm and the girder web. Due to the skewed bridge geometry, this location is subjected to distortion induced fatigue, where the girder web displaces laterally as well as vertically. This distortion can also be found in bridge A-6243 location 9 (see Figure 4-6(d)). Figure 4-7shows the distortion in the girder web of bridges (a) A-6243 and (b) A-3958 due to the skewed bridge geometry. Figure 4-7(b) illustrates how the distortion in the web creates tensile stresses on the opposite side of the diaphragm connection due to the lateral deflections in the web. Additionally, tensile stresses are present at the bottom of the diaphragm connection within the weld due to the downward deflection. In Figure 4-7(a), the transverse stiffener is welded to the top flange and the web of the girder which helps to lessen the lateral deflection near the top of the section; however, high stress concentrations are still present within the web at the bottom of the cross-frame detail due to lateral and downward deflections.

Locations 1, 3, and 6 show the stress history at the weld between the cover plate and the flange of the longitudinal girder. The stress history at location 6 (see Figure 4-6(c)) is within the top flange as opposed to the bottom flange because the detail is located over a negative moment region in the continuous span of bridge T-130. Finally, location 10 (see Figure 4-6(d)) show the stress history at the weld between the bearing stiffener and the flange of the girder. Similar to location 6, location 10 is also within a negative moment region, above the fixed support of bridge A-6243.

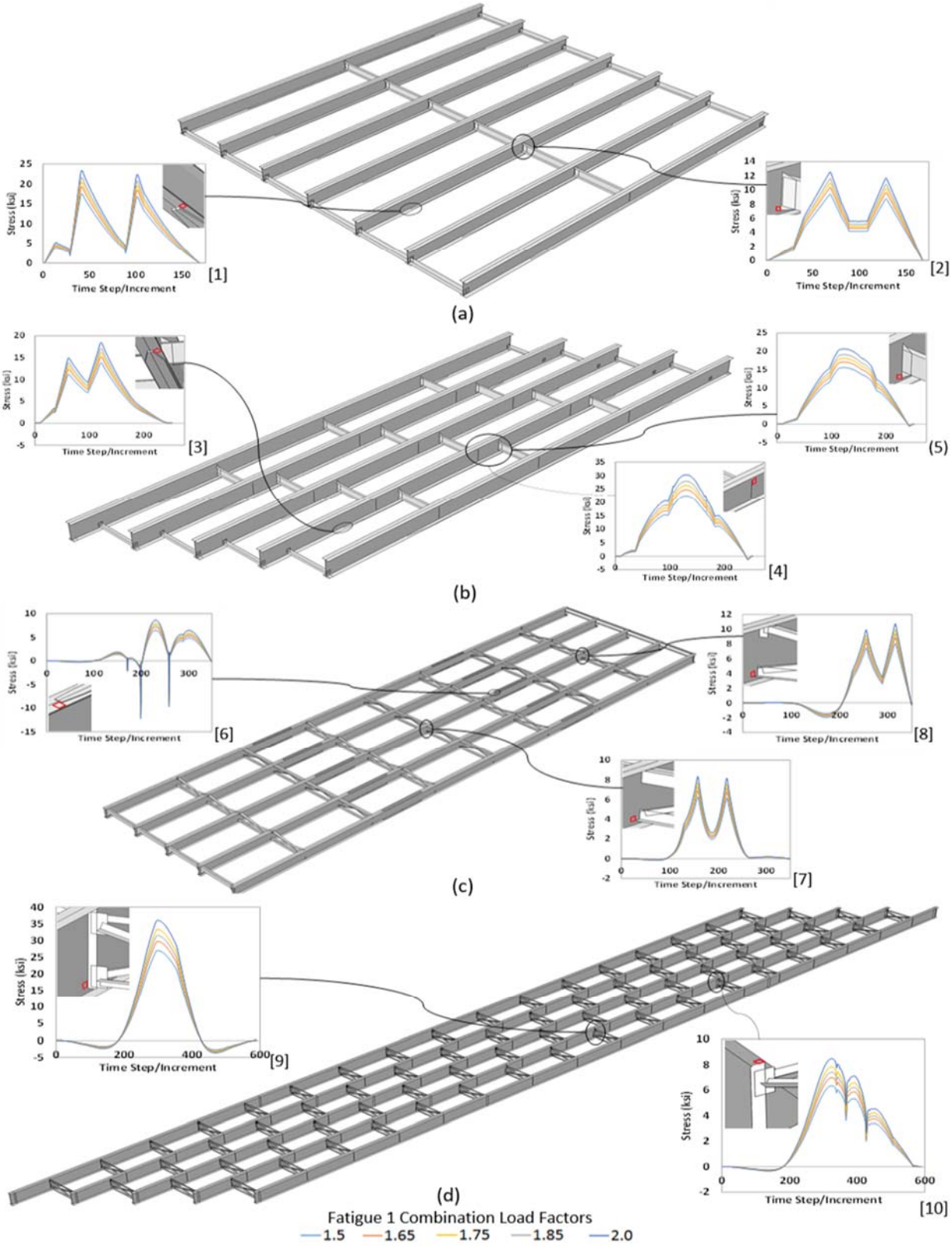

Figure 4-6: Stress history at structural details most susceptible to fatigue for bridges (a) A-3956, (b) A-3958, (c) T-130, and (d) A-6243

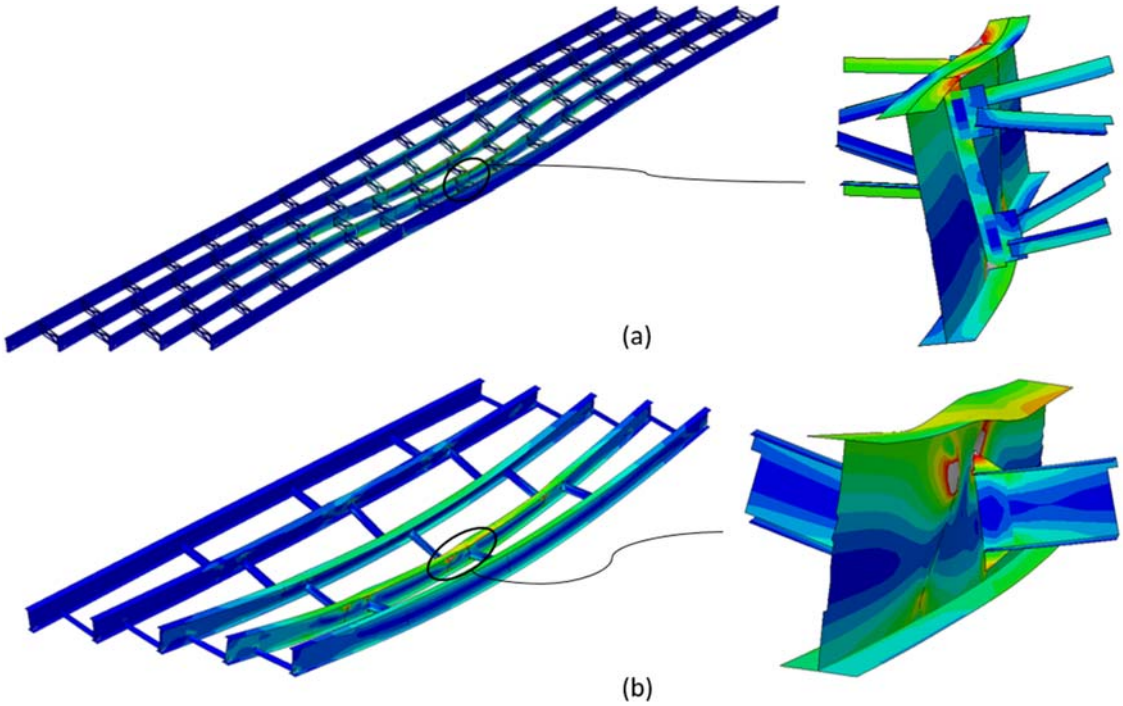

Figure 4-7: von Mises stress distribution showing distortion in the girder web of bridges (a) A-6243 and (b) A-3958 (Note: Deflections are scaled 50 times for visualization.)

The fatigue damage resulting from the different stress histories is determined through cycle counting using the rain-flow counting method (see Appendix A), and linear fatigue damage accumulation using Miner's rule (described in Section 3.3.1). Table 4-2 shows the resulting fatigue damage in the bridge details due to the stress histories shown in Figure 4-6 considering the 1.5 load factor. This calculation assumes that only 60% of the stress within the compressive region is damaging [44].

In Table 4-2, the largest fatigue damage within bridges A-3956, A-3958, and T-130 is found within the weld between the cover plate and girder flange (see locations 1, 3, and 6). This high fatigue damage is due to the low fatigue capacity associated with the cover plate connection (AASHTO detail category E) compared with the other detail categories. The remaining structural details (locations 2, 4, 5, 7, 8, 9, and 10) are all located at cross-frame or diaphragm connections and contain stress ranges similar to or much greater than the cover plate details. These structural details contain much higher fatigue capacities according to the 2012 AASHTO specification and are consistent with detail categories C' (location 2, 5, 9, and 10) or D (location 7 and 8), with the exception of

Table 4-2: Fatigue damage calculations for critical structural details due to 1.5 load factor

Location[a]	Bridge	Stress Range (ksi)	Number of Cycles (n_i)	N_i[b]	Total Damage (ΣD)
1	A-3956	17.2	1	7.66E+04	2.07E-05
		2.1	1	4.21E+07	
		14.4	1	1.31E+05	
2	A-3956	9.2	1	5.65E+06	1.99E-07
		4.6	1	4.52E+07	
3	A-3958	13.7	1	1.52E+05	6.77E-06
		4.1	1	5.66E+06	
4	A-3958	22.4	1	2.22E+06	4.50E-07
5	A-3958	15.5	1	1.18E+06	8.46E-07
6	T-130	1.42	1	3.84E+08	1.90E-06
		1.4	0.5	4.01E+08	
		6.92	0.5	3.32E+06	
		11.92	0.5	6.49E+05	
		10.78	0.5	8.78E+05	
		9.18	0.5	1.42E+06	
		4.8	0.5	9.95E+06	
7	T-130	6.2	1	9.23E+06	1.42E-07
		4.2	1	2.97E+07	
8	T-130	8.8	1	3.23E+06	3.57E-07
		4.7	1	2.12E+07	
9	A-6243	1.62	1	1.03E+09	4.95E-06
		27.92	1	2.02E+05	
10	A-6243	6.48	1	1.62E+07	6.35E-08
		1.7	1	8.96E+08	
		1.3	1	2.00E+09	

Note: [a]See Figure 4-6 for location, [b]See Equation 3-2 in Section 3.3.1

location 4 which is identified as detail category A. Although the cross frame details are indicated as the fastest damage accumulation based on nominal stress data and the AASHTO detail categories, at a fundamental level fatigue performance is based on the mean stress and stress amplitude; therefore each location in Figure 4-6 is analyzed using the Goodman criterion to determine which details are not within the infinite fatigue life (safe) region.

4.3. GOODMAN DIAGRAM AND FATIGUE LIFE EVALUATION

Each bridge detail identified in Figure 4-6 was evaluated using the modified Goodman criterion. The development of the Goodman diagrams presented herein followed the calculations described earlier in Section 3.3.2. Construction documents indicate that the bridges considered are constructed of grade 50 steel with a yield stress of 50 ksi and ultimate strength of 65 ksi. The endurance limit, S_e, was calculated as 14 ksi using the Marin equation (see Appendix B). The resulting Goodman plots are shown in

Figure 4-8, only showing the most critical fatigue detail in both the (a) skewed bridges and (b) non-skewed bridges.

Note that the Goodman diagrams consider the maximum in-plane principal stresses, as opposed to the maximum in plane stress component that was used in the damage calculation from the AASHTO detail categories; therefore, the stress ranges are greater than the values shown in Figure 4-6 and Table 4-2. Principal stresses are considered because crack growth is expected propagate in a direction perpendicular to the maximum in-plane stress. The five data points shown for each bridge represent the different load factors (1.5, 1.65, 1.75, 1.85, and 2.0) considered in the analysis.

In the skewed bridges, the critical fatigue details were identified as location 4 in bridge A-3958 and location 9 in bridge A-6243. In the non-skewed bridges, the critical fatigue details were identified as location 8 in bridge T-130 and location 1 in bridge A-3956. Figure 4-8 plots the stresses in each critical fatigue detail on the Goodman diagram for (a) the skewed bridges, and (b) the non-skewed bridges, for each of load factor. All of the data points within the skewed geometry fall within the finite fatigue life (unsafe) region of the Goodman plot; conversely, all of the data points within the non-skewed geometry are within the infinite fatigue life (safe) region, with the exception of the 2.0 load factor at location 1 in bridge A-3956. All of the other bridge details evaluated (locations 2, 3, 5, 6, 7, and 10) were within the infinite fatigue life region.

The data in Figure 4-8 clearly show that skewed bridge construction is much more damaging to the steel component fatigue life than non-skewed construction. Partial depth web attachments found in the cross-frame or diaphragm to web connections within the skewed bridges were susceptible to higher stress ranges than in non-skewed bridges due to distortions in the girder web during the passage of the fatigue truck. Results from this analysis also show that an increase in the applied load (load factor) corresponds to a proportional increase in both the mean stress and stress amplitude. To shift the steel component life from finite fatigue life to infinite fatigue life, a localized retrofit utilizing pre-stressed CFRP is developed to reduce the mean stress to the safe region.

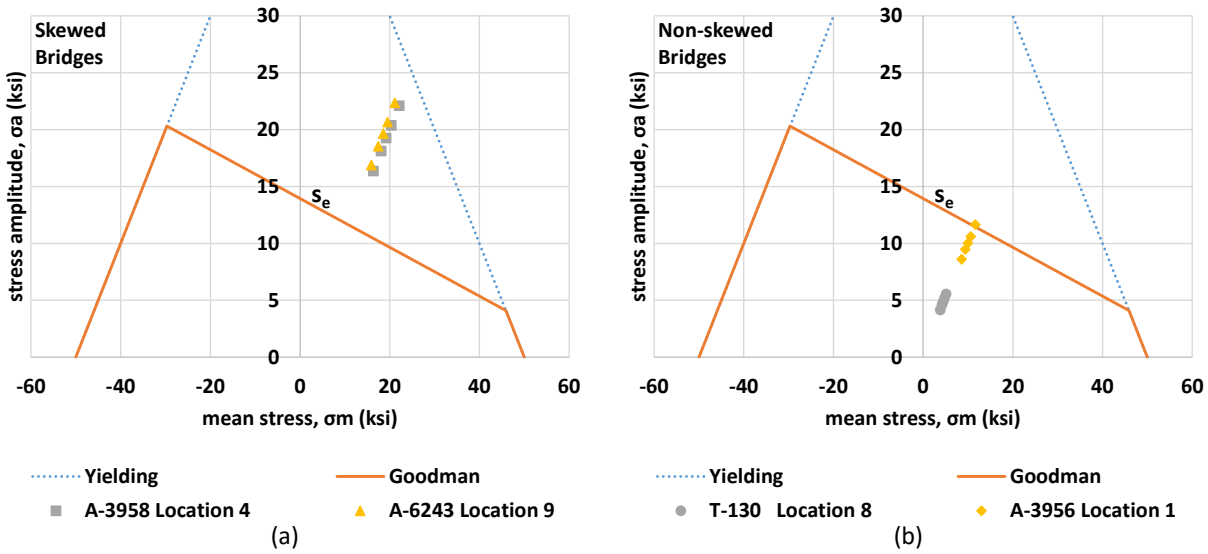

Figure 4-8: Goodman plots for the critical fatigue detail in the (a) skewed bridges (A-3958 & A-6243) and (b) non-skewed bridges (A-3956 & T-130)

5. RETROFITS FOR INFINITE COMPONENT FATIGUE LIFE

5.1. DEVELOPMENT OF RETROFIT

The retrofit developed in this work consists of stainless steel clamps and fixtures which can be locally installed near a structural detail. In this configuration, T-clamps used to grip the CFRP material are inserted into a holder which is bonded to the structural component. The pre-stress is applied to the CFRP by separating the T-clamps from the holders using threaded bolts. Figure 5-1 shows the retrofit and illustrates the installation procedure. As shown in Figure 5-1, the CFRP is un-bonded from the structural member, while the holder is bonded to the structural member using structural adhesive. In this system, the CFRP material or parts of the metal fixtures can be easily replaced if necessary by simply loosening the bolts on the holders and T-clamps.

The retrofit can be installed locally at the critical fatigue region within common bridge connection details. Consider a partial depth web attachment similar to location 9 in Figure 4-6. Figure 5-2 shows how the pre-stressed CFRP retrofit may be installed to reduce the mean stress in this bridge detail. Crack growth is expected to occur at the weld toe between the transverse stiffener and the girder web. The retrofit should be installed perpendicular to the direction of crack growth so that the pre-stress force is acting to close

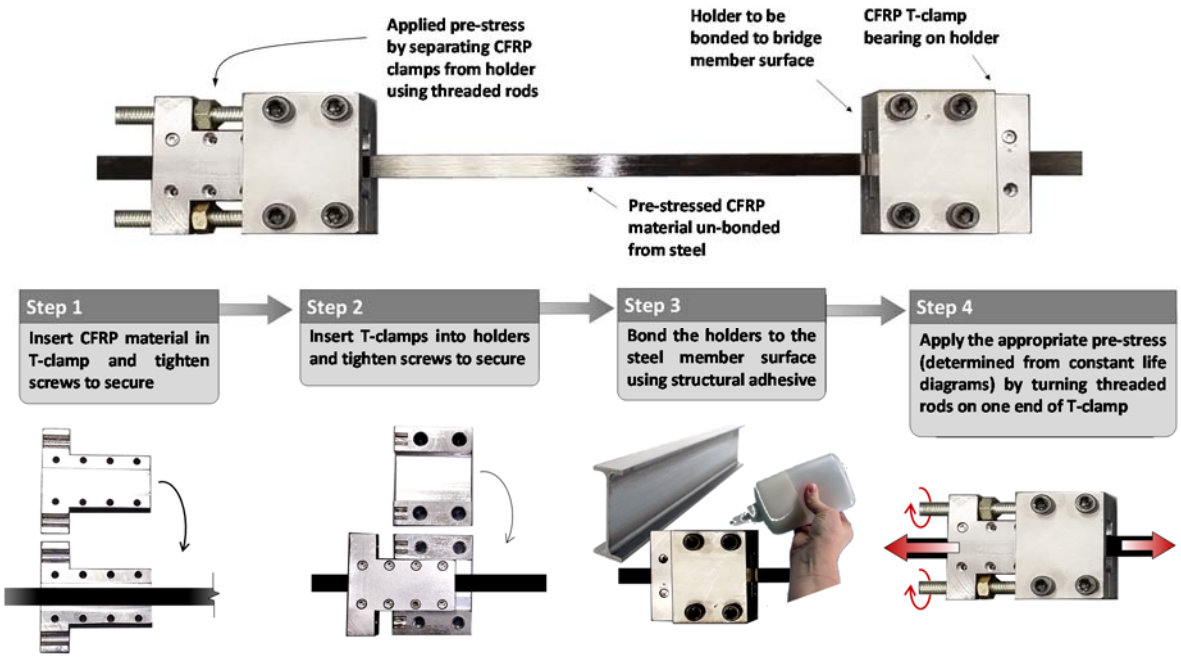

Figure 5-1: CFRP retrofit and installation procedure

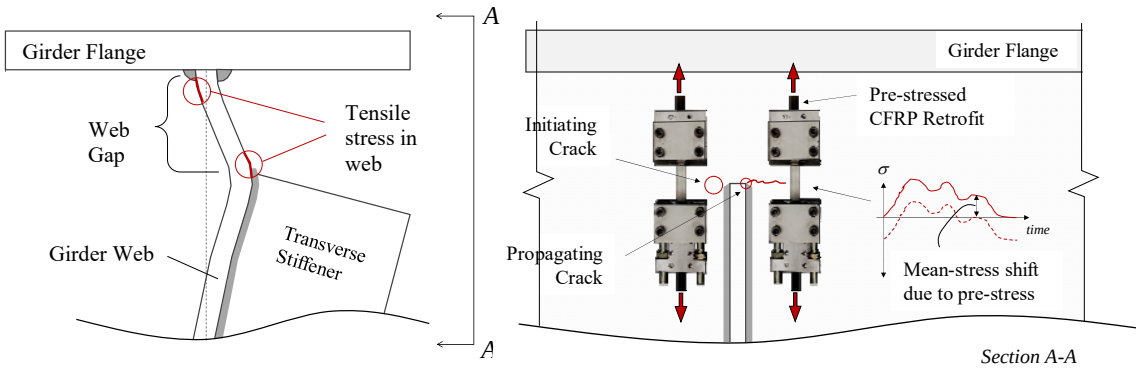

Figure 5-2: Example of retrofit installation on a partial depth web attachment showing shift in mean stress due to the pre-stressed CFRP.

the crack. The applied pre-stress will prevent crack initiation or crack propagation by shifting the mean stress in the structural detail to a safe limit on the Goodman diagram.

5.2. DEVELOPMENT OF EQUATIONS TO SHIFT COMPONENT LIFE FROM FINITE TO INFINITE LIFE

The determination of the minimum pre-stress required to shift the component from a state of finite life to infinite fatigue life is based on the retrofit shown in Figure 5-1 and the Goodman constant life diagram. Let σ_{mi} and σ_{ai} represent the stresses in the structural

detail before strengthening, corresponding to point A in the Goodman diagram shown in Figure 5-3. Point B, corresponding to the point (σ_{mf}, σ_{af}) represents the stress in the structural detail after installation of the retrofit. The shift in mean stress is indicated by $\Delta\sigma_m$ and is written as

$$\Delta\sigma_m = \sigma_{mi} - \sigma_{mf} \qquad \text{Equation 5-1}$$

where σ_{mf} is obtained by rewriting the Goodman equation in terms of mean stress shown in Equation 5-2. Due to the thin cross section and an elastic modulus similar to steel, the CFRP is assumed to add negligible stiffness to the component cross section; therefore, a negligible decrease in the stress amplitude is expected. As a result, σ_{ai} is equal to σ_{af} in the following equations.

$$\sigma_{mf} = \frac{S_{ut}}{n} - \frac{S_{ut}\sigma_{af}}{S_e} \qquad \text{Equation 5-2}$$

Substituting Equation 5-2 into Equation 5-1 gives

$$\Delta\sigma_m = \sigma_{mi} + \frac{S_{ut}\sigma_{af}}{S_e} - \frac{S_{ut}}{n} \qquad \text{Equation 5-3}$$

where $\Delta\sigma_m$ is the minimum compressive stress required to shift the mean stress from point A to point B, and n is a factor of safety.

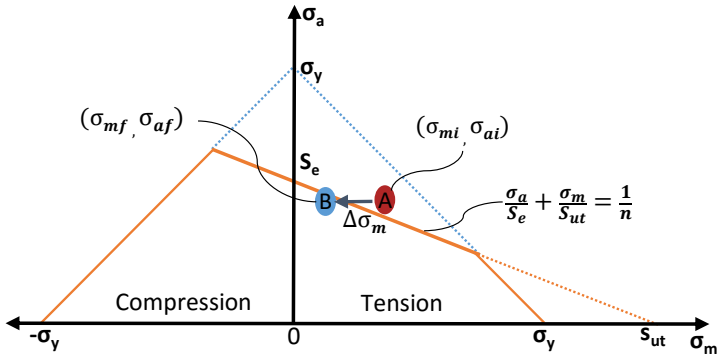

Figure 5-3: Shift in mean stress for infinite component life

The minimum pre-stress force (F_{pre}) corresponding to $\Delta\sigma_m$ can be determined through a cross section analysis of the structural component and retrofit configuration. Figure 5-4 shows the front and side view of the retrofit attached to a bridge girder web identifying the parameters needed to calculate F_{pre}. Considering the small area encompassed by the retrofit, $\Delta\sigma_m$ can be estimated as

$$\Delta\sigma_m = \frac{e\,F_{pre}\,t_w}{2\,I_m} + \frac{F_{pre}}{A_m} \qquad \text{Equation 5-4}$$

where t_w is the thickness of the girder web; A_m and I_m are the cross-sectional area and moment of inertia of a small region of the cross section encompassed by the retrofit; and e is the eccentricity between the CFRP material and the centroid of the girder web. Rearranging Equation 5-4 in terms of F_{pre} gives

$$F_{pre} = \frac{\Delta\sigma_m}{\frac{e\,t_w}{2\,I_m} + \frac{1}{A_m}} \qquad \text{Equation 5-5}$$

Finally, the minimum pre-stress required for infinite component fatigue life is written as

$$\sigma_{pre} = \frac{F_{pre}}{A_p} \qquad \text{Equation 5-6}$$

where A_p is the cross sectional area of the CFRP material.

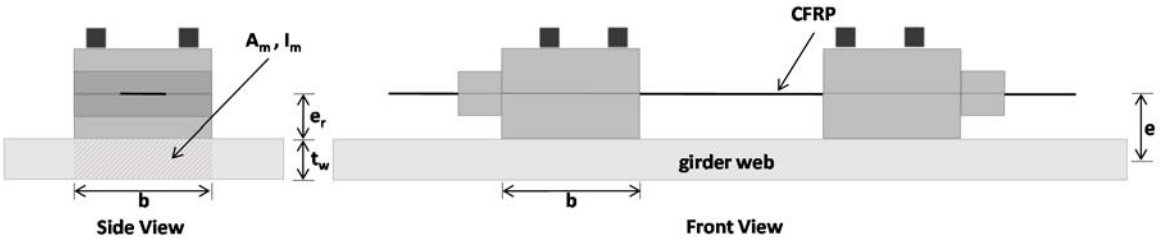

Figure 5-4: Front and side view showing dimensions of retrofit attached to a bridge component

5.3. MINIMUM CFRP PRE-STRESS REQUIRED FOR INFINITE COMPONENT FATIGUE LIFE

Tables 5-1 and 5-2 show the results of the calculations for $\Delta\sigma_m$ and F_{pre} following the procedure described above. Results are only shown for Location 4 in bridge A-3958 and Location 9 in bridge A-6243 (see Section 4.2, Figure 4-6) as these two details were the only components that contained stresses in the finite life region of the Goodman plot; all of the other bridge details evaluated (locations 2, 3, 5, 6, 7, and 10) were within the infinite fatigue life region. As discussed previously in this report, the bridges are constructed of grade 50 steel with a yield stress (S_y) of 50 ksi and ultimate strength (S_{ut}) of 65 ksi. The endurance limit (S_e) was predetermined as 14 ksi using the Marin equation (see Appendix B). The parameters necessary for the calculation of F_{pre} are shown in Figure 5-4 in which b = 2.0 in. and e_r = 0.5 in. Based on the construction documents, t_w = 0.65 in. for bridge

Table 5-1: Calculation of pre-stress force (F_{pre}) required for infinite component fatigue life in critical details for bridge A-3958 location 4.

AASHTO Fatigue I Load Factor	σ_{mi}	σ_{mf}	σ_{ai}, σ_{af}	$\Delta\sigma_m$	F_{pre}
1.5	16.35	-11.20	16.35	27.56	4.19
1.65	18.1	-19.36	18.1	37.46	5.69
1.75	19.25	-24.72	19.25	43.98	6.68
1.85	20.35	-29.85	20.35	50.20	Reduction in σ_a necessary
2	22.1	-38.01	22.1	60.11	Reduction in σ_a necessary

Table 5-2: Calculation of pre-stress force (F_{pre}) required for infinite component fatigue life in critical details for bridge A-6243 location 9.

AASHTO Fatigue I Load Factor	σ_{mi}	σ_{mf}	σ_{ai}, σ_{af}	$\Delta\sigma_m$	F_{pre}
1.5	15.92	-13.67	16.88	29.60	2.96
1.65	17.46	-21.41	18.54	38.88	3.89
1.75	18.56	-26.54	19.64	45.10	4.51
1.85	19.53	-31.34	20.67	50.87	Reduction in σ_a necessary
2	21.15	-39.17	22.35	60.32	Reduction in σ_a necessary

A-3958, and t_w = 0.5 in. for bridge A-6243. The calculation was completed for the actual AASHTO fatigue I load factor (1.5) and four theoretical load factors (1.65, 1.75, 1.85, and 2.0). The data in Table 5-1 is plotted in Figure 5-5.

Figure 5-5(a) uses the Goodman plot to illustrate the minimum shift in mean stress ($\Delta\sigma_m$) and corresponding pre-stress force (F_{pre}) required for infinite component life, considering the AASHTO 1.5 fatigue I factor. According to Figure 5-5(a) and the data in Table 5-1, bridges A-3958 and A-6243 contain a similar mean stress and stress amplitude before strengthening, resulting in a similar shift in $\Delta\sigma_m$; however, F_{pre} varies due to differences between the two girder cross-sections. Bridge A-6243 has a smaller girder thickness (t_w), cross-sectional area (A_m) and moment of inertia (I_m), which reduces the F_{pre} required to reduce the mean stress.

Figure 5-5(b) plots the F_{pre} required for infinite life in the critical bridge details, considering AASHTO fatigue I load factors ranging from 1.5 to 2.0. According to Figure 5-5(b), the F_{pre} required for infinite life increases linearly as the load factor increases. F_{pre} increases more rapidly in bridge A-3958 than bridge A-6243. While the critical fatigue detail in these two bridges contain similar mean stresses and stress amplitudes, this plot shows that the a smaller web thickness in bridge A-6243 results in a slower rate of

increase of F_{pre} as the load increases. As shown in Figure 5-5(a), σ_a reaches its maximum at 20.3 ksi when σ_m is -29.7 ksi. The maximum value of σ_a is slightly exceeded for both bridge A-3958 and A-6243 when the factored load is 1.85 (refer to Table 5-1); therefore, a reduction in σ_a becomes necessary to achieve infinite fatigue life when the stress range corresponding to the 1.85 load factor is exceeded for these bridge details. As stated previously in this report, σ_a can be reduced by increasing the stiffness of the structural detail; however, if the increase in stiffness is achieved by enlarging the cross-section, F_{pre} will also increase.

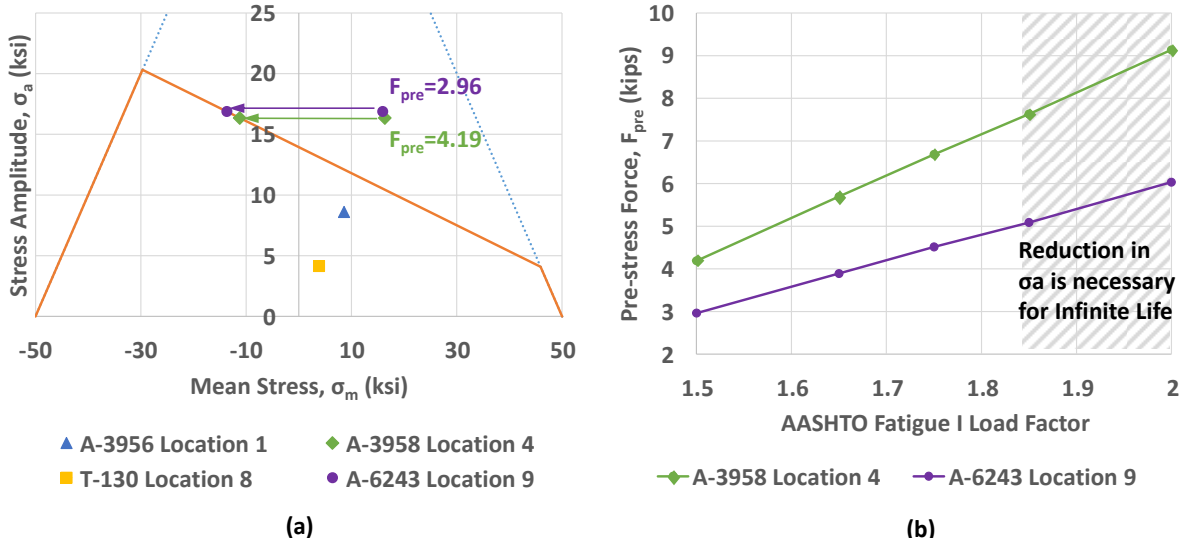

Figure 5-5: Minimum F_{pre} required for infinite fatigue component life in critical bridge details (a) illustrated in Goodman plot considering AASHTO 1.5 fatigue I load factor (b) considering AASHTO fatigue I load factors between 1.5 and 2.0

5.4. EXPERIMENTAL TESTING OF RETROFIT SOLUTION

A simple laboratory test was developed to evaluate the performance of the proposed pre-stressed CFRP retrofit system. In this experiment, a small-scale girder with a welded diaphragm connection is developed based on the cross frame configuration in bridge A-3958 (see 3.2.1, Figure 3-3). The beam is instrumented with strain gauges in order to compare readings before and after installation of the retrofit. Pictures of the experimental setup are shown in Figure 5-6. The diaphragm detail shown in Figure 5-6(c) is constructed of two L-shapes (1.5 in. × 1.5 in. × 0.125 in.) welded together to form a

C-shape. The C-shape is welded to the face of a 1/8 in. steel plate, then welded to the web of a W8× section.

The beam is simply supported (see Figure 5-6(d)) and instrumented with two uniaxial strain gauges below the diaphragm detail on both sides of the beam. A third strain gauge is installed on the surface of the CFRP in order to measure the strain due to the applied pre-stress. Figure 5-6(b) shows the location of two of the three installed strain gauges. Strain gauges were installed on smooth steel, achieved by cleaning and grinding the beam surface. A linear variable differential transformer (LVDT) (shown in Figure 5-6(a)) was used to measure local deflections of the beam during loading.

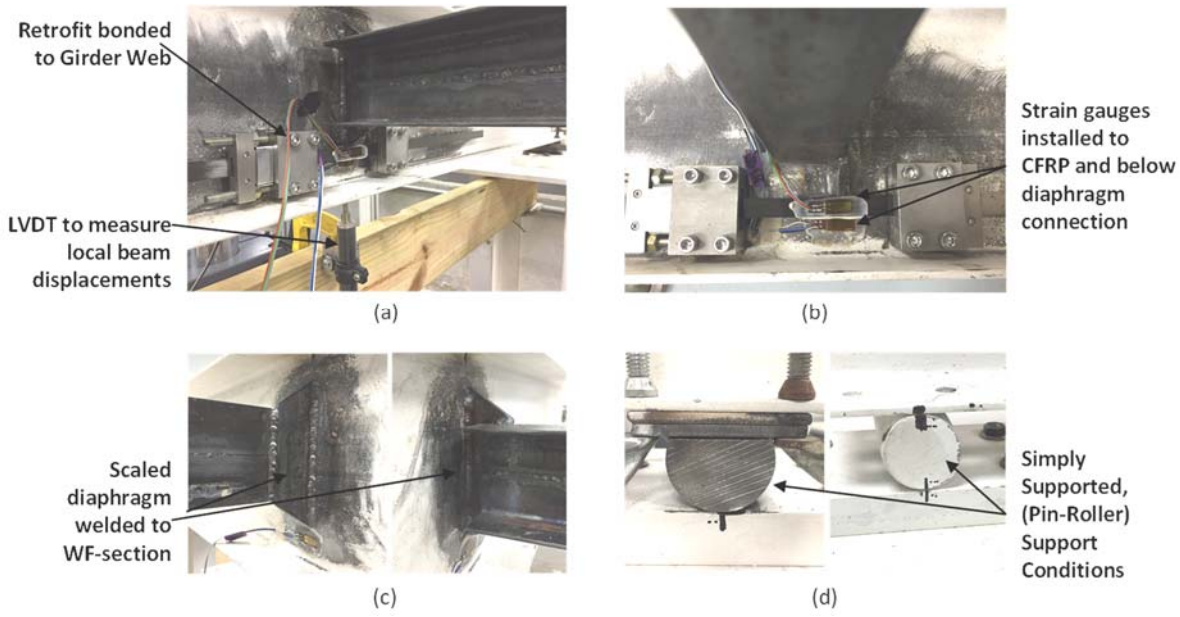

Figure 5-6: Pictures of experimental test setup showing (a) retrofit bonded to structure, (b) installed strain gauges, (c) diaphragm to web connection detail, (d) test support conditions

The retrofit was bonded to the beam using structural adhesive as shown in Figure 5-6(a) and (b). The retrofit was installed over the strain gauge located below the diaphragm connection in order to compare the strain readings beneath the diaphragm before and after pre-stressing the CFRP. Pre-stress was applied to the CFRP by hand through turning the threaded bolts on the retrofit as described in Section 5.1. The beam

was cyclically loaded in a three-point configuration, with the load applied at mid span above the diaphragm connection at a rate of 0.5 Hz.

Results of the experimental test show a shift in the stress range after the installation of the retrofit as shown in Figure 5-7. The stress was calculated using Hooke's law ($\sigma = \varepsilon E$), assuming a typical steel young's modulus of 29,000 ksi. The mean stress under the applied load was 1.77 ksi before strengthening and 1.15 ksi after strengthening, resulting in a mean stress shift of 0.62 ksi.

Although this experiment only provides a preliminary evaluation of the retrofit performance, the results indicate that the retrofit is capable of shifting the mean stress of structural details therein improving fatigue performance. One challenge faced during this experiment was preventing slip between the CFRP and the T-clamps. Attempts were made to increase the friction between the clamps and CFRP using heavy grit sand paper, but were unsuccessful as the pre-stress force increased. Bonding the CFRP to the T-clamps using structural adhesive may provide a more permanent solution suitable for a laboratory test at this scale. Ultimately, a thorough evaluation of slip will need to be conducted and a new clamping configuration will need to be developed in further testing.

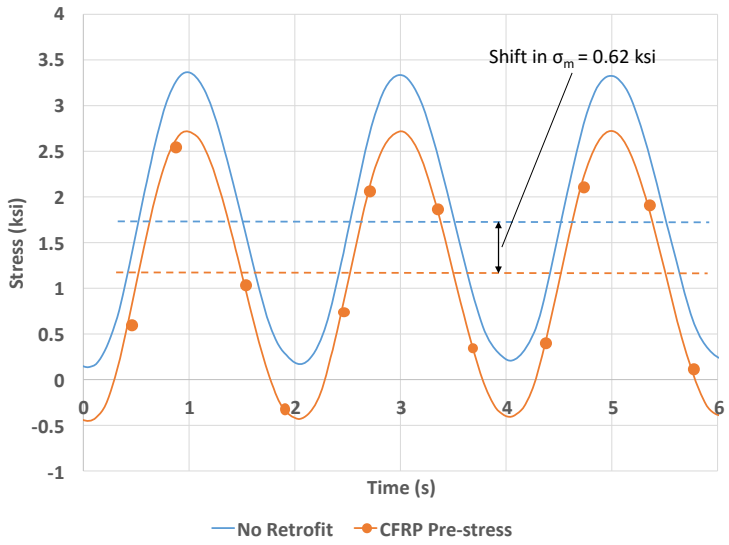

Figure 5-7: Shift in mean stress due to pre-stress under experimental testing

5.5. INVESTIGATION INTO BONDING STRATEGIES AND PRE-STRESS LOSS

In order for the CFRP retrofit to be effective, the bond between the retrofit components and existing steel sections must be capable of developing the CFRP pre-stress forces. Because the existing steel section surfaces may be corroded following years of exposure to harsh environments, quantifying bonding strengths between the retrofit and corroded steel surfaces is important. In addition to bonding strengths, pre-stress losses within the CFRP material, retrofit clamps, and bonding adhesives may affect retrofit performance over time. To investigate retrofit bonding strengths and pre-stress losses, experimental tests involving corroded steel plates, structural adhesives, prototypes of the developed retrofits, and local strain measurements were conducted. Figure 5-8 shows the initial test setup, where the retrofit is bonded to a corroded steel plate surface (representing a typical exposed steel girder surface) and instrumented with a uni-directional strain gauge for measurement of the initial applied pre-stress and resulting pre-stress losses. In the experimental setup shown in Figure 5-8, a two-part epoxy structural adhesive was used to bond the stainless steel retrofit component to the corroded steel plate.

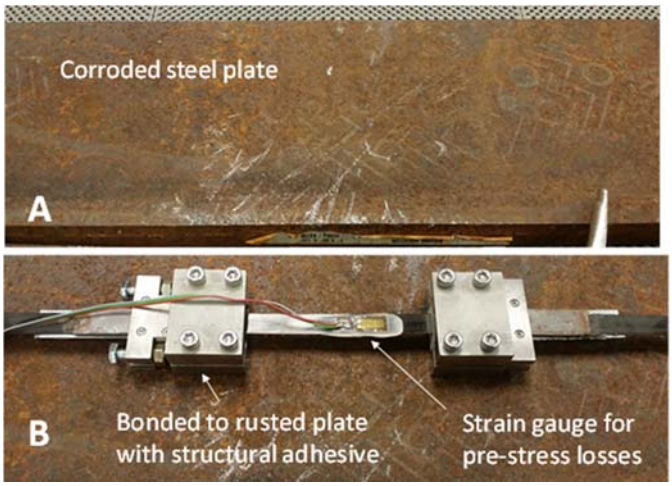

Figure 5-8: Corroded steel plate and bonded retrofit

During initial pre-stress, a corroded layer de-bonded from the steel plate, resulting in a complete loss of retrofit pre-stress. This de-bonding occurred at a CFRP pre-stress of near 70 ksi; however, it is important to note that the adhesive did not fail. Review of the

de-bonded clamp-holder surface indicated the removal of a corroded steel layer (see Figure 5-9). Figure 5-10(a) shows the pre-stress measurements for the retrofit-to-corroded-plate experiments.

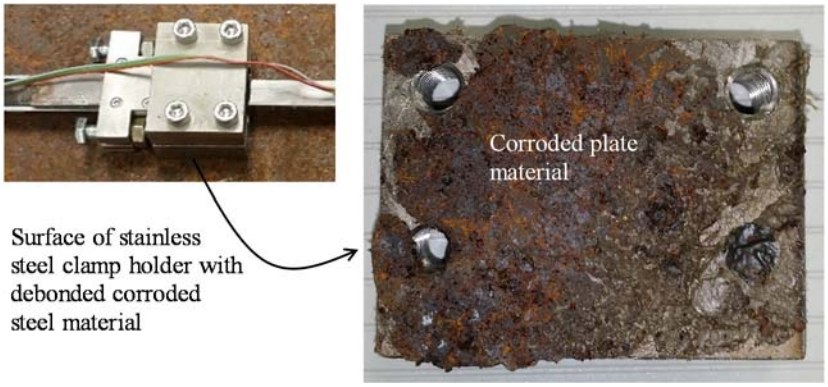

Figure 5-9: De-bonded retrofit with corroded plate material attached

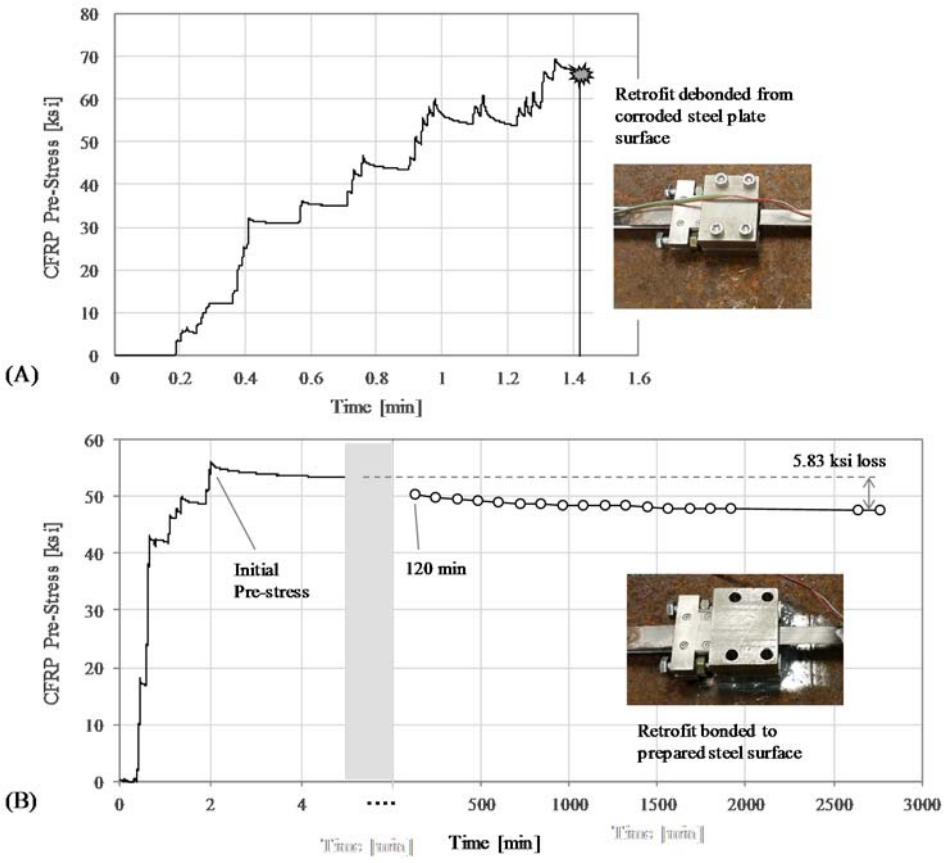

Figure 5-10: Pre-stress measurements for retrofits bonded to A) unprepared corroded steel surface, and B) prepared steel surface

Following the corrosion bond experiments, the steel plate surface was prepared by local grinding of the corroded layer, after which the retrofits were re-bonded using the two-part epoxy adhesive. Once the retrofit bond cured, a pre-stress of 56 ksi was applied to the CFRP and measurements were taken every two hours to gauge pre-stress losses. Figure 5-10(b) shows initial pre-stress and gradual pre-stress loss within the CFRP over the entire 2,760 min measurement window. As shown in Figure 5-10(b), relaxation at the friction-clamp-to-CFRP interface led to a total loss of 5.83 ksi over the initial two-day period, prior to the pre-stress stabilization. Alternative CFRP configurations, such as cylindrical CFRP rods with end chucks (similar to post-tension cable construction) may help reduce pre-stress losses.

6. LABORATORY INVESTIGATION OF PRESTRESSED CONCRETE CORROSION BEHAVIOR

The laboratory experiments consisted of the following process: construction of the prestressed concrete girders, end zone deterioration of those girders through the use of an accelerated corrosion setup, and shear testing of the girders. Nine prestressed concrete girder specimens were cast for testing in this project. Six were shear tested and three saved for later retrofit. An investigation of a potential retrofit design option was conducted and is also discussed in this report.

6.1. PRESTRESSED CONCRETE GIRDER SPECIMENS

The prestressed concrete girder specimens were designed to be half-scale AASHTO Type II girders with similar concrete compressive strength and in-service stress state as two full-scale decommissioned girders taken from the I-244 bridge over the Arkansas River in Tulsa, Oklahoma and tested as part of a complementary project. Since shear capacity in prestressed concrete beams is affected by the effective prestress, the beam designs were developed by adjusting the prestress configuration for the half-scale girders to obtain service level stress states equivalent to that of the full-scale girders within an acceptable range. The girders were designed through multiple iterations using a design spreadsheet based on the ACI and AASHTO methods and developed as part of the complementary project [45]. The design spreadsheet considered the concrete stress at release and in service. The girders were designed to replicate two full-scale girder

designs, Beam “A” and Beam “C”, from the original design drawings of the decommissioned bridge. Reinforcing steel was also designed to follow the reinforcement configuration of the original Beam “A” and Beam “C” girders from the drawing set provided by the Oklahoma Department of Transportation (see Appendix C for drawings of Beam “A” and Beam “C”, as well as screenshots of the design for the girders constructed for the project described in this report).

After many iterations, the half-scale girder design yielded the closest stress values when harped prestressing strands were used. However, the prestressing bed at Fears Structural Engineering Laboratory placed limitations on construction that would prevent the ability to use harped prestressing strands. The girder designs were updated to account for different prestressing strand locations with emphasis on straight strands only, transformed section properties, and stress equivalence in the in-service stress category.

The final design intended to match Beam “A” included two ½ in. special strands located at 4 in. from the bottom of the section with a 186 ksi prestress while the final design intended to match Beam “C” included two 0.6 in. strands at 4 in. with a 202.5 ksi prestress. The design called for a 2 in. of center-to-center spacing between the two prestressing strands. Both designs included shear reinforcement in the form of No. 3 Z bars. The designs also considered pretensioned anchorage zone reinforcement requirements and consistent concrete-to-steel shear strength contribution ratios between the full-scale and half-scale specimens. For the full-scale Beam “A”, it was determined that the total shear strength consisted of approximately 30% contribution from the concrete and 70% from the transverse reinforcing steel. Similarly, for the full-scale Beam “C” the contributions were approximately 29% from the concrete and 71% from the steel. The concrete-to-steel strength contribution ratios were determined using the design spreadsheet along with the transverse steel spacing and bar sizes. The concrete-to-steel strength contribution ratios at a distance equal to ¼ of the span from the support and h/2 from the support, the critical sections described in the various design codes, are presented in Table 6-1 and Table 6-2.

Table 6-1: Concrete-to-steel strength contribution ratios at L/4 from the support

Specimen Type	Concrete Contribution	Steel Contribution
Beam “A” (full scale ODOT)	31%	69%
Girder A (half-scale)	26%	74%
Beam “C” (full scale ODOT)	29%	71%
Girder C (half-scale)	19%	81%

Table 6-2: Concrete-to-steel strength contribution ratios at h/2 from the support

Specimen Type	Concrete Contribution	Steel Contribution
Beam “A” (full scale ODOT)	28%	72%
Girder A (half-scale)	26%	74%
Beam “C” (full scale ODOT)	29%	71%
Girder C (half-scale)	18%	82%

Also using the design spreadsheet, the girders were designed to have a stress state similar to the stress state of the original Beams “A” and “C” with a specific focus on the in-service compressive stress, which has the largest impact on shear capacity. The in-service stresses were based only of the effects of prestress and dead load. Table 6-3 and Table 6-4 present the concrete stress values at release and in service. When the formwork for the girders was constructed, the depth of the girder was 4.5 in. greater than anticipated, which increased the stresses in the actual specimens.

Concurrently with the design of the prestressed concrete girders, an approximately 58 ft-long prestressing bed were designed and constructed at Fears Lab. Steel formwork was designed and fabricated for construction of the girders. The prestressing bed consists of two steel abutments bolted to the Fears Lab strong floor and a wooden platform for supporting the formwork. It was designed to cast up to 48 ft of beam at one time. The prestressing bed has a “dead end” for strand anchorage at the south which has no moveable parts,and a “live end” at the north where the prestress is applied. The live end prestressing abutment and the overall prestressing bed are shown in Figure 6-1.

Table 6-3: Concrete stress values at release for Girder A and C designs

Stress Location	Beam “A” (full scale) (ksi)	Girder A (half-scale) (ksi)	Difference (%)	Beam “C” (full scale) (ksi)	Girder C (half-scale) (ksi)	Difference (%)
Section Top	-0.239	-0.056	76.5	-0.268	-0.018	93.3
Section Bottom	-1.151	-1.101	4.3	-1.871	-1.604	14.3

Note: (+) indicates compression, (-) indicates tension.

Table 6-4: Concrete stress values in service for Girder A and C designs

Stress Location	Beam “A” (full scale) (ksi)	Girder A (half-scale) (ksi)	Difference (%)	Beam “C” (full scale) (ksi)	Girder C (half-scale) (ksi)	Difference (%)
Section Top	-0.450	-0.211	53.1	-0.768	-0.176	77.1
Section Bottom	-0.903	-0.896	0.8	-1.31	-1.35	3.1

Note: (+) indicates compression, (-) indicates tension.

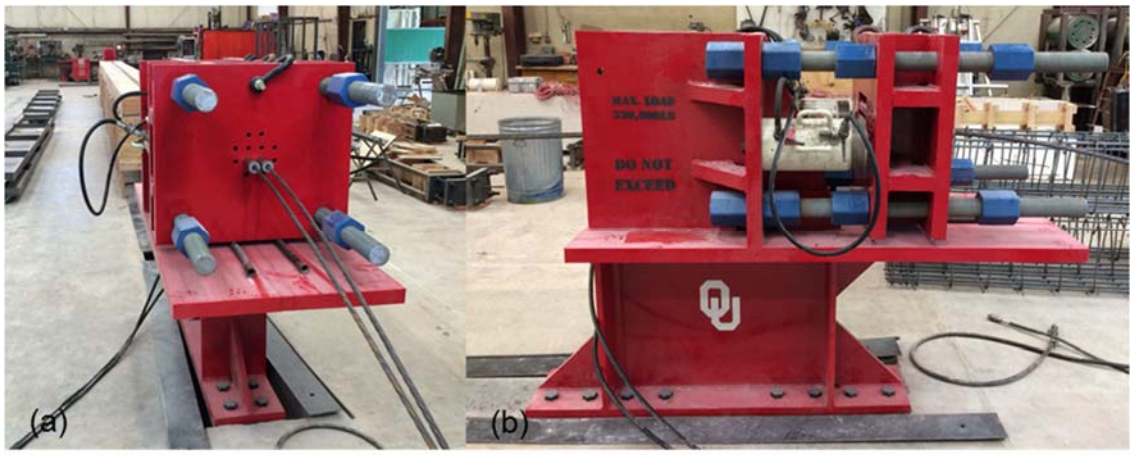

Figure 6-1: (a) View along the length of the prestressing bed at Fears Lab and (b) side view of the tensioning abutment

The concrete mix utilized to construct the beams was identified from mixes considered technically comparable to the original concrete design used for the full-scale girders based on compressive strength. The final mix design had a water/cement (*w*/*c*) ratio of 0.37, no entrained air, and a theoretical unit weight of 150.9 lb/ft^3. Table 6-5 presents the final proportions used for the concrete mix design.

Table 6-5: Concrete mix proportions used for casting girder specimens

Material	Quantity
Cement (lb/yd^3)	851
Sand (lb/yd^3)	1459
Rock (lb/yd^3)	1372
Water (lb/yd^3)	315
w/c	0.37
HRWR (oz/cwt)	5.0

Concrete compression tests were performed using 4 in. x 8 in. cylinders for quality control purposes and to ensure the required compressive strength for the girders was

achieved. The girders were cast using the prestressing bed over a period of five weeks. In total ten, 18-ft long girders were cast: four using the Girder A design (only three of these were used as there was a problem with consolidation for the first one cast), and six using the Girder C design. Three of the Girder C specimens were reserved for future retrofitting. The girders were cured for at least 28 days inside Fears Lab and then taken outside in preparation for the accelerated corrosion setup. Completed girder specimens are shown in in Figure 6-2.

Figure 6-2: Half-scale prestressed concrete girder specimens immediately before subjecting to the accelerated corrosion process

6.2. ACCELERATED CORROSION SETUP

After the girders were designed and cast, the next step was to begin the corrosion induced end-zone deterioration. As part of this effort, the corrosion accelerant process was developed. Initially, a literature review was performed to understand chloride solutions successfully used in previous research, as well as the optimum duration for wet/dry cycles of chloride saturated water. Ultimately, a 5 percent by weight chloride solution was chosen and sodium chloride was used for the solution. A large plastic tub was selected to serve as a reservoir, in which a submersible pump was installed to pour

the chloride solution over the end of the beams. Perforated plastic tubes were bonded to the beams approximately 6 in. from the beam ends. Four 3/32 in. diameter holes were drilled in the plastic tubes attached to each beam for the chloride solution to disperse over the beam ends. A valve was used to control the flow of the chloride solution through the perforated tubing. The final arrangement is shown in Figure 6-3. A cycle time of two hours on and two hours off was chosen based on the literature review, limitations of available timers, and to ensure drying between cycles.

After 28 days of curing for all beams, the beams were subjected to the wet/dry accelerated corrosion process. The exposure process adhered to the following:

a. Three girders, one from the Girder A and two from the Girder C reinforcement configuration, were subjected to the corrosion accelerant for two months.
b. Two girders, one from the Girder A and one from the Girder C reinforcement configuration, were subjected to the corrosion accelerant for four months.
c. Three girders, one from the Girder A and two from the Girder C reinforcement configuration, were subjected to the corrosion accelerant for six months.
d. One girder, from the Girder C reinforcement configuration, was subjected to the corrosion accelerant past six months, for a longer term exposure.

Figure 6-3: Corrosion accelerant setup (red arrows indicate the direction of flow from the perforated tubes)

The corrosion exposure setup was monitored throughout testing to ensure a consistent concentration of chloride. The progress of the corrosion was monitored to determine whether other measures should be taken, such as: inducing cracking into the end zones of the members to facilitate more moisture movement or applying an electrical current. Ultimately, there were no deviations from the originally designed accelerated corrosion setup. Cracks occurred during fabrication of some of the girders (e.g., during the prestress release) and the location of these cracks was recorded before starting the accelerated corrosion process on the girders.

6.3. SHEAR TESTING OF CORRODED SPECIMENS

Following the accelerated corrosion period, each end of the exposed specimens was tested in shear. A three point bending setup using a hydraulic actuator to apply load to the girders was used to simulate the maximum shear stress at the critical section used for shear design, and the load point location was chosen to induce a bond-shear type failure. The opposite end of the beam from that being tested overhung the support to prevent damage during the first test. The critical section for shear was determined by using a shear span to depth (a/d) ratio of 2. The critical section is important in that it is the location where a shear failure is more likely to be created as opposed to a moment induced failure. The support was located 4 in. from the end of the beam and the center-to-center distance between the supports was 9 ft; leaving 8 ft - 8 in. of overhang. A single point load was applied through a 6 in. wide plate, centered 41 in. from the end of the beam, using a hydraulic actuator. Sand was placed between the load plate and the beam to ensure uniform load distribution. The girders were loaded in 5000 lb increments before initial cracking, and 2000 lb increments after initial cracking to failure.

Deflection at the load point was measured using wire potentiometers (wire pots) on each side of the beam, strand end slip was measured using linear voltage differential transformers (LVDTs) attached to the prestressing strands on the non-corroded end and placed touching the strand ends on the corroded end. Manual deflection measurements were also taken after each load increment using a steel ruler. Visual mapping of cracking was conducted during the testing by marking cracks with a permanent marker and noting the load increments. Data was collected from all instruments during testing using a single data acquisition system. The data were used to compare the findings to the nominal

design/theoretical values calculated using the ACI and AASHTO LRFD codes and to identify the failure mechanism. The results of tests of the undamaged ends of the girders were compared to tests of the corroded girder ends to identify differences in performance. Figures 6-4 to 6-8 illustrate the shear test setup.

Figure 6-4: Typical shear test setup looking towards the north – (A) LVDT 1 & 2, (B) wirepots 1 (west) & 2 (east), (C) supports at 9 ft center-to-center, (D) single load point with load cell at 41 in. from end of beam, and (E) 8 ft - 8 in. overhang of the beam

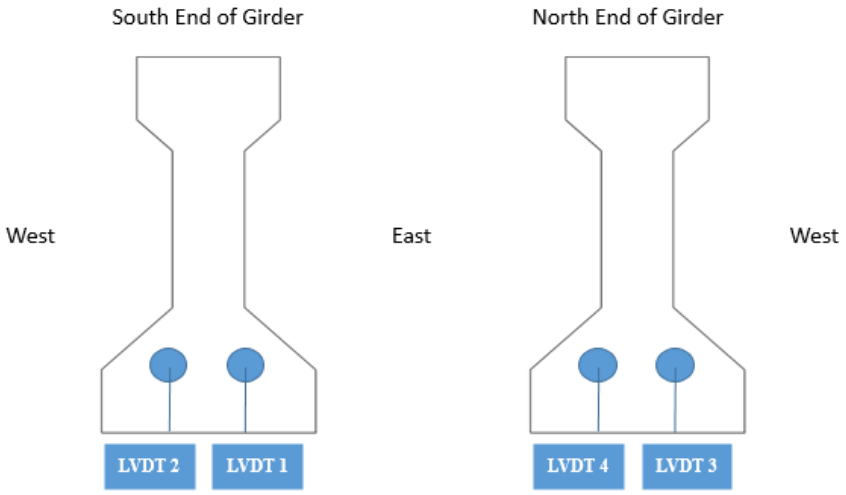

Figure 6-5: Location of LVDTs on prestressing strands at the girder ends during shear testing

Figure 6-6: Close-up of location (A) from figure 6-4 showing LVDT 1 (right) and LVDT 2 (left) – looking toward the north

Figure 6-7: View of the shear test setup looking toward the south and location (F) from Figure 6-4 showing LVDT 3 (right) & LVDT 4 (left), the load point, and supports

Figure 6-8: Close-up view of location (B) from Figure 6-4 looking toward the north showing wire pot 1 (left/west) and wire pot 2 (right/east)

6.4. RETROFIT OF REMAINING CORRODED SPECIMENS

The three remaining corroded girders were intended for retrofit designed using fiber reinforced polymer sheets and the information collected during shear testing of the first six corroded girders as part of the larger research project. A literature review was performed on the products related to this topic and to determine the general types that are applicable to this research effort. A Carbon Fiber Reinforced Polymer (CFRP) strip was selected for application the ends of the girders where shear strength is most critical. Great difficulty was encountered in obtaining retrofit materials and a greater focus was placed on field inspections to relate service conditions to laboratory data.

7. FIELD INSPECTIONS OF GIRDER ENDS

The Oklahoma bridge inventory was surveyed using the National Bridge Inventory (NBI) [46] and other available online resources [47] to assess the current state of deterioration in concrete bridges and identify those that fit desired specifications for field visits. The construction period of the bridges investigated was 1960 through 1979 in order to match the full-scale decommissioned girders. Site visits to a representative sample of these bridges were conducted to verify and document the levels of end region

deterioration in Oklahoma. Documentation and data were analyzed to identify common patterns, determine frequency of identified concerns, and ultimately, relate those identified concerns if possible to potential causes. As shown in Figure 7-1, the majority of concrete bridges in region 6 are either concrete culverts or stringer/multi-beam (girder) bridges. The focus of the study was placed on stringer/multi-beam (girder) bridges since these are the most common bridges using prestressed concrete girders. Only bridges in Oklahoma were considered for field visits due to logistical concerns.

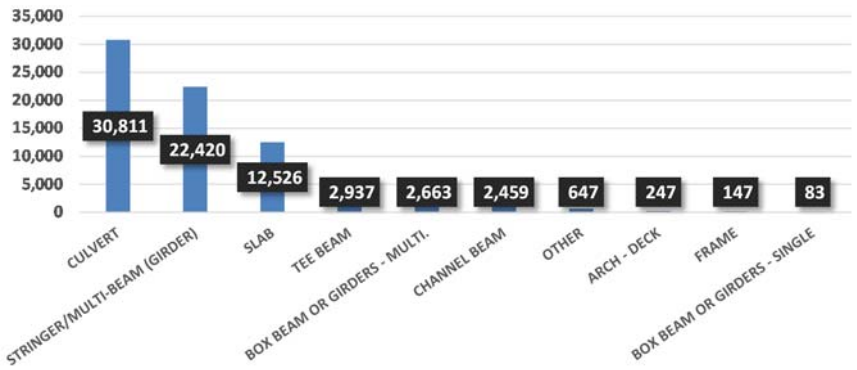

Figure 7-1: Distribution of concrete bridge types within Region 6.

7.1. BRIDGE SELECTIONS

All 22,912 bridges in Oklahoma, as represented by the data provided from the Federal Highway Administration's (FHWA) National Bridge Inventory (NBI), were filtered to select bridges for inspection as part of this research effort. Using the FHWA's Recording and Coding Guide for the Structure Inventory and Appraisal of the Nation's Bridges [48] (e.g. (Features Intersected (6A)), bridges were selected based on the following criteria:

- Features Intersected (6A): Did not include bridges with "river" and "creek"
- Construction Year (27): 1960-1979
- Design Load (31): M13.5/H15, M18/H20 and MS18/HS20 (same loading as the decommissioned bridge from the complementary project)
- Navigation Control (38): "N - Not Applicable, No waterway"
- Structure Open, Posted, or Closed to Traffic (41): "A - Open, no restriction"
- Type of Service under bridge: Highway, Railroad, Highway-Railroad

- Structure Kind (43A): 5 - Prestressed Concrete
- Structure Type (43B): 2 – Stringer/Multi-beam or Girder

These criteria were used to remove bridges that were: not constructed of prestressed concrete, spanned over rivers and creeks and thus were difficult to inspect, or were outside of the construction age this research intended to consider. The aforementioned criteria helped to narrow down the possible bridges to a more manageable 215 bridges. When considering the same design load as used for the decommissioned I-244 bridge in Tulsa County, the 116 listed in Table 7-1 Table remained, which is organized by Oklahoma Department of Transportation (ODOT) Field Division (see Figure 7-2).

Table 7-1: Bridges considered for a site visit by ODOT Field Division

ODOT Field Division	Number of Bridges (Total – 116)
1	19
2	29
3	1
4	23
5	1
6	0
7	8
8	35

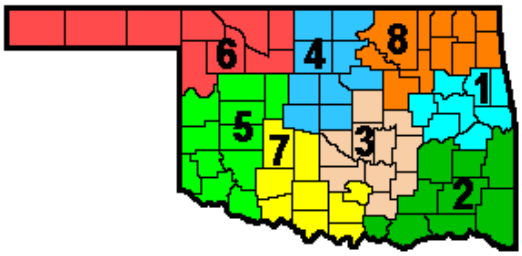

Figure 7-2: Geographical location of ODOT Field Divisions [49]

In the field, preference was placed on visiting bridges with significant ratings (i.e. lower) for the superstructure, or main load carrying system, of the bridge. The goal being to select and inspect bridges with a variety of superstructure ratings. Per the FHWA's Recording and Coding Guide [48], the superstructure rating is intended to describe the physical condition of all structural members. The Guide states the structural members

should be inspected for “signs of distress which may include cracking, deterioration, section loss, and malfunction and misalignment of bearings.” Also, bridges were pre-screened with available online resources (e.g., Google Maps) to determine potential traffic levels, and access issues.

7.2. PICTURE REFERENCE SYSTEM

Photos were taken of the overall bridge, each girder end, and any other pertinent locations for each bridge visited. These provided a visual record of the bridge condition at the time of the field visit. At each bridge, photos were taken of each girder end at the abutments along with any visual deficiencies such as cracking, spalling, and corroded bearing plates. For certain deficiencies to be more noticeable, a water bottle was used to spray the surface and highlight the area of concern. In order to have a uniform approach for referencing bridge locations, the following system was followed:

- The first set of numbers (e.g. 16606) is always the NBI structure number.
- The girders are numbered in sequential order with the northernmost girder (for east-west bridges) or westernmost girder (for north-south bridges) as first. Since the spans are (almost) always the end spans of the bridge they are not numbered but rather signified by their direction. Photos were taken of each side of each girder end resulting in north/south or west/east side photos of each girder.

An example photograph with label is shown in Figure 7-3.

In the example shown in Figure 7-3, “18554” is the NBI Structure #, “1W-N” means the picture is taken from the northern side (“N”) of the northernmost (“1”) girder on the western end (“W”) of the bridge. Figures 7-4 and 7-5 illustrate the picture reference system in a plan view layout of typical multi-span, multi-beam bridges.

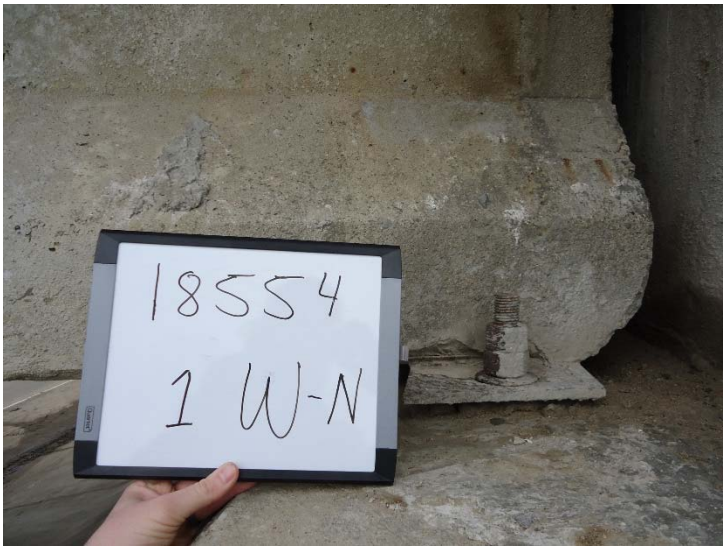

Figure 7-3: Bridge #18554, photo taken from northern side of the northernmost, west exterior girder

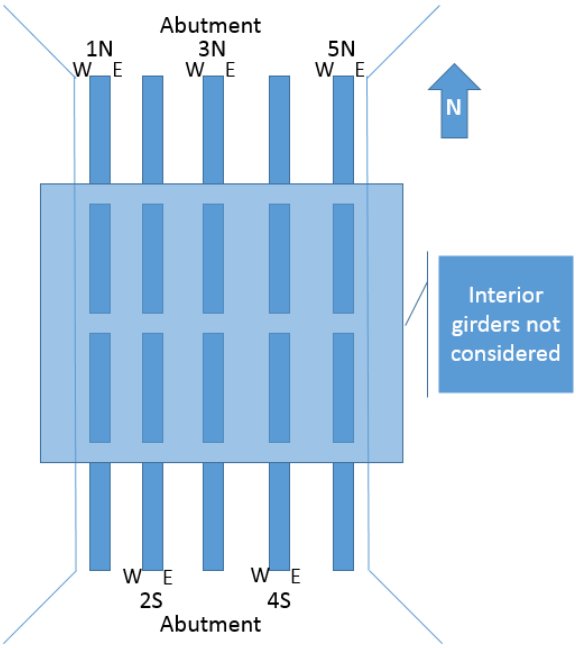

Figure 7-4: Plan view of an example north-south bridge using the picture reference system

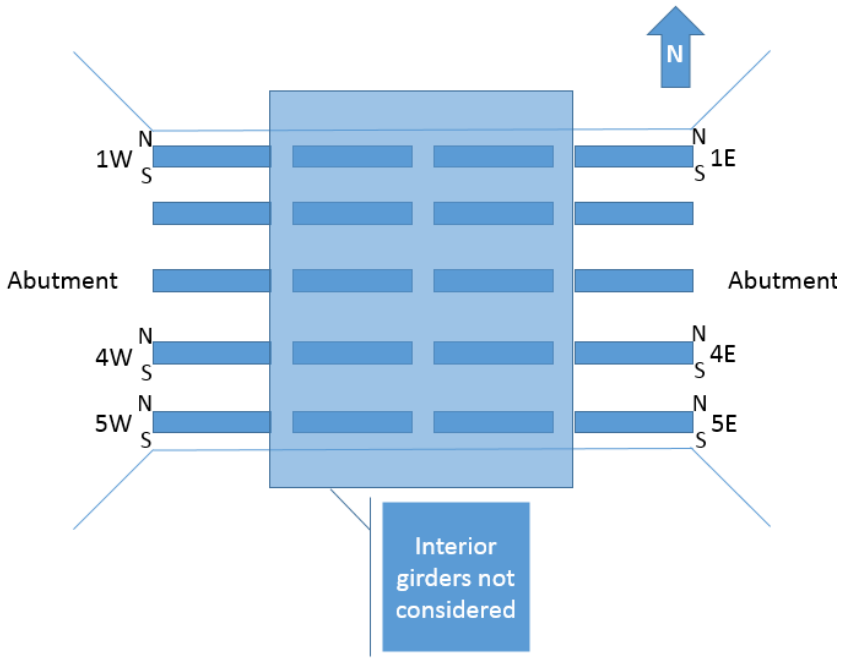

Figure 7-5: Plan view of an example east-west bridge using the picture reference system

8. RESULTS OF CONCRETE EXPERIMENTAL TESTING

8.1. COMPRESSIVE STRENGTH OF BEAMS

During the casting of the girders, cylinders were taken to perform compression tests at intervals of 1 day, 7 days, and 28 days. For each interval, three 4 in. x 8 in. cylinders were tested, and the compressive strength was calculated as an average of the results from each cylinder test. Table 8-1 shows the average compressive strengths for each time interval for all nine girders.

Table 8-1: Compressive strength of girder specimens

Girder	1 day Strength (psi)	7 day Strength (psi)	28 day Strength (psi)
A2	4,080	6,600	6,490
A3	5,400	6,820	7,000
A4	4,590	5,720	5,780
C1	5,650	6,890	7,600
C2	6,220	7,150	8,250
C3	5,030	6,740	7,050
C4	5,030	6,940	7,160
C5	4,320	5,630	6,140
C6	4,530	6,180	6,630

All of the measured compressive strengths were larger than the targeted compressive strength of 4,000 psi at prestress release (1-day). However, there was a relatively large variation in the measured strengths, with the maximum value being more than 50% larger than the target. The compressive strength of Girder A4 was 4% less than the design compressive strength of 6,000 psi at 28-days. The remaining girders exceeded the design compressive strength, but with relatively large variation. The maximum value was 37% greater than the design compressive strength. The variation in compressive strength has the potential to affect the prestress transfer and development lengths, as well as the girder's shear capacity. Larger compressive strengths would lead to shorter transfer and development lengths, and higher shear capacity.

8.2. SHEAR TESTS

The cracking load and failure load were determined via the notes taken during testing, along with the load-deflection data provided from the data acquisition system. The locations of the LVDTs and wire pots are referenced in Section 6.3 and shown in Figures 6-4 to 6-8. Whenever the north end of the girders was tested LVDTs 1 and 2 were not in use as the overhang did not allow for measuring the slip on that overhung end.

For the discussion to follow, the location of the shear test is abbreviated as follows: first the girder specimen identification number (i.e., A4), then the end of the girder (i.e., north or south), and lastly if it is the "corroded end" then a "C" follows. The label for the end of the girder identifies the location in the prestressing bed which may affect transfer length. The label is also significant in that the accelerated corrosion process was not consistently applied on one directional end (i.e., not all of the girders were corroded on the north end of the girders). As an example, in describing the corroded south end of Girder A4, the abbreviation is A4SC. A summary of the results of all shear tests is given in Table 8-2. The results of each test are presented in greater detail in the following sections.

Table 8-2: Failure mechanisms of girders during each shear test

Specimen	Test Age	Corrosion Accelerated End	Control End
Girder A4	2 months	Bond-shear failure; slip before flexural cracking	Bond-shear failure; flexural-shear cracking before slip
Girder C1	2 months	Bond-shear failure; slip before web-shear cracking	Bond-shear/flexure failure; flexural-shear cracking before slip; flange deterioration
Girder A3	4 months	Bond-shear failure; slip before flexural cracking	Bond-shear failure; maybe flexural failure first; flexural-shear cracking before slip
Girder C2	4 months	Bond-shear failure; slip before web-shear cracking	Bond-shear failure; cracking before slip
Girder A2	6 months	Web-shear failure; flexural cracking initially	Bond-shear failure; web-shear cracking before slip
Girder C3	6 months	Bond-shear/flexure failure; web-shear cracking before slip; concrete crushed at load point	Bond-shear failure; web-shear cracking before slip

8.2.1. Two-month Shear Testing

For the two-month shear testing of girders A4 and C1, the corroded end of the girders had a higher failure load than the control ends. The control end of girder A4 had a failure load of roughly 77% of the failure load for the corroded end. For girder C1, the control end failure load was roughly 83% of the corroded end failure load.

8.2.1.1. Specimen A4SC

Initial photos were taken of the girder before the testing began (Figure 8-1). The shear loading was increased in approximately 5 kip intervals until flexural cracking occurred at approximately 41 kips. The girder was then loaded in 2 kip intervals until the girder's failure at approximately 56 kips of load. A web shear crack appeared at failure, and more cracks formed under continued load. The load versus deflection graph (Figure 8-2) for this test illustrates that: the load-deflection relationship was mostly linear until the cracking load where the girder began to behave nonlinearly; at the cracking load deflection was roughly 0.15 in.; at the maximum load the deflection of the girder was approximately 0.36 in.; and the girder had a maximum deflection of almost 0.6 in.

Figure 8-1: Specimen A4SC before shear testing

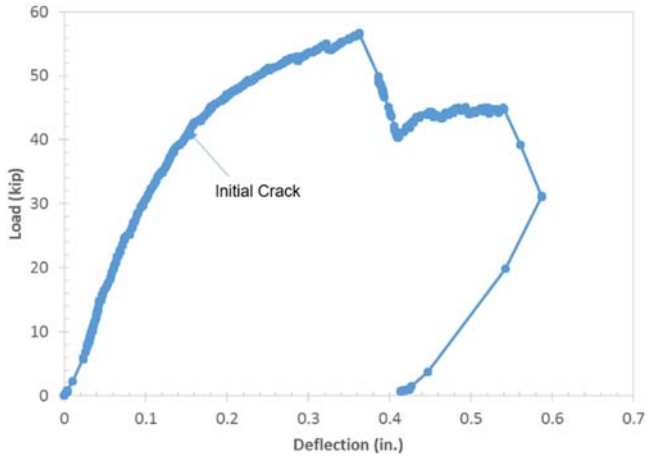

Figure 8-2: Load versus deflection for specimen A4SC

The load versus slip graph (Figure 8-3) shows that slip began simultaneously with the applied load. Results from LVDTs 3 and 4 were removed from the graph because the slip was approximately zero for these strands. LVDT 2 had more slip than LVDT 1, which was visible at the strand ends as shown in in Figure 8-4. As the graph illustrates, more than 0.08 in. of slip occurred before visible cracking of the girder began. The shear failure caused the slip to occur before the first flexural crack was visible. Figure 8-5 is a photo of the visual map of cracking that occurred during the shear testing of A4SC.

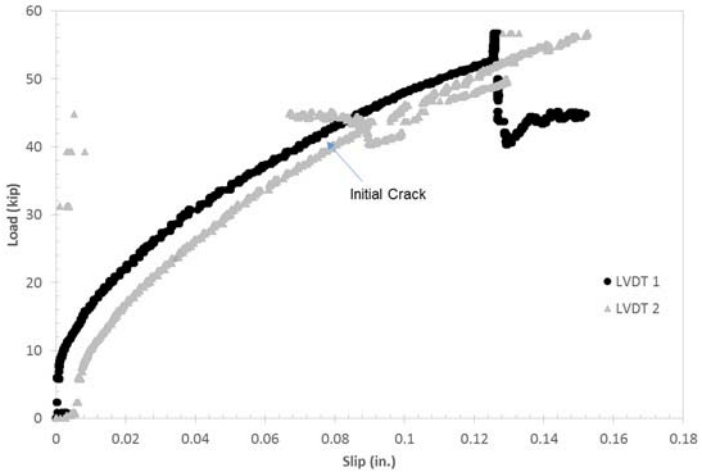

Figure 8-3: Load versus strand slip for specimen A4SC

Figure 8-4: Slip (a) during and (b) after shear test of specimen A4SC (LVDT 2 is on the left in each photo and LVDT 1 is on the right

Figure 8-5: Visual map of cracking for shear test of specimen A4SC

8.2.1.2. Specimen A4N

The north end of girder A4, the control end, was tested second. Initial photos were taken of the girder before the testing began (Figure 8-6). The cracking load, determined visually, was approximately 41 kips. The girder was then loaded with a 2 kip interval and further cracking occurred at 43 kips, after which the beam could take no further load. The beam was continuously re-loaded up to 43 kips until it became apparent that the beam had failed. A flexural-shear crack was the first crack that occurred followed by multiple web shear cracks by 43 kips of load. The load versus deflection graph (Figure 8-7) for this test illustrates that: the load-deflection relationship was mostly linear until the cracking load after which the load had quick decline; the beam did not take much additional loading past 41 kips; at the cracking load the deflection was approximately 0.07 in.; and the maximum deflection was roughly 0.58 in. The load versus slip graph (Figure 8-8) shows that slip appears to have occurred after cracking, and thus did not contribute to the shear failure. Figure 8-9 illustrates the cracking along the girder.

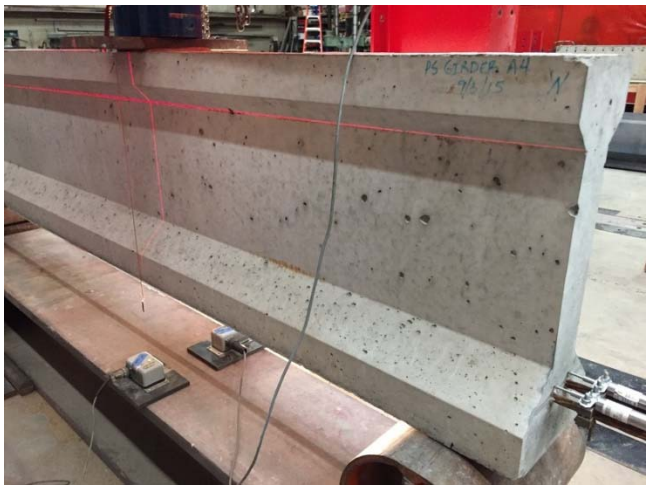

Figure 8-6: Specimen A4N before shear testing

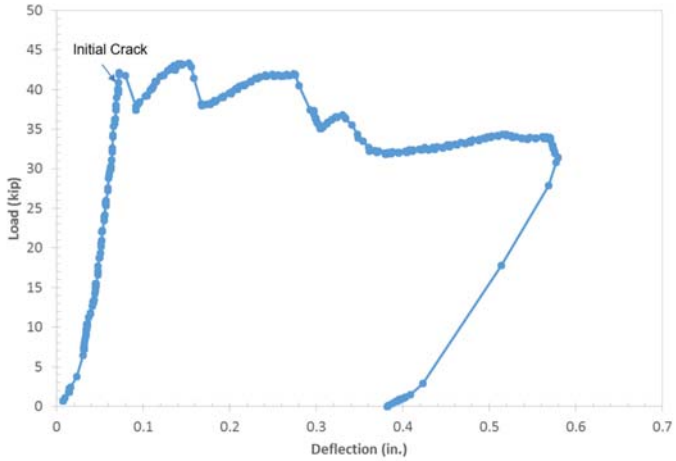

Figure 8-7: Load versus deflection for specimen A4N

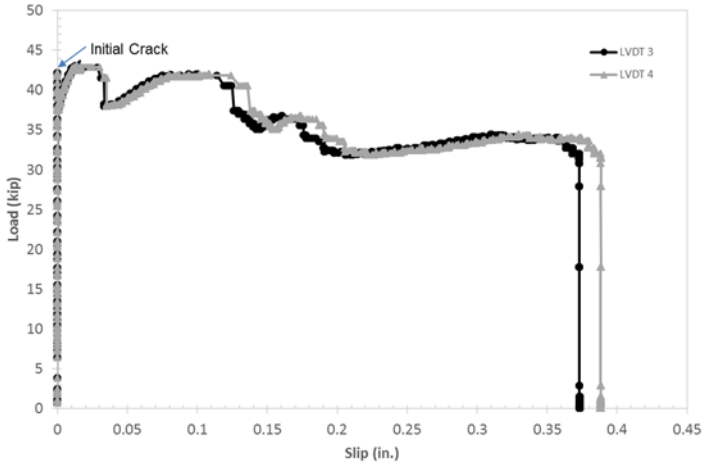

Figure 8-8: Load versus strand slip for specimen A4N

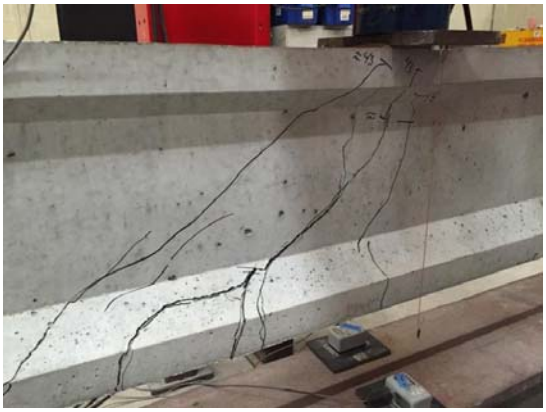

Figure 8-9: Visual map of cracking for shear test of specimen A4N

8.2.1.3. Specimen C1NC

For girder specimen C1, the north end of the girder was tested first. The north end of the girder was also the end exposed to the accelerated corrosion setup. Initial photos were taken of the girder before the testing began (Figure 8-10). Web-shear cracking occurred from the bottom of the flange up towards the load point at a load of approximately 45 kips, and the beam failed at a load of approximately 52 kips. The girder exhibited both horizontal and inclined shear cracks, typically indicative of a bond failure. The load versus deflection graph (Figure 8-11) for this test illustrates that: the load-deflection relationship was mostly linear until the cracking load where the beam began to behave nonlinearly; at the cracking load the deflection was roughly 0.05 in.; and the maximum deflection was approximately 0.64 in.

The load versus slip graph (Figure 8-12) shows that the slip occurred at the same time the loading began. LVDTs 3 and 4 were removed from the graph because the slip was approximately zero for these strands. LVDT 1 seemed to be out of its effective range, and also did not measure any slip. Approximately 0.08 in. of slip was measured by LVDT 2 before visible cracking of the beam began. Figure 8-13 shows a visual map of the cracking that took place during the shear testing. The web-shear cracks had a width between roughly 0.25 in. and 0.35 in. Figure 8-14 illustrates the visible slip of the strand measured by LVDT 2.

Figure 8-10: Specimen C1NC before shear testing

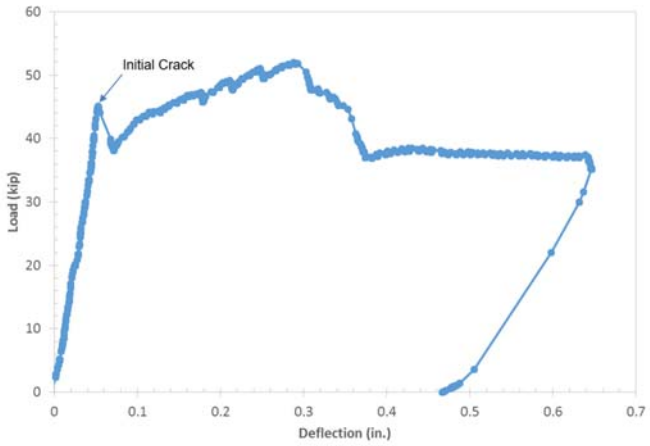

Figure 8-11: Load versus deflection for specimen C1NC

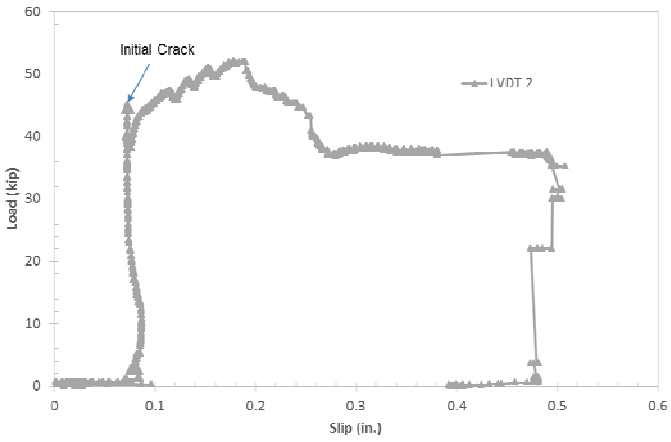

Figure 8-12: Load versus strand slip for specimen C1NC

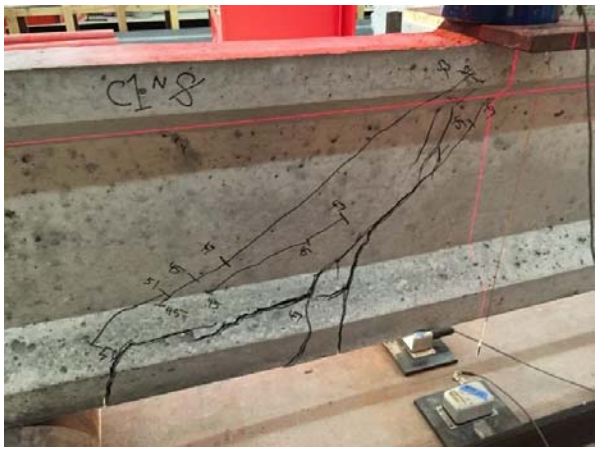

Figure 8-13: Visual map of cracking for shear test of specimen C1NC

Figure 8-14: Visible strand slip for LVDT 2 (left) after shear test of specimen C1NC

8.2.1.4. Specimen C1S

The south end of girder C1, the control end, was tested after the corroded end. Initial photos were taken of the girder before the testing began (Figure 8-15). Cracking occurred at a load of approximately 28 kips, after which the girder was loaded in 2 kip intervals until the beam failed at a load of approximately 43 kips. A flexural-shear crack was the first crack that occurred, then by 43 kips, multiple web shear cracks, as well as a horizontal crack near the strands appeared along the beam. At the widest, the main flexural-shear crack was approximately 0.3 in. wide. The load versus deflection graph (Figure 8-16) for this test illustrates that: the load-deflection relationship was mostly linear until the cracking load; the relationship then became nonlinear; and the maximum deflection was approximately 0.7 in. The load versus slip graph (Figure 8-17) shows that slip occurred after cracking, and thus did not contribute to the shear failure. The flange did separate at the top as evident by Figure 8-18, so this could be considered a bond-shear/flexure failure. Figure 8-19 shows the visual map of cracking of the girder during the shear test.

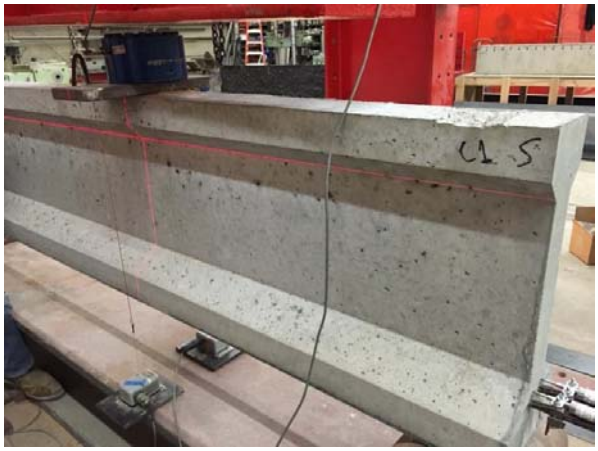

Figure 8-15: Specimen C1S before shear testing

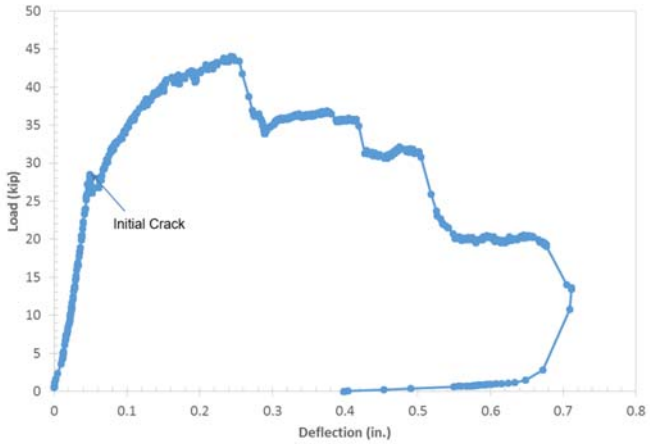

Figure 8-16: Load versus deflection for specimen C1S

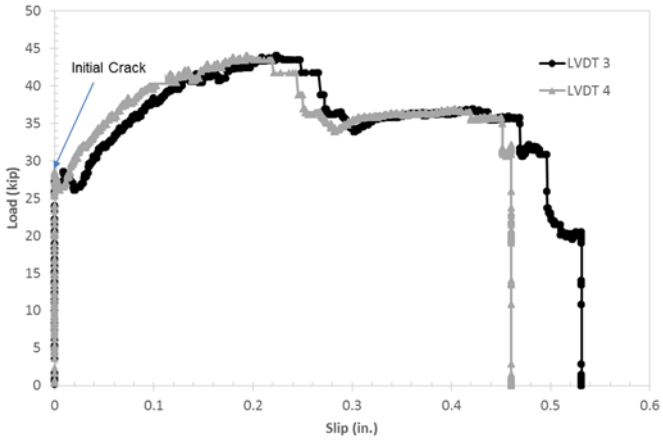

Figure 8-17: Load versus strand slip for specimen C1S

Figure 8-18: Specimen C1S upon completion of shear test

Figure 8-19: Visual map of cracking for shear test of specimen C1S

8.2.2. Four-month Shear Testing

For the four-month shear testing of girder specimen A3, the corroded end of the specimen had a higher failure load than the control, or non-corroded end. However, for girder specimen C2, the opposite was true – the corroded end had a lower failure load than the control end. The control end however was tested first this time, as opposed to the previous tests. The control end of girder specimen A3 had a failure load of roughly 87% of the corroded end. For girder specimen C2, the non-corroded end failure load was roughly 122% of the corroded end failure load.

8.2.2.1. Specimen A3SC

For girder specimen A3, the south end of the specimen was tested first. The south end of the specimen was also the end exposed to the accelerated corrosion setup. Flexural cracking occurred at approximately 45 kips. The girder was then loaded in 2 kip intervals until the beam's failure at approximately 57 kips when a large web-shear crack appeared. The load versus deflection graph (Figure 8-20) for this test illustrates that: the load-deflection relationship was mostly linear until the cracking load where the beam began to behave nonlinearly; the deflection at the cracking load was approximately 0.07 in.; and the maximum deflection was slightly more than 0.2 in. Figure 8-21 illustrates the cracking of the girder during and after the shear test. The measured slip data was not conclusive, and therefore is not presented.

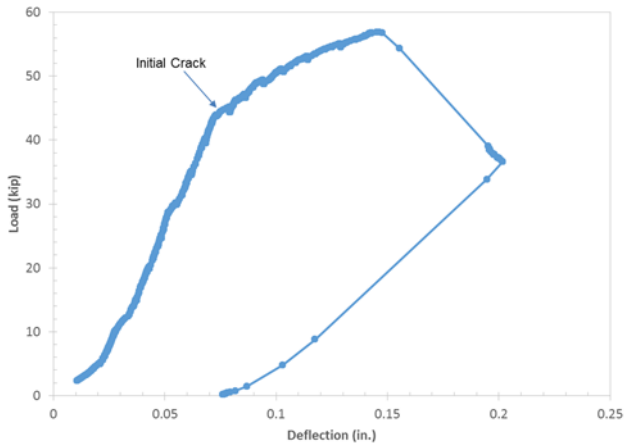

Figure 8-20: Load versus deflection for specimen A3SC

Figure 8-21: Visual map of cracking for shear test of specimen A3SC

8.2.2.2. Specimen A3N

The north end of girder specimen A3N, the control end, was tested after the corroded end. Cracking occurred at approximately 46 kips. The girder was then loaded in 2 kip intervals until further cracking occurred at 50 kips at which time much load was lost and the beam was reloaded until it failed completely at 41 kips. The load versus deflection graph (Figure 8-22) for this test illustrates that: the load-deflection relationship was mostly linear with small deformations until the cracking load; the beam was reloaded to about 50 kips when more cracking and a larger deflection occurred: and the beam was loaded until it failed completely and was left with a maximum deflection of approximately 0.74 in. The load versus slip graph (Figure 8-23) shows that slip was not measured until after

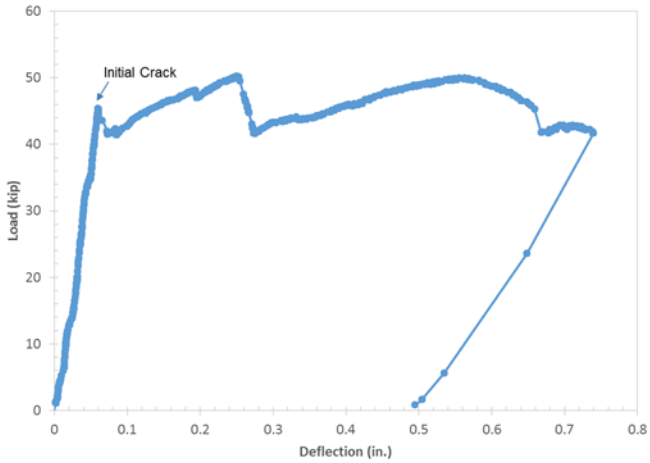

Figure 8-22: Load versus deflection for specimen A3N

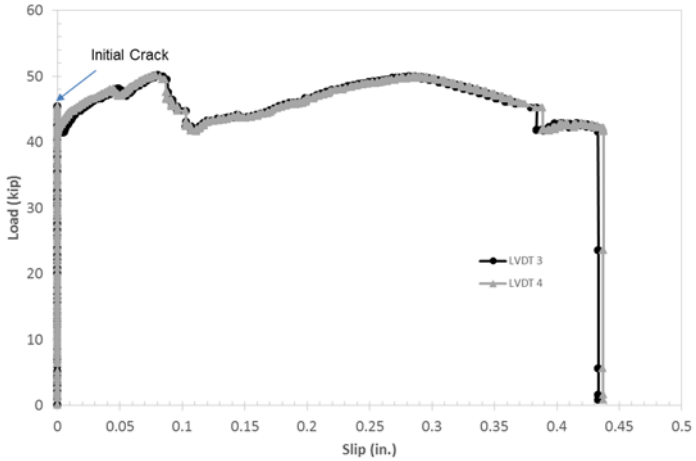

Figure 8-23: Load versus strand slip for specimen A3N

cracking, and thus did not contribute to the shear cracking, but resulted from it. A bond failure occurred as the total measured strand slip was greater than 0.4 in. Figure 8-24 shows the visual map of cracking for the shear test of specimen A3N.

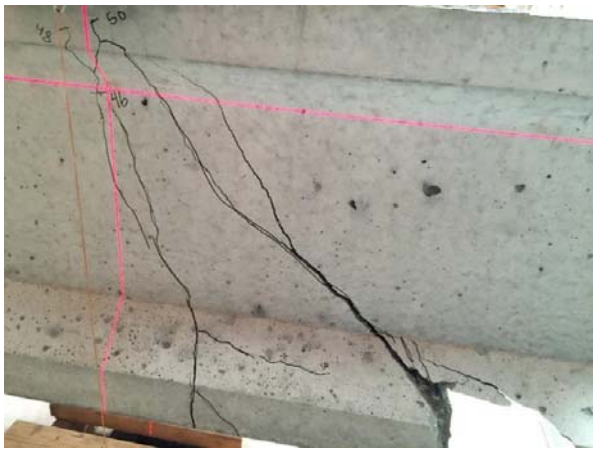

Figure 8-24: Visual map of cracking for shear test of specimen A3N

8.2.2.3. Specimen C2NC

The north end of girder specimen C2 was the end exposed to the accelerated corrosion setup and was the second end tested. Initial photos were taken of the girder before the testing began and a horizontal crack below the web/bottom flange interface of the girder (Figure 8-25 and Figure 8-26) was observed. Failure occurred at approximately 40 kips. A large web-shear crack appeared when the beam began to fail, and widened

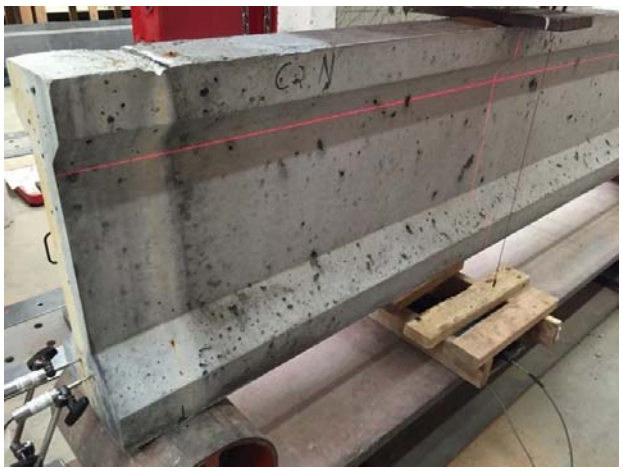

Figure 8-25: Initial condition of specimen C2NC

Figure 8-26: Horizontal crack below the web/flange interface of specimen C2NC before testing

and extended as additional load was applied. The load versus deflection graph (Figure 8-27) for this test illustrates that: the load-deflection relationship was mostly linear until the cracking/failure load; there then was a long residual load curve with the beam supporting a reduced load. The maximum measured deflection for the girder was approximately 0.65 in. The measured strand slip is presented in Figure 8-28. The data from LVDT 2 was unreliable, so the data from that sensor is not presented. Strand slip could have contributed to the shear failure, as more than 0.05 in. of slip occurred before visible cracking of the beam began. Figure 8-29 shows the visual map of cracking on the girder.

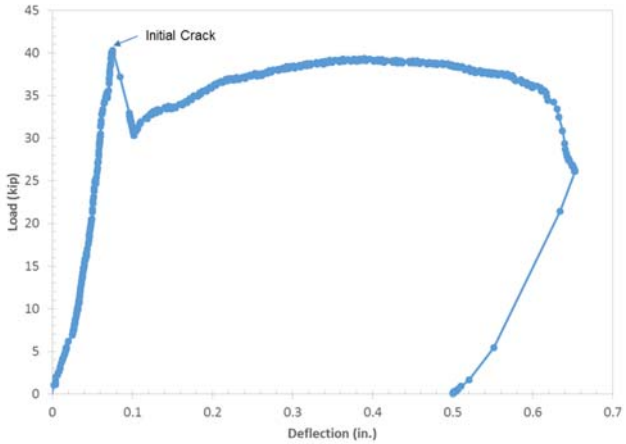

Figure 8-27: Load versus deflection for specimen C2NC

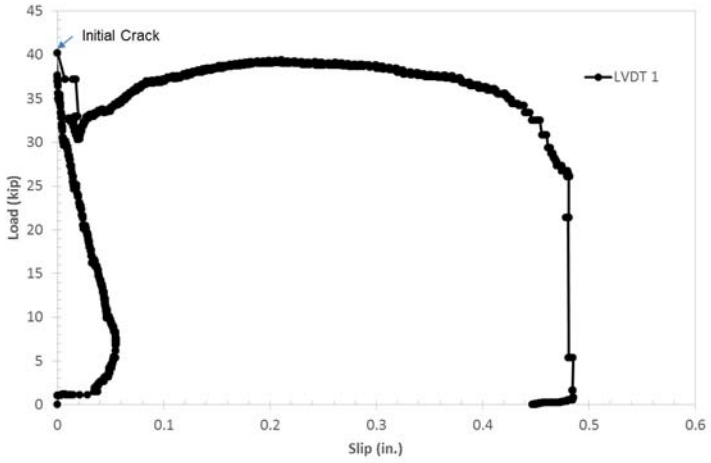

Figure 8-28: Load versus strand slip for specimen C2NC

Figure 8-29: Visual map of cracking for shear test of specimen C2NC

8.2.2.4. Specimen C2S

The south end of girder specimen C2, the control end, was tested before the corroded end. Cracking occurred at a load of approximately 45 kips, and the girder was loaded until failure at approximately 49 kips. The load versus deflection graph (Figure 8-30) for this test illustrates that: the load-deflection relationship was mostly linear until the failure load; the beam was reloaded slightly until it was apparent that the beam had failed; and there was a large residual capacity, with a maximum deflection of approximately 0.7 in. The load versus slip graph (Figure 8-31) shows the nonlinear relationship between the load and measured slip. A bond failure occurred as the strand slip was slightly greater than

0.43 in. Slip appears to have occurred after cracking, and thus did not contribute to the shear failure, but was caused by shear cracking. Figure 8-32 shows the visual map of cracking for specimen C2S.

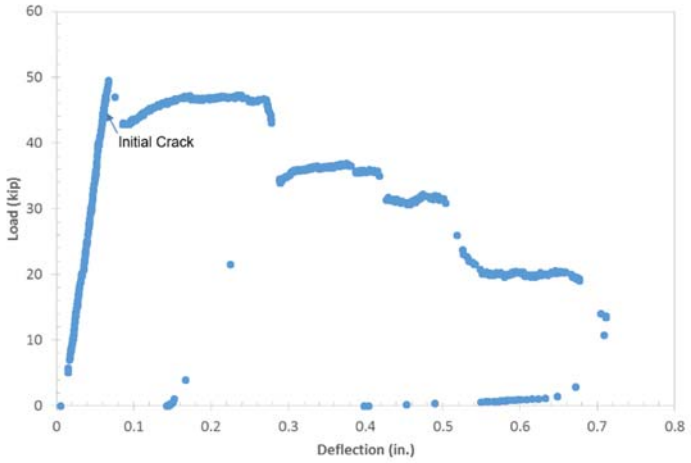

Figure 8-30: Load versus deflection for specimen C2S

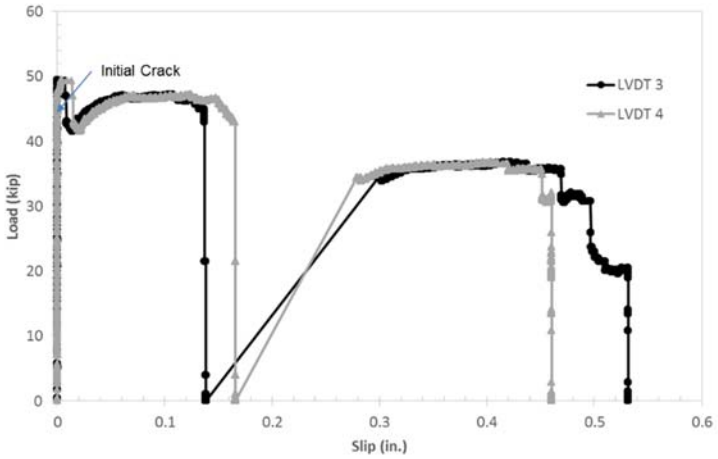

Figure 8-31: Load versus strand slip for specimen C2S

Figure 8-32: Visual map of cracking for shear test of specimen C2S

8.2.3. Six-month Shear Testing

For the six-month shear testing of girder specimens A2 and C3, the corroded end had a higher failure load than the control end. The control end of girder specimen A2 had a failure load roughly 51% of that for the corroded end. For girder specimen C3, the control end failure load was roughly 51% of the corroded end failure load.

8.2.3.1. Specimen C3NC

The north end of girder specimen C3, the end exposed to the accelerated corrosion setup was tested first. Before shear testing, photos were taken to document the condition (Figure 8-33). First cracking occurred at a load of approximately 45 kips, and the beam failed at a load of approximately 53 kips. The load versus deflection graph (Figure 8-34) for this test illustrates that: the load-deflection relationship was mostly linear until the cracking load; the first crack caused additional deflection of the beam; additional load caused a nonlinear relationship between the load and deflection; and the maximum deflection was recorded at slightly more than 0.5 in. The load versus slip graph (Figure 8-35) shows slip occurring after cracking of the girder had initiated. Results from LVDTs 3 and 4 were not included because the measured slip was approximately zero for these strands. The girder had multiple web-shear cracks at the time of failure (Figure 8-36). The top flange of the girder also exhibited crushing at the load point (Figure 8-37).

Figure 8-33: Initial condition of specimen C3NC before testing

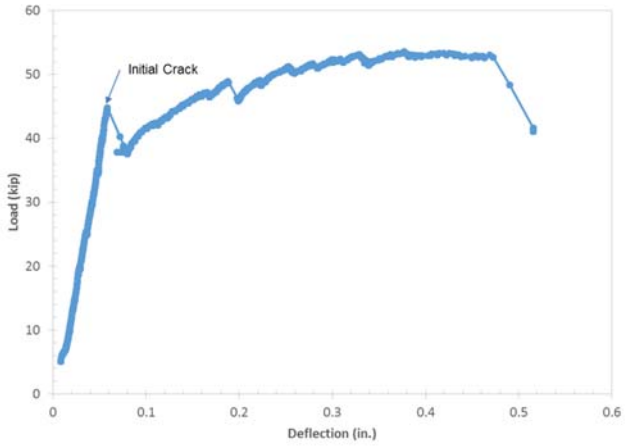

Figure 8-34: Load versus deflection for specimen C3NC

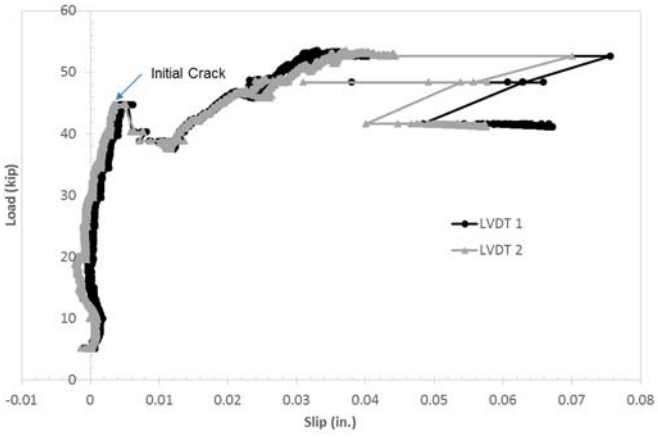

Figure 8-35: Load versus strand slip for specimen C3NC

Figure 8-36: Shear cracking of C3NC after shear test

Figure 8-37: Concrete crushing at top of top flange at failure of specimen C3NC

8.2.3.2. Specimen C3S

The south end of girder specimen C3, the control end, was tested second. Initial cracking in the form of web shear cracks occurred at a load of approximately 29 kips which was the maximum load sustained by the specimen. The load versus deflection graph (Figure 8-38) for this test illustrates that: the load-deflection relationship was approximately linear until the cracking/maximum load; after cracking the beam exhibited additional deflection at a fairly constant residual load of approximately 26 kips; and the maximum deflection was roughly 0.36 in. The load versus strand slip graph (Figure 8-39) shows no slip for LVDT 4 before cracking and only minimal slip for LVDT 3 indicating that

slip was caused by shear cracking. A bond failure occurred as the measured strand slip was greater than 0.3 in. A number of web shear cracks were observed near the support along with cracking on the underside of the beam (Figure 8-40 and Figure 8-41).

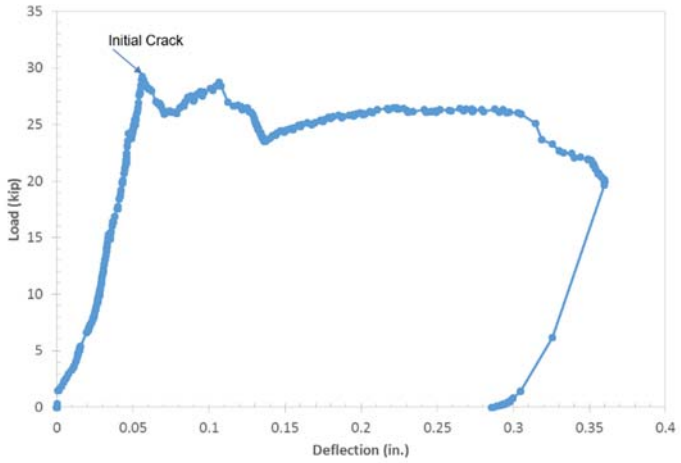

Figure 8-38: Load versus deflection for specimen C3S

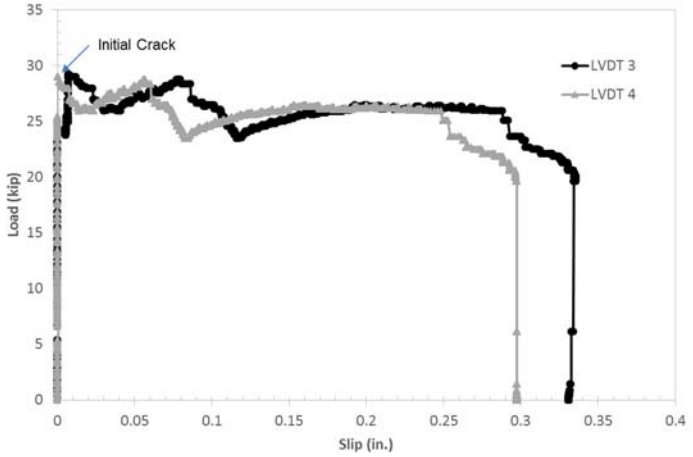

Figure 8-39: Load versus strand slip for specimen C3S

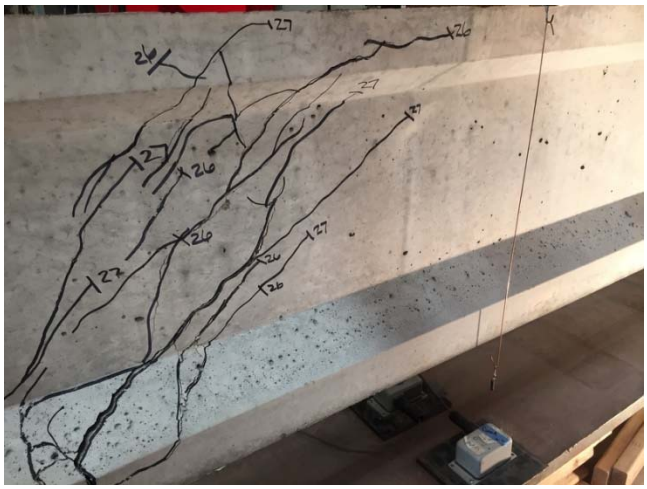

Figure 8-40: Visual map of cracking for specimen C3S

Figure 8-41: Cracking near the support and in the end of specimen C3S

8.2.3.3. Specimen A2SC

The south end of girder A2, the end exposed to the accelerated corrosion setup, was tested first. Prior to testing, photos were taken of the girder (Figure 8-42) to document its initial condition. Initial flexural cracking occurred at approximately 47 kips, and the beam failed at approximately 57 kips. The load versus deflection graph (Figure 8-43) for this test illustrates that: the load-deflection relationship was approximately linear until the cracking load; after the cracking load, the curve was still relatively linear, but had a smaller slope after cracking; and the failure load caused a sudden increase in deflection of the beam. The girder specimen exhibited multiple web shear cracks and one large

flexural crack at the time of failure (Figure 8-44). While slip was visually observed during this test (Figure 8-45), the data from the LVDTs did not prove reliable upon investigation after completing the shear test, and therefore is not presented.

Figure 8-42: Condition of specimen A2SC prior to testing

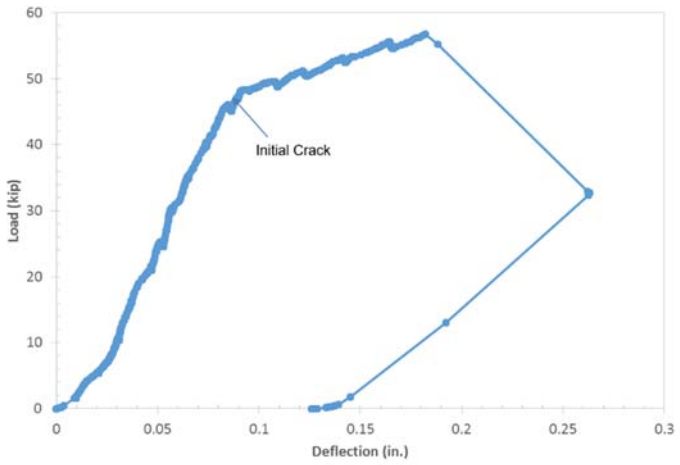

Figure 8-43: Load versus deflection for specimen A2SC

Figure 8-44: Visual map of cracking for specimen A2SC

Figure 8-45: Visible strand slip after testing specimen A2SC

8.2.3.4. Specimen A2N

The north end of girder specimen A2, the control end, was tested after the corroded end. Prior to testing, photos were taken of the girder (Figure 8-46) to document the initial condition compared to the corroded end. Initial cracking in the form of web shear cracks occurred at a load of approximately 25 kips. The load versus deflection graph (Figure 8-47) for this test illustrates that: the load-deflection relationship was approximately linear until the cracking load; after the cracking load, the beam exhibited a

sudden loss of load with increased deflection; the beam sustained a load in the 27-29 kips range as loading was continued until apparent failure; and the maximum deflection was approximately 0.38 in. The load versus strand slip graph (Figure 8-48) shows that slip appears to have occurred after cracking, and thus did not contribute to the shear failure, but that shear cracking caused the strand slip. Measured slip increased as the beam was loaded beyond cracking. A bond failure occurred as the strand slip was greater than 0.38 in. Web shear cracking was observed near the support and a vertical crack was observed on the beam end near one of the strands (Figure 8-49 and Figure 8-50).

Figure 8-46: Condition of specimen A2N prior to testing

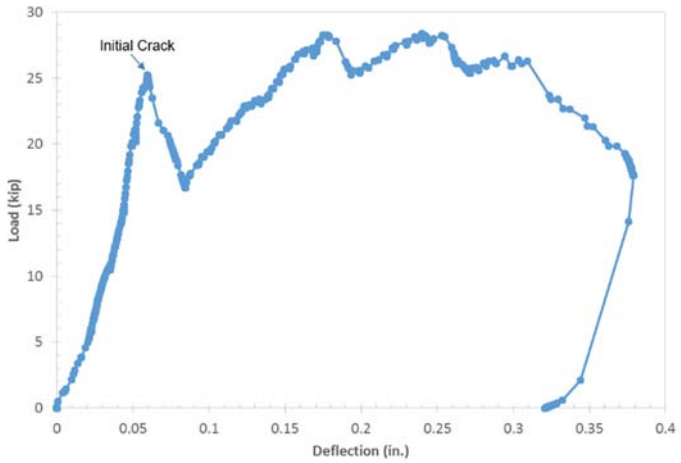

Figure 8-47: Load versus deflection for specimen A2N

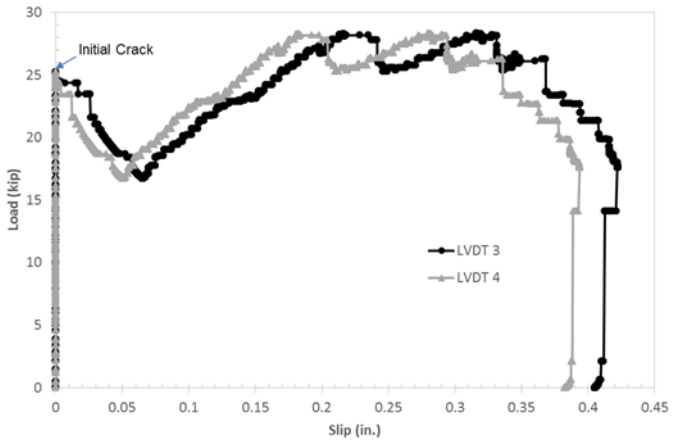

Figure 8-48: Load versus strand slip for specimen A2N

Figure 8-49: Cracking along the flange and web for specimen A2N

Figure 8-50: Cracking near the prestressing strands at the end of specimen A2N

8.2.4. Experimental Results Summary

Table 8-3 compares the design flexural and shear capacity values for each girder specimen to the measured values for each shear test. For example, for specimen A4SC, the failure load (P_{max}) of 56 kips corresponds to a maximum applied moment (M_{max}) of 113 k-ft., and a maximum applied shear (V_{max}) of 36.5 kips. The design values for specimen A4SC are 126.2 kip-ft for the moment capacity (M_n) calculated using strain compatibility, 25.5 kips for the shear capacity (V_n) using the AASHTO LRFD 2007 [51] method, 27.2 kips for the shear capacity (V_n) using the AASHTO LRFD 2012 [51] method, and 53.4 kips for the shear capacity (V_n) using the ACI [52] detailed method.

Table 8-3: Design and experimental capacity values for each shear test specimen

Test	P_{max} (kips)	M_{max} (kip-ft)	V_{max} (kips)	M_n (kip-ft)	V_n LRFD 2007 (kips)	V_n LRFD 2012 (kips)	V_n ACI (kips)
A4SC	56	113.0	36.5	126.2	45.5	27.2	53.4
A4N	43	86.6	27.9	126.2	45.5	27.2	53.4
C1NC	52	104.9	33.8	165.7	46.6	27.7	59.1
C1S	43	56.6	27.9	165.7	46.6	27.7	59.1
A3SC	57	115.0	37.1	127.3	46.5	27.8	55.1
A3N	50	100.8	32.5	127.3	46.5	27.8	55.1
C2NC	40	80.6	26.0	166.4	47.1	27.9	60.0
C2S	49	98.8	31.9	166.4	47.1	27.9	60.0
C3NC	53	106.9	34.5	165.0	46.2	27.4	58.3
C3S	29	58.3	18.7	165.0	46.2	27.4	58.3
A2SC	57	115.0	37.1	126.9	46.0	27.5	54.1
A2N	29	58.3	18.7	126.9	46.0	27.5	54.1

Note: Subscript “max” indicates experimentally measured values, subscript “n” indicates design values

Figure 8-51 illustrates the design and measured shear values for each girder for comparison. Overall, the measured shear values were less than the design shear capacity (ACI and AASHTO LRFD 2007 methods) for each girder. The measured compressive strengths were used to calculate shear capacities, which should account for the variation in compressive strength related to concrete shear strength. The a/d ratio used for all tests was 2.0, which is near the limiting value for the methods given by the codes and may have reduced the applicability of the code equations. Due to variation in compressive strengths, transfer lengths may have differed from the estimates used during calculation of shear capacity either greater or smaller.

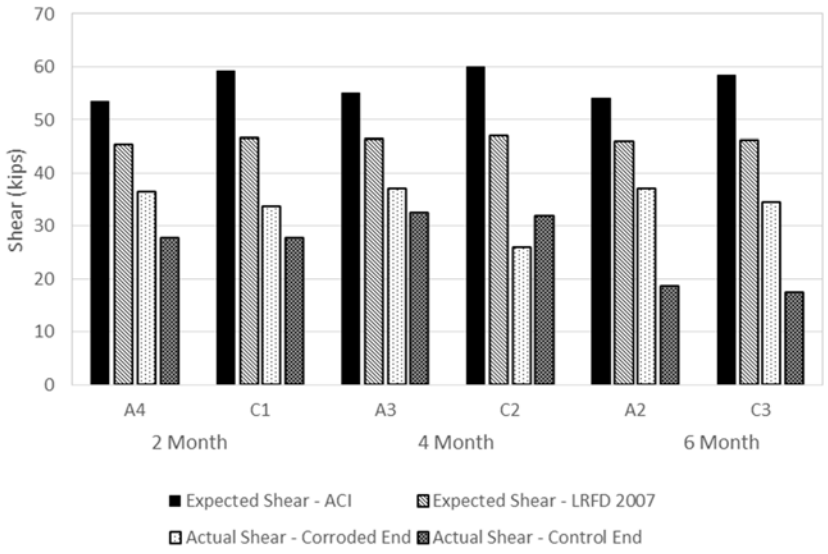

Figure 8-51: Design shear capacity compared to measured shear at failure for each specimen

All of the corroded ends had a larger measured shear than the control end, except for girder specimen C2. Similar results were shown by Abosrra et al. [29] for minor corrosion. With the exception of girder specimen C2, the corroded end of each girder was tested first. The order of testing could have potentially impacted the condition of the beam, thereby impacting the remaining end and resulting in less resistance available. The corroded ends of the girders may have had a larger measured shear due to increased compressive strength resulting from curing from the moisture provided by the accelerated corrosion process which was applied shortly after the theoretical curing process. No additional curing water was provided for the rest of each specimen. For many of the girders, the prestressing strands slipped prior to cracking of the beam. This slip is believed to have caused the beams to failure sooner than they otherwise would have. The control ends of girder specimens A2 and C3, exposed for six months, had a significantly smaller measured shear than the other tested control ends. There is no clear evidence as to why this occurred.

Figure 8-52 and Figure 8-53 illustrate the varying failure loads by girder design. Overall, the corroded ends of the girders with the Girder A design sustained a larger failure load than those corroded ends of the girders with the Girder C design. The larger

diameter of the 0.6 in. strands used in the Girder C design may have contributed to earlier slip and reduced capacity. Further research could explain if the larger strands in the Girder C design contributed a greater likelihood for strand slip, and in turn failure at a smaller load.

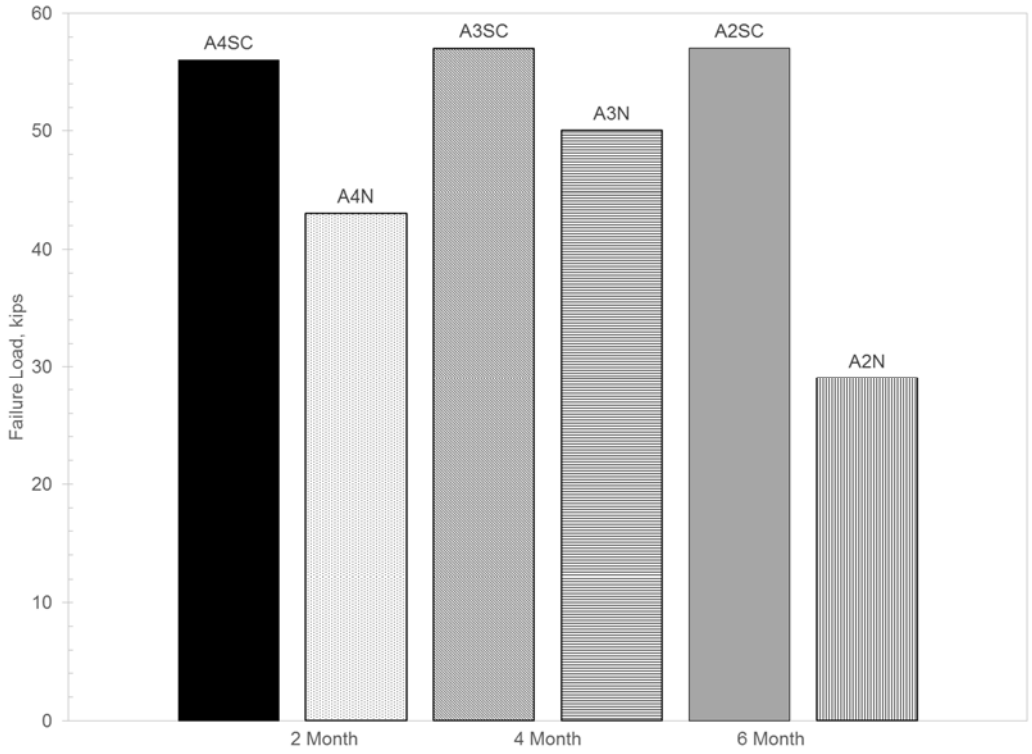

Figure 8-52: Comparison of failure loads for Girder A design

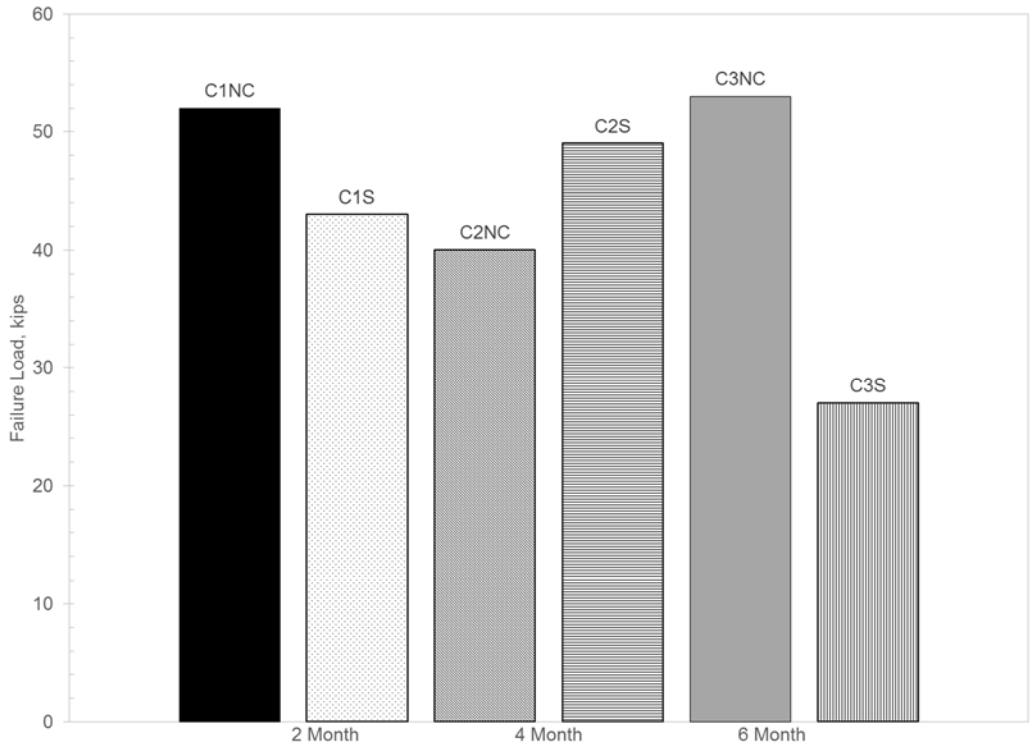

Figure 8-53: Failure loads for Girder C design

Figure 8-54 illustrates the comparison of the applied load at 0.01 in slip and at the initiation of cracking of the girder for the end tested. During the testing of one end, the other end of the girder had zero slip for the six tests where slip was measured on both ends. Also, there were three tests that had unreliable data due to the LVDTs being clamped to the support instead of the web of the beam and/or insufficient contact with the strands due to the irregular surface of the corroded ends. Of note, specimens C3S and A2N both decreased in loading after cracking and then slip occurred at the decreased loading (i.e., cracking occurred before slip). Data from the girders that had unreliable slip data are not presented in Figure 8-54.

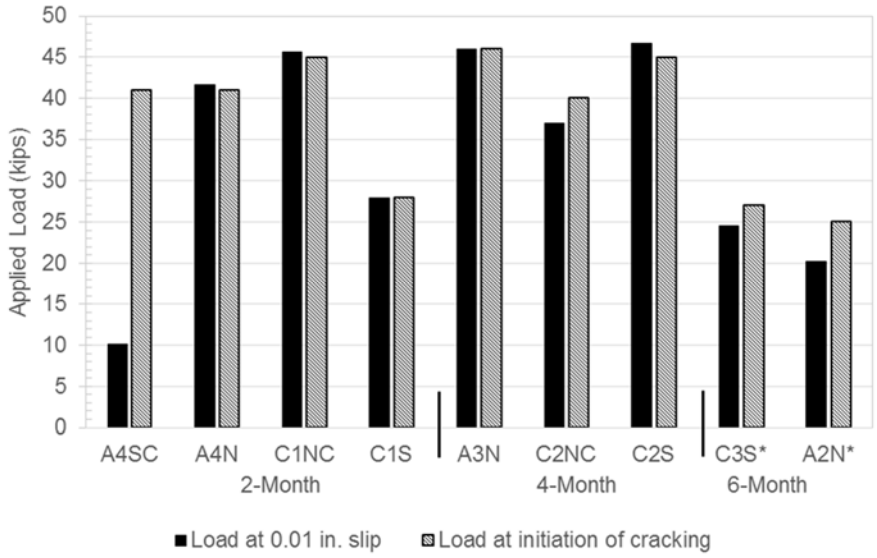

Figure 8-54: Comparison of load at 0.01 in. slip and initiation of cracking (*Note: C3S and A2N decreased in loading after cracking and then slip occurred at that decreased load)

9. FIELD INSPECTION RESULTS

9.1. DATA ANALYSIS

9.1.1. Structural Evaluation

The FHWA uses appraisal ratings to “evaluate a bridge in relation to the level of service which it provides on the highway system of which it is a part” [48]. The structural evaluation rating compares the existing bridge to a bridge that would be built to current standards. Table 9-1 discusses the description for each rating used, and Figure 9-1 illustrates the structural evaluation ratings of bridges under the criteria used for inspection and all of the prestressed concrete girder bridges in Oklahoma built between 1960 and 1979.

Of the 577 bridges built between 1960 and 1979, 94% of the bridges have ratings better than the minimum criteria, with some equal to the present desirable criteria. Of the remaining, there were 29 bridges that met the minimum tolerable limits, and 8 bridges that were considered intolerable: six requiring corrective action and two requiring replacement.

Table 9-1: FHWA structural evaluation criteria [48]

Code	Description
9	Superior to present desirable criteria
8	Equal to present desirable criteria
7	Better than present minimum criteria
6	Equal to present minimum criteria
5	Somewhat better than minimum adequacy to tolerate being left in place as is
4	Meets minimum tolerable limits to be left in place as is
3	Basically intolerable requiring high priority of corrective action
2	Basically intolerable requiring high priority of replacement
1	This value of rating code not used
0	Bridge closed

Figure 9-1: Oklahoma prestressed concrete girder bridges built between 1960 and 1979 and meeting inspection criteria by structural evaluation

9.1.2. Superstructure Condition

According to FHWA's Recording and Coding Guide for the Structure Inventory and Appraisal of the Nation's Bridges, condition ratings are used to describe existing bridges in relation to the original, as-built condition [48]. The guide states the following in respect to condition ratings:

> *"Condition codes are properly used when they provide an overall characterization of the general condition of the entire component being rated. Conversely, they are improperly used if they attempt to describe localized or nominally occurring instances of deterioration or disrepair.*

Correct assignment of a condition code must, therefore, consider both the severity of the deterioration or disrepair and the extent to which it is widespread throughout the component being rated."

The following is stated regarding superstructure condition ratings:

"This item describes the physical condition of all structural members… The structural members should be inspected for signs of distress which may include cracking, deterioration, section loss, and malfunction and misalignment of bearings. The condition of bearings, joints, paint system, etc. shall not be included in this rating, except in extreme situations, but should be noted on the inspection form." [48]

Table 9-2 provides the description for each rating used, and Figure 9-2 illustrates the superstructure condition ratings of bridges under the criteria used for inspection and for all of the prestressed concrete girder bridges built between 1960 and 1979. Additional information on the superstructure condition ratings is included in Appendix D.

Table 9-2: Superstructure condition ratings [48]

Code	Description
9	Excellent Condition
8	Very Good Condition
7	Good Condition
6	Satisfactory Condition
5	Fair Condition
4	Poor Condition
3	Serious Condition
2	Critical Condition
1	"Imminent" Failure Condition
0	Failed Condition

Of the 577 bridges built between 1960 and 1979, almost 99% of the bridges have superstructure ratings equal to or better than fair condition. There were five bridges rated in poor condition (rating of 4), and two bridges in serious condition (rating of 3).

9.1.3. Ownership and Superstructure Ratings

The vast majority of the prestressed concrete girder bridges, constructed in 1960-1979, are under the ownership and maintenance responsibilities of either ODOT or the Oklahoma Turnpike Authority (OTA). The two agencies serve as the agencies

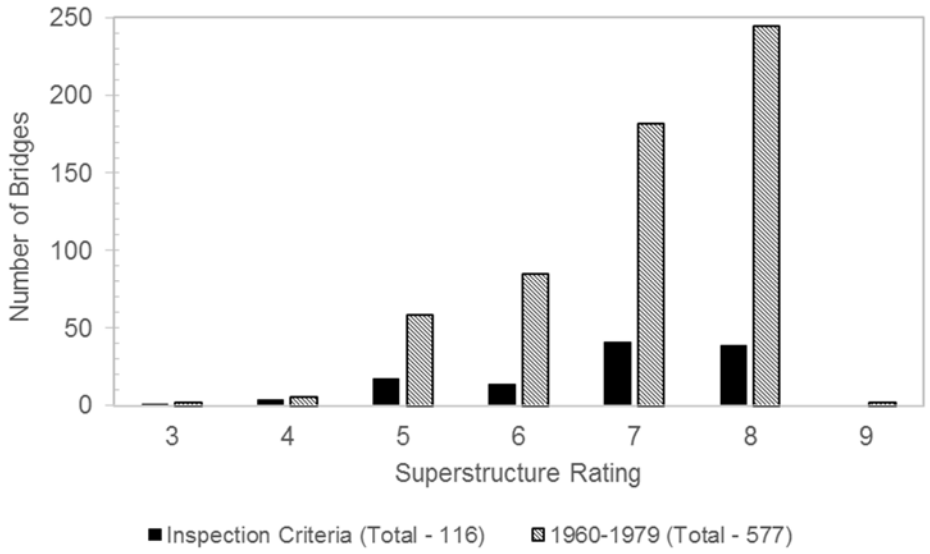

Figure 9-2: Oklahoma prestressed concrete girder bridges built between 1960 and 1979 and meeting inspection criteria by superstructure rating

responsible for intrastate travel within Oklahoma. ODOT is broken into eight field divisions that have maintenance and construction responsibilities in the respective jurisdictions. ODOT maintains the majority of the highway system, and OTA maintains the Oklahoma turnpike system. Figure 9-3 illustrates prestressed concrete girder bridges built between 1960 and 1979 by superstructure rating and ownership. During this timeframe, ODOT built 287 bridges while OTA built 164 bridges.

Almost all of the applicable OTA bridges were rated in either good or very good condition. The ODOT bridges had more reasonable variability given the age of the bridges where many were considered good or very good, but also more reasonably rated as fair or satisfactory condition. Figure 9-4 illustrates the breakdown of ownership for applicable bridges built between 1960 and 1979. While having higher superstructure ratings, the OTA bridges were generally older than the ODOT bridges. Further research should consider the maintenance per bridge spent at OTA vs. ODOT, as a possible indicator to the varied success; or differences in inspection opinion.

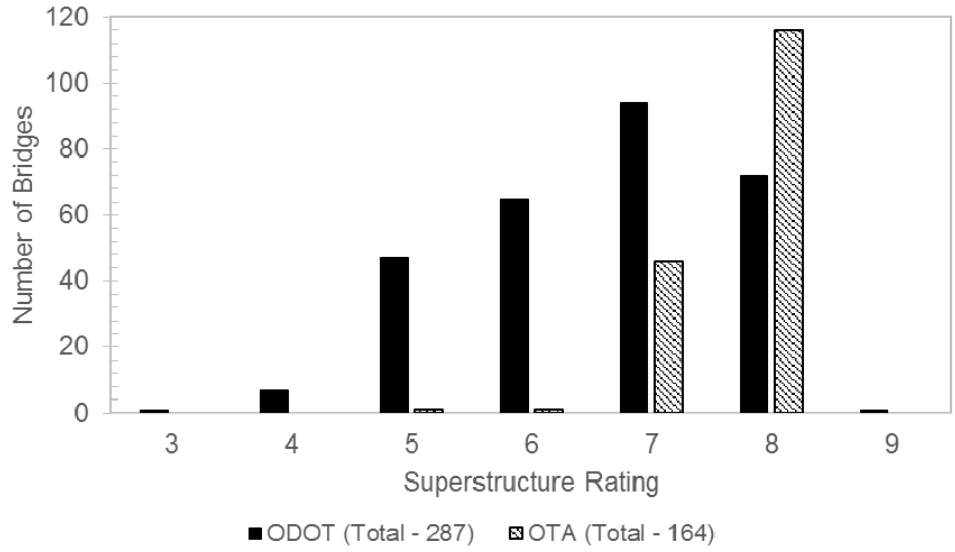

Figure 9-3: Oklahoma prestressed concrete girder bridges built between 1960 and 1979 by superstructure rating and ownership

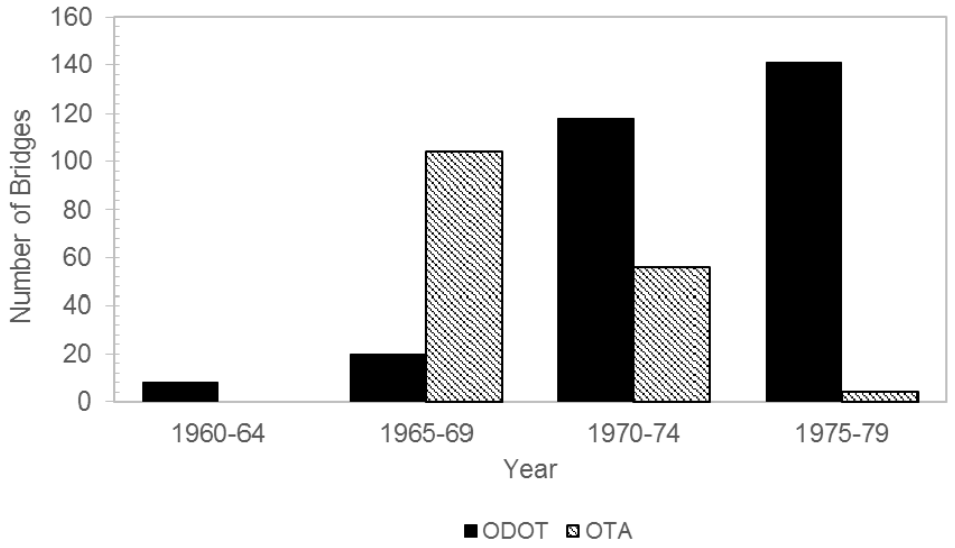

Figure 9-4: Oklahoma prestressed concrete girder bridges built in five year increments between 1960 and 1979 by ownership

9.1.4. Field Divisions and Superstructure Ratings

As mentioned previously, ODOT is broken into eight field divisions that have maintenance and construction responsibilities within their respective jurisdictions. For the 1960 – 1979 timeframe, as Figure 9-5 shows, most of the prestressed concrete bridges in

Field Divisions 1, 2, 4, and 7 were considered in good or very good condition. Field Division 8 had a reasonable distribution between poor and very good condition. Field Divisions 1, 2, 4 and 7 had sharp drops in bridges that were considered to be in fair condition or less. Funding and maintenance, or potentially differences in inspections, could play a part in why there were greater proportions of the bridges in favorable conditions in those regions. Interestingly, OTA accounted for the majority of the bridges constructed in 1960 – 1979 in Field Divisions 1 and 2, and approximately 50/50 with ODOT in Field Division 4.

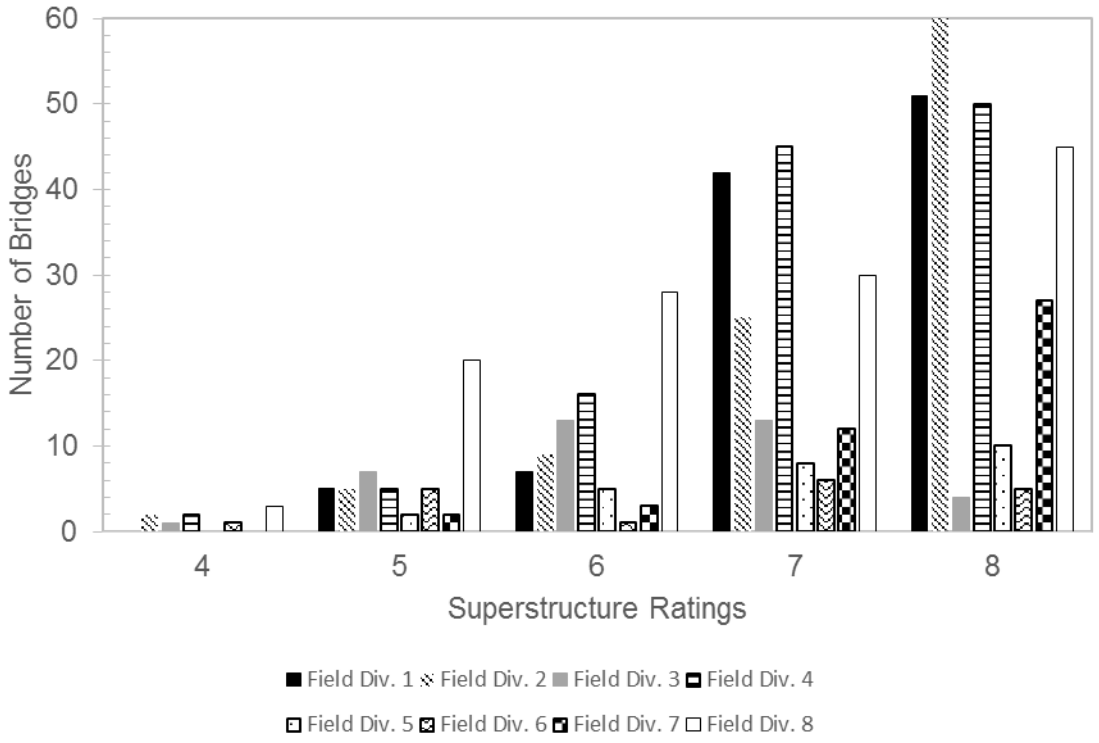

Figure 9-5: Oklahoma prestressed concrete girder bridges built between 1960 and 1979 by superstructure rating and field division

9.2. VISUAL INSPECTION

A total of 19 bridges were inspected through five site inspections to serve as a reasonably representative survey of the prestressed concrete girder bridges constructed from 1960 to 1979 in Oklahoma. The five site visits took place in five different ODOT Field Divisions. A more thorough discussion of each bridge visit can be found in Appendix D.

During the inspections, several common deterioration characteristics were found at multiple sites. The following sections summarize these characteristics and hypothesize their origins.

9.2.1. Corroded Bearing Plates

Many of the bridges inspected had corroded bearing plates; the corrosion, however, ranged from an initial stage with light rust to heavily corroded with expansion of the steel. Heavily corroded bearing plates had a “flaky” appearance to them – likely providing limited structural support. The steel in the bearing plate had corroded to the point where a few layers were held together in the center, but no cohesion was provided at the edge. Figure 9-6 shows an example of a corroded bearing plate. The bearing plates rested directly on the concrete abutment of each bridge. The location of the bearing plates also coincide with the end of the beams, which allow for potential drainage from the deck to fall and pool near the bearing plates. The bearing plates are also exposed to the elements and could be impacted by eroded materials introduced by wind or liquid flow. The bearing plates were aesthetically the most distressing of the features inspected.

Figure 9-6: Example of corroded bearing plate

9.2.2. Corroded Anchor Bolts and Nuts

The anchor bolts and nuts for many of the bridges were also corroded. Corroded anchor bolts were frequently found anchoring corroded bearing plates. In many cases the

anchor bolts were sheared completely in two, and much like the bearing plates, hypothetically could not provide much structural support due to the level of corrosion and deterioration of the components. The anchor bolts may also have been subjected to ponding of water and other liquids, as well as the effects of being exposed to the elements. Figure 9-7 shows an example of a corroded anchor bolt.

Figure 9-7: Example of corroded anchor bolt

In one observed case, deteriorated and necking members were coated to prevent further corrosion and damage (Figure 9-8). The significance and effect of coating the anchor bolts and nuts that had already suffered severe deterioration without replacing them was not immediately apparent.

Figure 9-8: Example of coated, damaged anchor bolt and nut

9.2.3. Spalling above Support

The corroded bearing plates were almost always accompanied by spalling of the concrete on the bottom of the girder directly above the bearing plate. The observed spalling correlated with the degree of corrosion exhibited on the bearing plates. The rusting coloration associated with corrosion could be found on much of the concrete that came in contact with the corroded bearing plates. Figure 9-9 shows an example of spalling above the bearing support.

Figure 9-9: Example of spalling above bearing support

In many cases, the spalling also resulted in cracks emanating from the deteriorating area and extending either horizontally or at an angle upward from the bearing plate. Figure 9-10 shows an example of cracking originating at spalling above a bearing support.

9.2.4. Exposed Reinforcing Steel and Prestressing Strands

Severe deterioration of concrete typically leaves the embedded materials exposed to the elements. This exposure provides an opportunity for further corrosion of the embedded steel, and further deterioration of the concrete structure. Exposed steel that begins to corrode, such as shown in Figure 9-11, likely does not have adequate bonding to provide any actual strength to the member near the exposed section. Figure 9-12 shows an example of exposed prestressing strands.

Figure 9-10: Example of crack from damage around the bearing plate

Figure 9-11: Example of exposed reinforcing steel

Figure 9-12: Example of exposed prestressing strands

9.2.5. Diagonal Crack at Back Corner of Girder

At the back corner of many of the prestressed girders visited, there was a diagonal crack that often resulted in a considerable amount of concrete missing from this area. This commonly noted deterioration characteristic is not immediately explainable like many of the previous characteristics. The common “back diagonal crack” typically led to insufficient concrete cover at the end of the member, thereby exposing the embedded steel materials to extreme environments. For most bridges where this characteristic was observed, many of the aforementioned deterioration characteristics were also present: corroding bearing plates, anchor bolts, and nuts; spalling above the support; and exposed steel. The “back diagonal crack” characteristic typically was similar to the example shown in Figure 9-13.

Figure 9-13: Example of back diagonal cracking

9.2.6. Vertical Cracking along Girder and Diaphragm Interface

Many of the prestressed girders were connected to a diaphragm that spanned multiple girders at the ends of the spans. In many cases, there was a vertical separation (cracking) between the diaphragm and girder, as shown in Figure 9-14. The separation could likely be attributed to the cold joint created during the construction process where the elements were formed separately and cast at different times. Opposing movements of the two structural elements may also have occurred due to temperature, shrinkage, and

Figure 9-14: Example of vertical cracking along diaphragm and girder

creep effects causing cracking in that location. A crack at this location could potentially allow water and chlorides to penetrate to the prestressing strand ends.

9.2.7. Horizontal Cracking along Top Flange and Web Interface

Horizontal cracking was observed along the interface of the top flange and web for multiple bridges, as shown in Figure 9-15. The horizontal cracking may have occurred due to differential movement caused by shrinkage or high stresses resulting from the eccentric prestress force or release forces. The exact cause was not explicitly apparent.

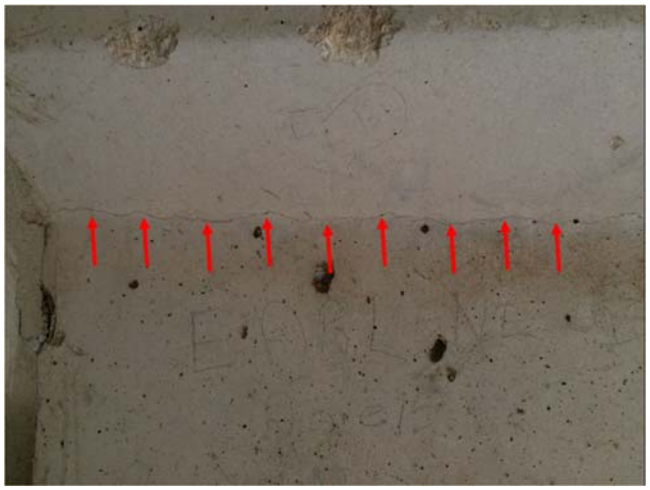

Figure 9-15: Example of horizontal cracking along the top flange and web interface

9.2.8. Diagonal Cracking from the Top Flange and Web Interface

Another frequently noted deterioration characteristic was diagonal cracking that emanated from the top flange and web interface and extended downward and into the span, shown in Figure 9-16. The cause of the diagonal cracking was not immediately apparent, but may be related to stresses caused by the eccentric prestress. The cracks were generally small in width and had varying lengths.

Figure 9-16: Example of diagonal cracking from the top flange and web interface

9.2.9. Diaphragm Deterioration

While not necessarily pertinent to the structural health of the prestressed girders, it is worth mentioning that many of the end diaphragms connecting the individual girders were in a deteriorated state. Many seemed to have insufficient concrete cover, leading to exposed rebar, and initiation of corrosion, as shown in Figure 9-17.

Overall, the girders subjected to the accelerated corrosion process did not exhibit many of the common factors noticed in girders visited in the field. Those corroded ends exhibited the common rusting discoloration, as well as the initiation of corrosion impacting the prestressing strands. In general, the deterioration in the field was frequent, and visually seemed much worse than what was possible with the laboratory specimens.

Figure 9-17: Example of diaphragm deterioration

10. CONCLUSIONS AND RECOMMENDATIONS

10.1. SUMMARY OF MAIN FINDINGS FOR STEEL BRIDGES

A localized retrofit using pre-stressed CFRP material was developed to increase the fatigue capacity of common details within aged steel bridges. In this study, four stringer/multi-girder steel bridges with varying construction types were analyzed using finite element analysis. Critical fatigue details within each bridge were identified, and the fatigue performance was evaluated using the modified Goodman constant life diagrams. Finally, analytical formulations based on the Goodman diagrams were developed to determine the pre-stress force required to shift the stresses in critical details from a state of finite fatigue life to a state of infinite fatigue life. In addition to this analytical investigation, two experimental tests are conducted in which 1) a local bridge is instrumented with strain gauges and analyzed using finite element modeling; real-time strain measurements were compared with results of the finite element simulation during the passage of a truck along the bridge span, and 2) the function and performance of the developed retrofit was evaluated on a diaphragm to girder weld detail. The following conclusions were determined from the analytical and experimental results:

1. Finite element modeling using four-node linear shell elements provides a reasonable estimation of the actual strain measurements in an instrumented steel bridge. Results of the finite element analysis overestimated strain values by about 20-40 μin./in.; however, the concrete bridge deck was excluded from

the finite element model. Analytical results from the finite element analysis are conservative based on the modeling techniques used.

2. The Goodman fatigue evaluation showed that skewed bridge construction is more damaging to the steel cross-frame-to-girder component fatigue life than non-skewed construction. Cross-frame and diaphragm details within the skewed bridge geometry were susceptible to higher stress ranges during the passage of the fatigue truck due to distortion in the web of the longitudinal girder.
3. Using the Goodman criterion, the pre-stress force required to shift a structural detail from a state of finite fatigue life to infinite fatigue life increases linearly with the applied stress range; however, the magnitude of the pre-stressing force is dependent on the size of the steel member cross-section.
4. Laboratory tests were successful in shifting the mean stress in an instrumented steel beam using the localized retrofit having pre-stressed CFRP plates. Although this experiment only provides a preliminary evaluation of the retrofit performance, the results indicate that the retrofit is capable of reducing the mean stress of structural details therein improving fatigue performance.
5. Preparation of the steel surface (grinding away of corrosion) is needed prior to retrofit application, as the corroded surface layer is prone to de-bonding during retrofit pre-stress.
6. Retrofit pre-stress losses of near 10% within 48-hours could be expected for the configuration tested; however, alternative configurations using CFRP rods may help reduce these pre-stress losses.

10.2. SUMMARY OF MAIN FINDINGS FOR CONCRETE BRIDGES

Over the course of this research, nine approximately half-scale AASHTO Type II girders were designed, constructed, and exposed to varying levels of a corrosive environment through a corrosion accelerant process. The varying levels of exposure to the end zone of the girders replicated the various environmental conditions a bridge girder could be exposed to in the field. The girders were designed with two different reinforcement configurations (Girder A and Girder C design) to create similar stress states to a recently decommissioned prestressed concrete girder bridge in Oklahoma

built within during the period of 1960 to 1979. Two girders from this decommissioned bridge were tested as part of a related project. Six of the half-scale girders were shear tested to examine what, if any effect the end zone deterioration has on the shear capacity of the girder. The remaining three half-scale girders that were exposed to the various environmental conditions will form the basis of additional research discussed later in this section. Of the six shear tests on the corroded end of the girders, four resulted in slip of the prestressing strands prior to the initial crack of the beam. For the control end of the girders, all six shear tests (both Girder A and Girder C designs) illustrated cracking of the girder prior to the initiation of slip. The control end of the girders cracking prior to slip shows that bond performance was not the same for the control and corroded ends. The two most common failure mechanisms were: bond-shear failure (either cracking before slip or slip before cracking) and bond-shear/flexure failure where cracking occurred before slip and crushing of the concrete in the top flange was observed.

Shear tests resulted in measured shear values less than the design shear capacity for each girder in all cases (i.e., corroded and control end) when compared to the ACI [50] and AASHTO LRFD 2007 [51] methods. The designed shear capacities were calculated using actual girder dimensions and measured compressive strengths. The a/d ratio of 2.0 used for the shear tests is near the limiting value for the methods given by the codes, which may have reduced the applicability of the code equations. All of the girder ends that had been exposed to the corrosive environment had a larger measured shear than the control end, except for one girder specimen (C2). Similar results were shown by Abosrra et al. [29] for minor corrosion. The percent difference between the measured and design shear values ranged from 21% to 32% below the expected values for the corroded ends not including girder specimen C2, which was 58% below expectation. For the control end, the percent difference in measured and design shear values had a much larger range – from 35% to 91% below expectation. These results may be due to several issues. The corroded ends may have sustained a larger load because the moisture from the accelerated corrosion process actually helped the girders cure longer. With the exception of girder specimen C2, the corroded end of the girders were tested first. The order of testing could have potentially impacted the condition of the beam and had an impact on the remaining end – resulting in less resistance available. While the measured

compressive strengths were used to calculate the shear capacities, variation in the measured strengths could have caused transfer lengths greater than estimated during calculation of shear capacity.

Overall, the corroded ends of the girders with the Girder A design, sustained a larger failure load than those corroded ends of the girders with the Girder C design. Based on the results, the larger prestressing strands used for the Girder C design could have been more susceptible to bond failure, causing the beam to fail sooner than the smaller prestressing strands used in the Girder A design. Larger diameters of reinforcement and prestressing strands require larger anchorage lengths per the ACI [50] and AASHTO LRFD codes [51], which supports this possibility. Further research would be necessary to prove if this indeed was the reason.

Concurrently with the lab experiments, a total of 19 bridges were inspected through five site inspections to serve as a survey of the prestressed concrete girder bridges constructed from 1960 to 1979 in Oklahoma. The five site visits took place in five different Oklahoma Department of Transportation (ODOT) Field Divisions. During the inspections, various deterioration characteristics were found at multiple sites. Those deterioration characteristics include: corroded bearing plates; corroded anchor bolts and nuts; spalling above the support; exposed rebar and prestressing strands; diagonal cracking of the back corner of the girder; vertical cracking along the girder and diaphragm interface; diagonal cracking originating from the top flange and web interface; and diaphragm deterioration. In reviewing the National Bridge Inventory [54] data, there was variation in superstructure condition ratings between bridges owned by ODOT and those owned by the Oklahoma Turnpike Authority. It was not immediately clear if this variation was a result of deferred maintenance and lack of funding, or differences in inspector opinions among the entities.

Together, the observations from the field inspections and the lab experiments were used to analyze existing retrofit methods and determine recommendations for in-situ rehabilitation for varying levels of deterioration. Fiber reinforced polymer, such as carbon fiber reinforced polymer systems (e.g., sheets, U-wraps, and strips) were identified as a viable option for increasing strength of girders damaged in the field. Available literature reviewed showed improved strength (flexural and shear) for repaired

members in comparison to those unrepaired and improved protection against further deterioration.

While the research effort described in this report has been largely inclusive in the data sought and presented, the results are expected to be similar only to the work performed during this analysis. Any differences in girder designs, concrete mix, bridge configurations, etc. could cause a variation from the results presented in this report.

The following specific conclusions can be drawn from the results obtained during the research discussed in this report:

1. The corroded ends of the members exhibited larger measured shear strengths for the conditions tested. The exact significance of these results is unclear, and further research including additional deterioration levels is necessary.
2. The difference in measured and design shear strengths could be attributed to: the variation in compressive strengths; an *a*/*d* ratio near the limit for the methods used; and potential variations in transfer length related to compressive strength.
3. All of the shear failures included the effects of strand slip and the tests of corroded ends indicated that strand slip occurred prior to cracking, while the tests of the control ends indicated cracking occurred prior to strand slip. This result indicates that corrosion may affect bond of the prestressing steel to concrete.
4. Common deterioration characteristics were observed at various bridges across the State of Oklahoma but did not appear to correlate directly with the superstructure ratings.

10.3. INTEGRATION OF CONCLUSIONS AND RECOMMENDATIONS

The research presented in this report addressed problem areas for corrosion and fatigue in the two most common type of bridge structure in region 6. The localized retrofits described in this report have the potential to extend the life of in-service steel bridges subject to damage from fatigue at cross-frame details and are almost instantly implementable. However, additional research is warranted to identify methods for reducing prestress losses in the retrofit and in surface preparation for mounting. A number of common deterioration characteristics were noted for prestressed concrete

girder ends for in-service bridges in Oklahoma. Several potential steps could be implemented to reduce the impacts of this deterioration. These include ensuring proper functioning of expansion joints to prevent exposure of the girder ends to deleterious materials and coating bearing plates, anchor bolts, and nuts. Further investigation of the reasons why the prestressed girder specimens exposed to corrosive environments performed better than the non-corroded ends is needed. A larger number of specimens and more heavily corroded members should be tested to better understand the effects of corrosion on shear capacity as large-scale tests of the girders taken from the I-244 bridge performed as part of a related project indicated an effect of corrosion on failure mechanism. The girders that have begun the deterioration process would benefit from repair to the member, such as patching, coupled with the use of a fiber reinforced polymer to increase the shear strength near the girder end if necessary.

REFERENCES

[1] A. Svirsky, "National Bridge Inventory (NBI) Database.," 2015. [Online]. Available: http://nationalbridges.com/.

[2] D. Mertz, "Design for Fatigue," *Steel Bridge Design Handbook,* pp. FHWA-IF-12-052-Vol. 12, 2012.

[3] D. Mertz, "Design for Fatigue," *Steel Bridge Design Handbook,* vol. 12, no. FHWA-IF-12-052, 2012.

[4] American Association of State Highway and Transportation Officials (AASHTO), "AASHTO LRFD Bridge Design Specifications," *AASHTO,* p. 2nd Edition, 1998.

[5] R. P. Gangloff, "Environmental Cracking— Corrosion Fatigue," in *Corrosion Tests and Standards*, ASTM- MNL20-2nd Edition-Chap. 26., 2005.

[6] R. J. Dexter and J. M. Ocel, "Manual for Repair and Retrofit of Fatigue Cracking in Steel Bridges," FHWA-IF-13-020, Federal Highway Administration, Washington, D.C., 2013.

[7] D. Kopeliovich, "Carbon Fiber Reinforced Polymer Composites," 2012. [Online]. Available: http://www.substech.com/dokuwiki/doku.php?id=carbon_fiber_reinforced_polymer_composites.

[8] J. G. Teng, J. F. Chen, S. T. Smith and L. Lam, "FRP strengthened RC structures," Chichester, UK, 2002.

[9] A. Peiris and I. Harik, "Steel Bridge Girder Strengthening Using Postinstalled Shear Connectors and UHM CFRP Laminates," *ASCE. J.Perform. Constr. Facil.,* vol. 29, no. 5, p. 04014139., 2015.

[10] D. Schnerch and a. Rizkalla, "Flexural Strengthening of Steel Bridges with High Modulus CFRP Strips," *ASCE. Journal of Bridge Engineering,* vol. 13, no. 2, pp. 192-201, 2008.

[11] T. C. Miller, M. J. Chajes, D. R. Mertz and J. N. Hastings, "Strengthening of a Steel Bridge Girder using CFRP Plates," *Journal of Bridge Engineering,* pp. Vol. 6-No. 6: 514-522, 2001.

[12] B. Kaan, F. Alemdar, C. Bennett, A. Matamoros, R. Barrett-Gonzalez and S. Rolfe, "Fatigue Enhancement of Welded Details in Steel Bridges Using CFRP Overlay

Elements," *ASCE Journal of Composites for Construction,* vol. 16, no. 2, pp. 138-149, 2012.

[13] Y. Huawen, C. Konig, T. Ummenhofer, Q. Shizhong and R. Plum, "Fatigue Performance of Tension Steel Plates Strengthened with Prestressed CFRP Laminates.," *ASCE Journal of Composites for Constuction,* vol. 14, no. 5, pp. 609-615, 2010.

[14] E. Ghafoori, M. Motavalli, A. Nussbaumer, A. Herwig, G. Prinz and M. Fontana, "Design criterion for fatigue strengthening of riveted beams in a 120-year-old railway metallic bridge using pre-stressed CFRP plates," *Elsevier,* vol. 68, no. 1-13, p. Composites: Part B , 2015.

[15] J. Fasl, C. J. Larosche and J. Fraczek, "Ductility Behavior of Corroded Bars in Concrete Slabs," *Concrete International,* pp. 55-61, 1 April 2016.

[16] K. Basham, "Delve Into Two Theories Related to Cracks and Rebar Corrosion," *Concrete Contractor,* 16 March 2015.

[17] F. B. Coggins and C. W. French, "Chloride Ion Distribution in Twenty-Year-Old Prestressed Bridge Girders," *ACI Materials Journal,* vol. 87, no. 5, pp. 479-488, September - October 1990.

[18] G. K. Chou and K. C. Hover, "Cathodic Protection for Prestressed Structures," *Concrete International,* pp. 26-30, January 1987.

[19] S. M. Bruce, P. S. McCarten, S. A. Freitag and L. M. Hasson, "Deteoriation of Prestressed Concrete Bridge Beams," Land Transport New Zealand Research Report 337, 2008.

[20] R. Szilard, "Corrosion and Corrosion Protection of Tendons in Prestressed Concrete Bridges," *ACI Journal,* pp. 42-59, January 1969.

[21] K. Vu, M. G. Stewart and J. Mullard, "Corrosion-Induced Cracking: Experimental Data and Predictive Models," *ACI Structural Journal,* vol. 102, no. 5, pp. 719-726, September-October 2005.

[22] A. Mukherjee and G. L. Rai, "Performance of Reinforced Concrete Beams Externally Prestressed with Fiber Composites," *Construction and Building Materials,* vol. 23, no. 2, pp. 822-828, 2009.

[23] G. Song and A. Shayan, "Corrosion of steel in concrete: causes, detection and prediction: a state-of-the-art review," ARRB Transport Research Ltd. Review Report 4, 1998.

[24] V. Novokshchenov, "Condition Survey of Prestressed Concrete Bridges," *Concrete International,* pp. 60-68, September 1989.

[25] J. L. Smith and Y. P. Virmani, "Materials and Methods for Corrosion Control of Reinforced and Prestressed Concrete Structures in New Construction (FHWA-RD-00-081)," U.S. Department of Transportation, Federal Highway Administration, McLean, 2000.

[26] R. A. Rogers, L. Wotherspoon, A. Scott and J. M. Ingham, "Residual strength assessment and destructive testing of decommissioned concrete bridge beams with corroded pretensioned reinforcement," *PCI Journal,* vol. 57, no. 3, pp. 100-118, 2012.

[27] M. K. ElBatanouny, J. Mangual, P. H. Ziehl and F. Matta, "Early Corrosion Detection in Prestressed Concrete Girders Using Acoustic Emission," *Journal of Materials in Civil Engineering,* vol. 26, no. 3, pp. 504-511, 1 March 2014.

[28] T. M. Pape and R. E. Melchers, "Performance of 45-year-old corrdoed prestressed concrete beams," *Structures and Buildings,* vol. 166, no. SB10, pp. 547-559, November 2013.

[29] C. S. Cai and X. Miao, "Repairing/Strengthening of Bridges with Post-tensioned FRP materials and Performance Evaluation," Louisiana Transportation Research Center, 2015.

[30] I. Abosrra, A. F. Ashour and M. Youseffi, "Corrosion of Steel Reinforcement in Concrete of Differenct Compressive Strengths," *Construction and Building Materials,* 23 May 2011.

[31] B. D. Merrill, S. Keske and J. McGormley, "Girder Anchorage Zone Crack Investigation - Interim (Phase 1) Report," Oklahoma Department of Transportation, Oklahoma City, 2015.

[32] Transportation Research Board, "TRID Database," 2016. [Online]. Available: https://trid.trb.org/view.aspx?id=1329302.

[33] A. A. Almusallam, "Effect of degree of corrosion on the properties of reinforcing steel bars," *Construction and Building Materials,* pp. 361-368, 5 January 2001.

[34] M. K. Tadros, S. S. Badie and C. Y. Tuan, "NCHRP Report 654 Evaluation and Repair Procedures for Precast/Prestressed Concrete Girders with Longitudinal Cracking in the Web," Transportation Research Board, Washington, D.C., 2010.

[35] M. D. Pritzl, H. Tabatabai and A. Ghorbanpoor, "Laboratory Evaluation of Select Methods of Corrosion Prevention in Reinforced Concrete Bridges," *International*

Journal of Concrete Structures and Materials, vol. 8, no. 3, pp. 201-212, September 2014.

[36] D. Darwin , J. Browning, T. Van Nguyen and C. Locke, Jr. , "Mechanical and Corrosion Properties of a High-Strength, High Chromium Reinforcing Steel for Concrete," 2002.

[37] International Federation for Structural Concrete, "Design and Use of Externally Bonded Fibre Reinforced Polymer Reinforcement (FRP EBR) for Reinforced Concrete Structures," International Federation for Structural Concrete, Lausanne, 2001.

[38] A. ElSafty, "Getting Clearance: CFRP U-wrapping shows promise as a repair option," *Roads & Bridges,* pp. 22-27, April 2013.

[39] C. Higgins, G. Williams, M. Mitchell, M. Dawson and D. Howell, "Shear Strength of Reinforced Concrete Girders with Carbon Fiber-Reinforced polymer: Experimental Results," *ACI Structural Journal,* vol. 109, no. 6, pp. 805-814, November-December 2012.

[40] I. Ray, G. C. Parish, J. F. Davalos and A. Chen, "Effect of Concrete Substrate Repair Methods for Beams Aged by Accelerated Corrosion and Strengthened with CFRP," *Journal of Aerospace Engineering,* vol. 24, no. 2, pp. 227-239, 1 April 2011.

[41] SIMULIA, Abaqus/CAE User's Manual, Providence, RI. : Dassault Systèmes Simulia Corp., 2012.

[42] Google Maps, 2016. [Online]. Available: https://www.google.com/maps.

[43] J. Shigley and C. Mischke, Mechanical engineering design (5th ed,), New York: McGraw-Hill., 1989.

[44] J. Marin, Mechanical Behavior of Engineering Materials, Englewood Cliffs, NJ: Prentice-Hall, 1962.

[45] K. MacDonald, "Fatigue design rules for welded structures," in *Fracture and fatigue of welded joints and structures*, Cambridge, UK, Woodhead Pub., 2011.

[46] B. Cranor, "Analysis and Experimental Testing for Shear Behavior of an AASHTO Type II Girder in Service for Several Decades," 2015.

[47] FHWA, "National Bridge Inventory (NBI)," 9 August 2016. [Online]. Available: https://www.fhwa.dot.gov/bridge/nbi.cfm.

[48] J. Baughn, "Ugly Bridges," 9 August 2016. [Online]. Available: http://uglybridges.com/.

[49] Federal Highway Administration, "Recording and Coding Guide for the Structure Inventory and Appraisal of the Nation's Bridges," Washington, D.C., 1995.

[50] ODOT, "Field Divisions," 9 August 2016. [Online]. Available: https://www.ok.gov/odot/About_ODOT/Contact_ODOT_Divisions/Field_Divisions.html.

[51] AASHTO, LRFD Bridge Design Specifications Customary U.S. Units 4th Edition, Washington, D.C.: American Association of State Highway and Transportation Officials, 2007.

[52] American Association of State Highway and Transportation Officials (AASHTO), AASHTO LFRD Bridge Design Specifications, Washington, D.C.: American Association of State Highway and Transportation Officials (AASHTO), 2012, p. 6th Edition.

[53] ACI Committee 318, Building Code Requirements for Structural Concrete (ACI 318-14) and Commentary (ACI 318R-14), Farmington Hills, Michigan: American Concrete Institute, 2014.

[54] Federal Highway Administration (FHWA), "National Bridge Inventory," 9 August 2016. [Online]. Available: https://www.fhwa.dot.gov/bridge/nbi.cfm.

[55] T. Irvine, "Rainflow Cycle Counting in Fatigue Analysis," 26 August 2011. [Online]. Available: http://citeseerx.ist.psu.edu/viewdoc/download?doi=10.1.1.444.3640&rep=rep1&type=pdf.

[56] National Association of Corrosion Engineers (NACE), "Highways and Bridges," 2012. [Online]. Available: https://www.nace.org/Corrosion-Central/Industries/Highways-and-Bridges/.

[57] T. Dinges, "The History of Prestressed Concrete: 1888 to 1963," Manhattan, 2009.

[58] E. G. Nawy, Prestressed Concrete: A Fundamental Approach, Upper Saddle River, New Jersey: Prentice Hall, 2010.

[59] MIT OpenCourseWare, "Reinforced and Prestressed Concrete," 21 November 2008. [Online]. Available: https://www.flickr.com/photos/mitopencourseware/3048302726/.

[60] American Association of State Highway and Transportation Officials (AASHTO), AASHTO LRFD Bridge Design Specifications 2nd Edition, Washington, D.C.: AASHTO, 1998, p. 2nd Edition.

APPENDIX A.

RAIN-FLOW CYCLE COUNTING

Rain flow cycle counting is a technique used to count fatigue cycles in a stress history. Cycle counting techniques help to simplify complicated stress histories, allowing the application Miner's rule to assess the fatigue damage in a structural component. The rain flow method obtained its name from an analogy of rain dripping down a pagoda roof. The procedure for rain flow counting is described below.

Procedure for rain flow counting [53]:

1. Reduce the time history to a sequence of peaks and troughs.
2. Turn the sheet clockwise 90°, so the starting time is at the top
3. Imagine that the time history is a pagoda with water dripping down each peak and trough
4. Begin at the trough with the lowest value and count the number of half-cycles by looking for terminations in the flow occurring when either:
5. It reaches the end of the time history
6. It merges with a flow that started at an earlier trough; or
7. It encounters a trough of greater magnitude.
8. Repeat step 4 for each peak starting at the peak with the highest value.
9. Pair up half-cycles of identical magnitude (but opposite sense) to count the number of complete cycles.

This procedure is illustrated using the sample stress history shown in Figure A-1(a). Figure A-1(b) shows the labeled peaks and troughs and illustrated the "rain flow" in the stress history.

The total counts and the magnitude of each stress cycle is given in Table A-1, and the resulting cycle counts described in step 4 are as follows:

Counting Half Cycles:

Troughs: A-B, C-H, E-E', G-G'

Peaks: B-C, D-E, F-G, H-I

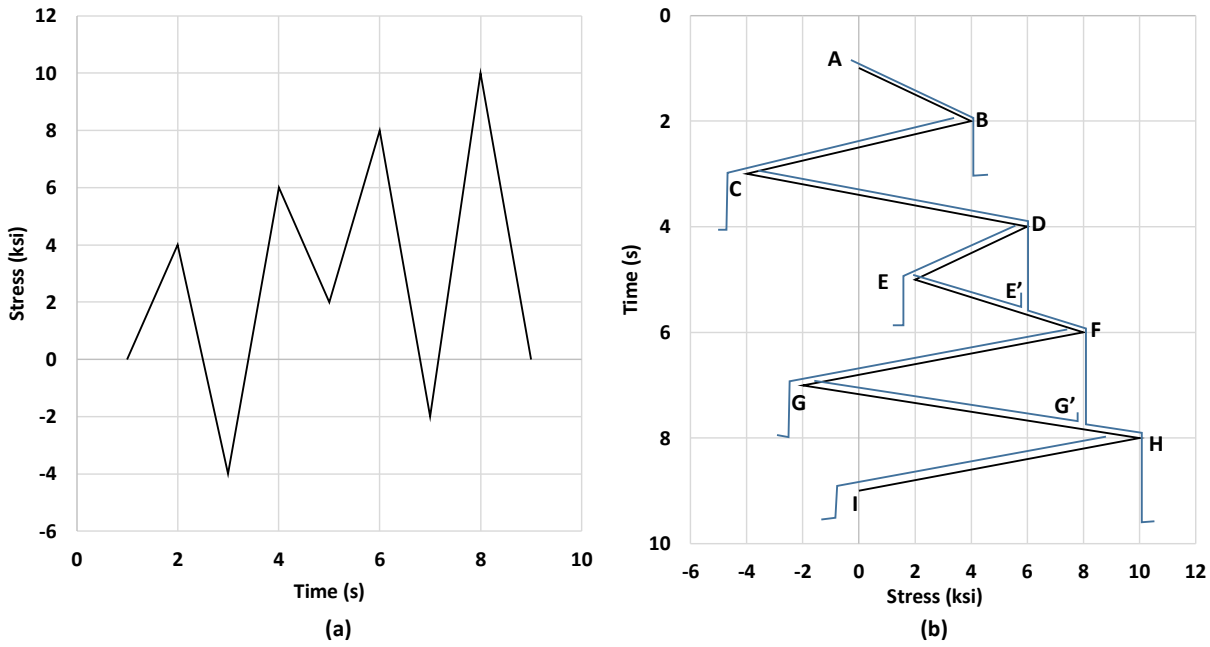

Figure A-1: (a) Sample stress history (b) rain flow cycle counting procedure.

Table A-1: Total cycle counts, stress range, and path for sample stress history

Stress Range (ksi)	Number of Cycles, (n_i)	Path
4	0.5	A-B
14	0.5	C-H
8	0.5	B-C
10	0.5	H-I
4	1.0	D-E-E’
10	1.0	F-G-G’

APPENDIX B.

ENDURANCE LIMIT, S_e

This section describes the procedure for calculating the endurance limit, S_e, using the Marin equation. The process is described in detail in Shigley (1989). The Marin equation was given previously by Equation 3-7 and is shown here as Equation B-1.

$$S_e = k_a k_b k_c k_d k_e k_f S_e' \qquad \text{Equation B-1}$$

S_e' is the endurance limit of the rotating beam specimen given previously by Equation 3-6 and is shown below as Equation B-2

$$S_e' = \begin{cases} .5\, S_{ut} & S_{ut} \le 200ksi \\ 100\ ksi & S_{ut} > 200ksi \end{cases} \qquad \text{Equation B-2}$$

B.1. SURFACE FACTOR k_a

The initiation of fatigue cracks often occurs at the free surface of the material. The surface modification factor is used to assess the quality of the finished surface and the tensile strength of the material. k_a is represented by Equation B-3, where a and b are the two coefficients given in Table B-1.

$$k_a = aS_{ut}^b \qquad \text{Equation B-3}$$

Table B-1: Parameters for Marin surface modification factor

Surface Finish	Factor a, S_{ut} given in ksi	Exponent *b*
Ground	1.43	-0.085
Machined or cold-drawn	2.70	-0.265
Hot-rolled	14.4	-0.718
As-forged	39.9	-0.995

B.2. SIZE FACTOR k_b

The size modification factor for rotation bar specimens were obtained through curve fitting of experimental results. This factor is based on the probability of failure for within a certain volume. As the volume increases, there is a higher probability of stress interaction with a critical flaw; therefore, the endurance limit decreases [43]. For members that are subjected to bending and torsion, k_b is expressed as

$$k_b = \begin{cases} 0.879d^{-0.107} & 0.11 \le d \le 2\ in \\ 0.91d^{-0.157} & 2 < d \le 10\ in \end{cases} \qquad \text{Equation B-4}$$

For axial loading there is no size effect, therefore k_b=1. For members with non-circular cross-sections, an effective diameter d_e is used in place of d in Equation 8-4. For rectangular cross sections, d_e is given by

$$d_e = 0.808\sqrt{bh} \qquad \text{Equation B-5}$$

where *b* and *h* are the base and height of the cross-section, respectively. Equations to calculate d_e for other common structural shapes are given in Shigley (1989).

B.3. LOAD FACTOR k_c

The load modification factor considers whether axial, bending, or torsional loading is applied to a structure. Average values estimated for steel are given below.

$$k_c = \begin{cases} 1.0 & Bending \\ 0.85 & Axial \\ 0.59 & Torsion \end{cases}$$

B.4. TEMPERATURE FACTOR k_d

The ultimate strength (S_{ut}) varies under extreme temperatures. At high operating temperatures, the yield strength of steel is reduced and ductile failure is expected. At low operating temperatures, brittle fracture is expected in steel structures. Due to this reality, the endurance limit is similarly related to the tensile strength at extreme temperatures [42]. The following fourth order polynomial (obtained by curve fitting of experimental results) is used to calculate the temperature modification factor, where T_F is the temperature in degrees Fahrenheit for the range $70 \leq T_F \leq 1000$ °F.

$$k_d = 0.975 + 0.432(10^{-3})T_F - 0.115(10^{-5})T_F{}^2 \qquad \text{Equation B-6}$$
$$+0.104(10^{-8})T_F{}^3 - 0.595(10^{-12})T_F{}^4$$

B.5. RELIABILITY FACTOR k_e

Endurance strength data is often reported as average values. The reliability modification factor accounts for the scatter of experimental data. Reliability factors for some standard specified reliabilities assuming an eight percent standard deviation of the endurance limit are given in Table B-2.

B.6. MISCELLANEOUS-EFFECTS FACTOR k_f

The miscellaneous-effects modification factor accounts for other various effects that the material may be subjected to during service. This factor may consider corrosion, electrolytic plating, metal spraying, cyclic frequency, and frottage corrosion [42]. These

Table B-2: Reliability factors corresponding to 8% standard deviation of the endurance limit

Reliability, %	Reliability Factor k_e
50	1.000
90	0.897
95	0.868
99	0.814
99.9	0.753
99.99	0.702
99.999	0.659
99.9999	0.620

values are not easily attained; therefore, the miscellaneous-effects factor is assumed to be 1.0 in this work.

B.7. CALCULATION OF S_e

The endurance limit, S_e, was calculated for each bridge. Results of this calculation are described here for bridge A-6243. Reasonable assumptions were made for calculations of the modification factors due to limited information about the bridge steel. Using Equation B-3 and assuming a hot rolled finish assumption, the surface modification factor was calculated as k_a=0.719. The critical fatigue region in bride A-6243 was located at the weld between the cross-frame and the girder web; therefore the size factor was calculated considering cross-section of the girder web (0.5in x 48 in). Using Equation B-5 the effective diameter of the web was calculated as d_e=3.958 in. Substituting this value into Equation B-4 results in a size factor of k_b=0.733. Assuming a combination of bending and axial loading, the load factor was approximated as k_c=0.95. Using Equation B-6 and assuming a normal operating temperature of 70°F, the temperature factor was calculated as k_d=1.0. A reliability factor of 95% is considered for the analysis, which results in k_e=0.868. The bridges were constructed using Grade 50 steel with an ultimate strength (S_{ut}) of 65 ksi. Using Equation B-2 endurance limit of the rotating beam specimen was calculated as S_e'=32.5 ksi. Substituting these values into the Marin equation (Equation B-1), results in an endurance limit of S_e=14 ksi. A similar value was calculated for each of the four brides, therefore an endurance limit of S_e=14 ksi is used for all Goodman analyses.

APPENDIX C.

CONCRETE GIRDER DESIGN

C.1. BEAM “A” AND BEAM “C” DRAWINGS

From “Sections Prestressed Concrete Girders FAP 244-2(134)093, Sheet No. 44, Revision #6” drawing provided by ODOT:

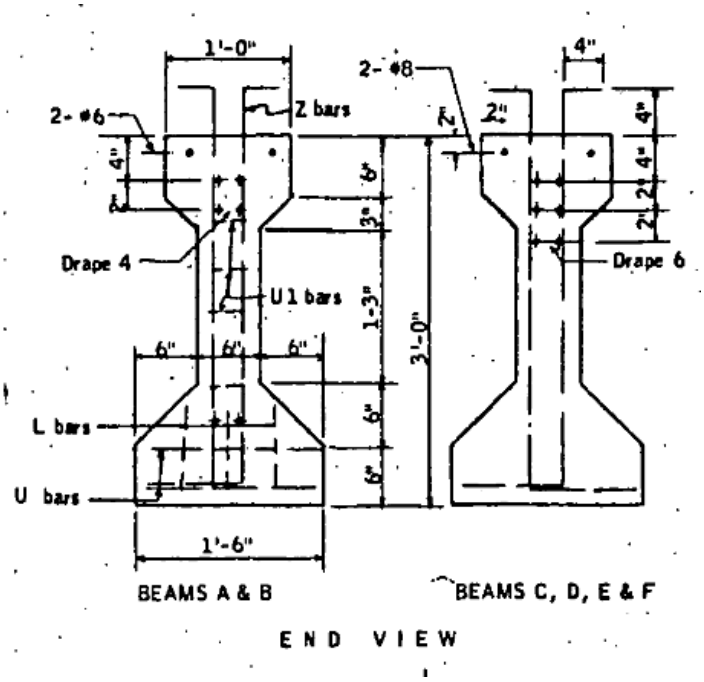

Figure C-1: End cross-section view of Beam "A" and Beam "C"

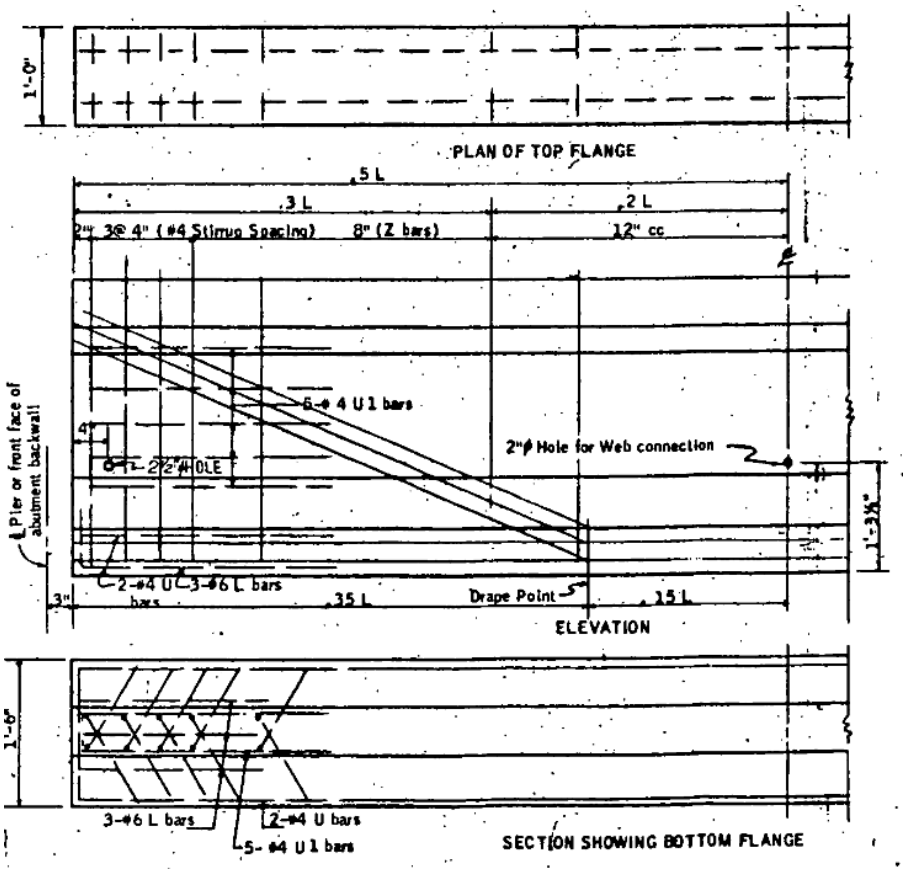

Figure C-2: Elevation and bottom flange plan views of Beam "A" and Beam "C"

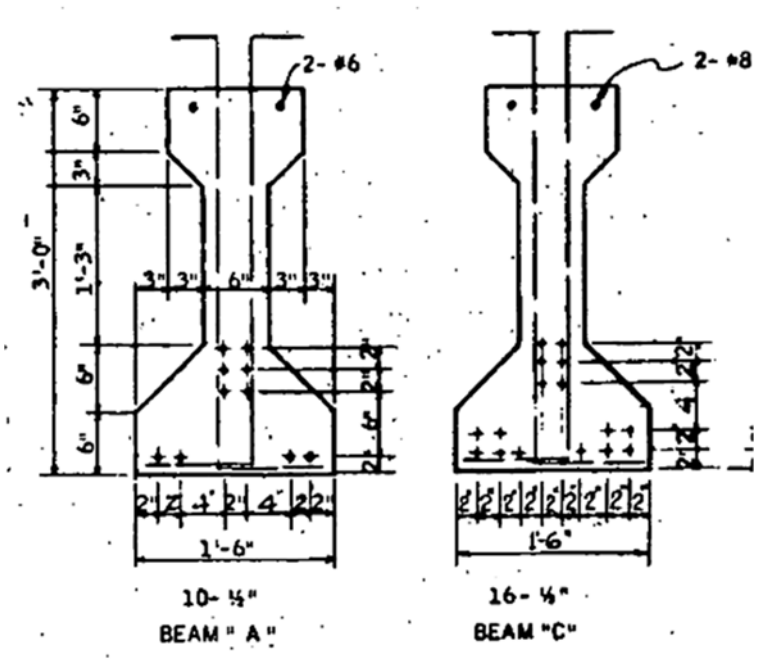

Figure C-3: Midspan cross-section view of Beam "A" and Beam "C"

C.2. GIRDER DESIGN CALCULATION SHEETS

C.2.1. GIRDER A

Type	2	1=Type 2 AASHTO Girder, 2=Type 2 AASHTO Girder (1/2 scale), 3=46' Girder, 4
Length	18	

Pretension or Post-tension?	Pretension	if Post-tension, time after moist	
Low Relaxation Strands?	No	cure to prestress application?	
Tendon Type	1		

Dimensions (inches)

TYPE	Girder	D1	D2	D4	D5	D6	D7	B1	B2	B3	B4	B6
2	AASHTO Type II (half-scale) w/o Deck	22.5	3	1.5	3	3	12	6	9	3	1.5	3

Additional Loads

w_d (lb/ft)	0.00
P_l (kips)	0.00
Distance between supports (ft	9.000
Tributary width of girders (ft)	0

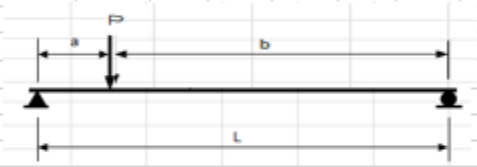

Stirrup Spacing

Location (ft)	0	0	0.667	5.4	9
Spacing (in)		1	2	4	6
A_v (in^2)	0.11				

Prestress Draping Strands

Drape Length (ft)	0
Drape Height (in.)	0
Strands Draped (#)	0

*Location from bottom of girder

Strand Location at Ends

Row (in.)	2	4	6	8	10	12	14	16	18	20	22	24
# Strands	0	2	0	0	0	0	0	0	0	0	0	0

Strand Location at Mid Span

Row (in.)	2	4	6	8	10	12	14	16	18	20	22	24
# Strands	0	2	0	0	0	0	0	0	0	0	0	0

Concrete Properties	
f'_{ci} (psi)	4000
f'_c (psi)	6000
Unit Weight (pcf)	150
Lightweight Coefficent, λ	1.00
Mild Steel Properties	
d' (in)	2
f_y (ksi)	60
A's (in2)	0.88
Prestress Properties	
Loss Method	Gross
f_{pu}	270
f_{py}	229.5
f_{pi}	186
Strand Type	0.52
Relative Humidity	70
E_{ps} (ksi)	28500

	Tendon Type
1	Gr. 270 Stress-Relieved Strand or Wire
2	Gr. 250 Stress-Relieved Strand or Wire
3	Gr. 240 or 235 Stress Relieved Wire
4	Gr. 270 Low-Relaxation Strand
5	Gr. 250 Low-Relaxation Wire
6	Gr. 240 or 235 Low-Relaxation Wire
7	Gr. 145 or 160 Stress Relieved Bar

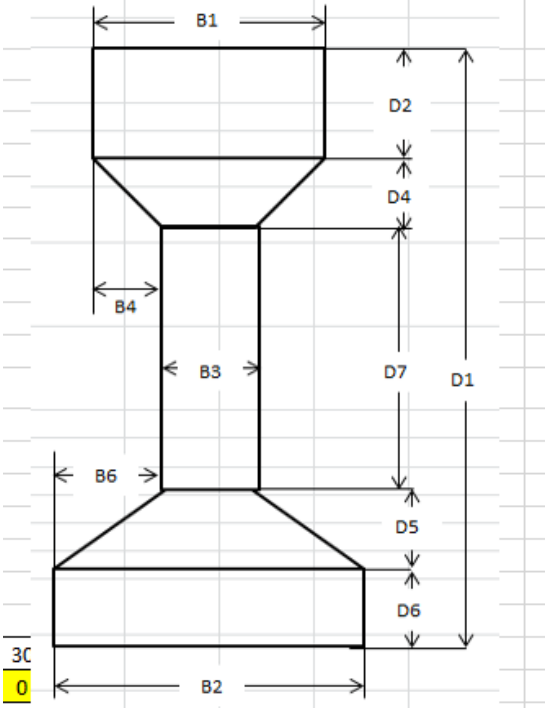

ACI Shear Capacity Calculation				
Properties				**Loadings**
Type	2			
cgs (in.)	4			
h (in.)	22.5			
d_p (in.)	18.50			
d' (in.)	2.00			
b_w (in.)	3			
w_d (k/ft)	0.110			
w_l (k/ft)	0.000			
P (kips)	62.365	62.365		
A_g (in^2)	105.75			
A_{ps} (in^2)	0.33			
L (ft) supports	9		**Simplified Shear**	
l_c (ft)	3.083333333		V_c (kips)	**41.43**
a (ft)	3.083333333		V_{min} (kips)	8.60
b (ft)	5.92		V_{max} (kips)	21.50
V_{de} (kips)	0		**Detailed Shear**	
$V_{d(-support)}$ (kips)	0.99140625		V_{ci} (kips)	26.14
$V_{d(+support)}$ (kips)	0.991		$V_{ci,min}$ (kips)	7
V_{dc} (kips)	-0.340		V_{cw} (kips)	23.7
M_{dc} (k-ft)	-0.523624674		**Final**	
V_{ue} 1 (kips)	40.99921296		V_c (kips)	23.66
V_{ue} 2 (kips)	21.36578704		V_s (kips)	30.525
V_{uc} (kips)	40.65956452546		**V_n (kips**	54.18
M_{cu} (k-ft)	125.8906153		**ϕV_n (kips)**	40.63522
V_i (kips)	40.999		**M_n (k-ft)**	126.4149
M_{max} (k-ft)	126.41424			

C.2.2. GIRDER C

Type	2	1=Type 2 AASHTO Girder, 2=Type 2 AASHTO Girder (1/2 scale), 3=46" Girder, 4
Length	18	

Pretension or Post-tension?	Pretension	if Post-tension, time after moist	
Low Relaxation Strands?	No	cure to prestress application?	
Tendon Type	1		

Dimensions (inches)

TYPE	Girder	D1	D2	D4	D5	D6	D7	B1	B2	B3	B4	B6
2	AASHTO Type II (half-scale) w/o Deck	22.5	3	1.5	3	3	12	6	9	3	1.5	3

Additional Loads

w_d (lb/ft)	0.00
P_l (kips)	0.00
Distance between supports (f	9.000
Tributary width of girders (ft)	0

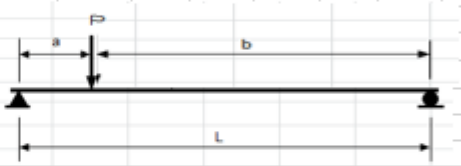

Stirrup Spacing

Location (ft)	0	0	0.667	5.4	9
Spacing (in)		1	2	4	6
A_v (in^2)	0.11				

Prestress Draping Strands

Drape Length (ft)	0
Drape Height (in.)	0
Strands Draped (#)	0

*Location from bottom of girder

Strand Location at Ends

Row (in.)	2	4	6	8	10	12	14	16	18	20	22	24
# Strands	0	2	0	0	0	0	0	0	0	0	0	0

Strand Location at Mid Span

Row (in.)	2	4	6	8	10	12	14	16	18	20	22	24
# Strands	0	2	0	0	0	0	0	0	0	0	0	0

Concrete Properties	
f'_{ci} (psi)	4000
f'_c (psi)	6000
Unit Weight (pcf)	150
Lightweight Coefficent, λ	1.00

Mild Steel Properties	
d' (in)	2
f_y (ksi)	60
A'_s (in2)	0.88

Prestress Properties	
Loss Method	Gross
f_{pu}	270
f_{py}	229.5
f_{pi}	202.5
Strand Type	0.6
Relative Humidity	70
E_{ps} (ksi)	28500

Time	
Days when prestress strands are released	1
Days when curing stops	1
Days from release that deck was placed	28
Days since girder batched	17155

ACI Shear Capacity Calculation				
Properties				**Loadings**
Type	2			
cgs (in.)	4			
h (in.)	22.5			
d_p (in.)	18.50			
d' (in.)	2.00			
b_w (in.)	3			
w_d (k/ft)	0.110			
w_l (k/ft)	0.000			
P (kips)	80.730	80.730		
A_g (in^2)	105.75			
A_{ps} (in^2)	0.434			
L (ft) supports	9		**Simplified Shear**	
l_c (ft)	3.083333333		V_c (kips)	**41.43**
a (ft)	3.083333333		V_{min} (kips)	8.60
b (ft)	5.92		V_{max} (kips)	21.50
V_{de} (kips)	0		**Detailed Shear**	
$V_{d(-support)}$ (kips)	0.99140625		V_{ci} (kips)	33.02
$V_{d(+support)}$ (kips)	0.991		$V_{ci,min}$ (kips)	7
V_{dc} (kips)	-0.340		V_{cw} (kips)	27.1
M_{dc} (k-ft)	-0.523624674		**Final**	
V_{ue} 1 (kips)	53.0725		V_c (kips)	27.13
V_{ue} 2 (kips)	27.6575		V_s (kips)	30.525
V_{uc} (kips)	52.73285156250		**V_n (kips**	57.65
Mcu (k-ft)	163.1165837		**ϕV_n (kips)**	43.23984
V_i (kips)	53.073		**M_n (k-ft)**	163.6411
M_{max} (k-ft)	163.6402083			

APPENDIX D.

INDIVIDUAL BRIDGE SITE VISITS

The following sections provide a detailed discussion of each site visit, and photos representative of observations for each entire bridge. Each photo includes a reference location within the bridge based on the numbering system described in Section 7.2. The bridges are listed in order of superstructure rating, from best to worst, and organized by ODOT field division.

D.1. FIELD DIVISION NO. 1

Field Division No. 1 (Figure D-1), located in eastern Oklahoma, includes Adair, Cherokee, Haskell, McIntosh, Muskogee, Okmulgee, and Wagoner counties. On April 17, 2015, four bridges were visited in Field Division No. 1, as detailed in the following.

Figure D-1: Field Division 1 Jurisdiction [49]

D.1.1. NBI# 24219, Indian Nation Turnpike & Co. Rd. E1095, Okmulgee County

This bridge was built in 1965, and is maintained by the Oklahoma Turnpike Authority. For this bridge, located at Indian Nation Turnpike (under[1]) & Co. Rd. E1095, the superstructure rating is 8, or very good condition.

The following highlights some key findings at this site:

- Bearing plates are expanding, and corroding (Figure D-2)

[1] For future reference, the first descriptor in the bridge's location, is the feature that is "under."

Figure D-2: Example of a corroding bearing plate (3W-S)

- Horizontal crack at 4W-S flange/web interface; and vertical crack (Figure D-3 and Figure D-4)

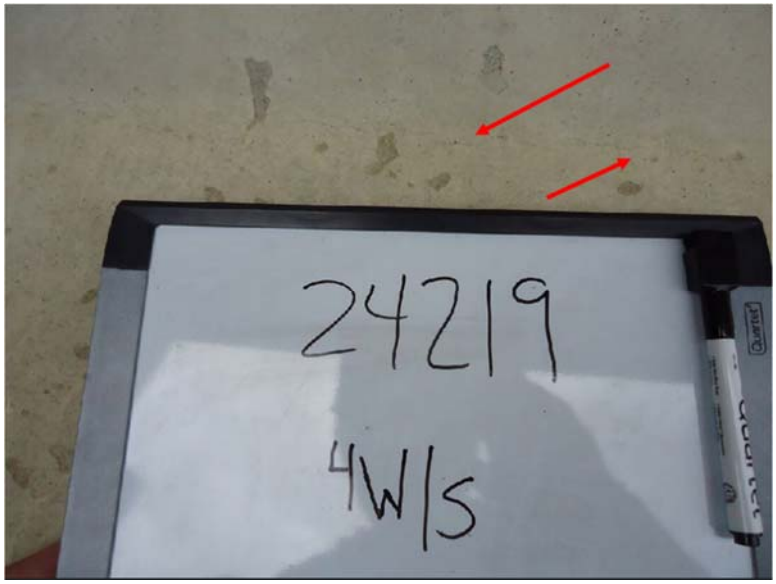

Figure D-3: Horizontal crack at top flange/web interface (4W-S)

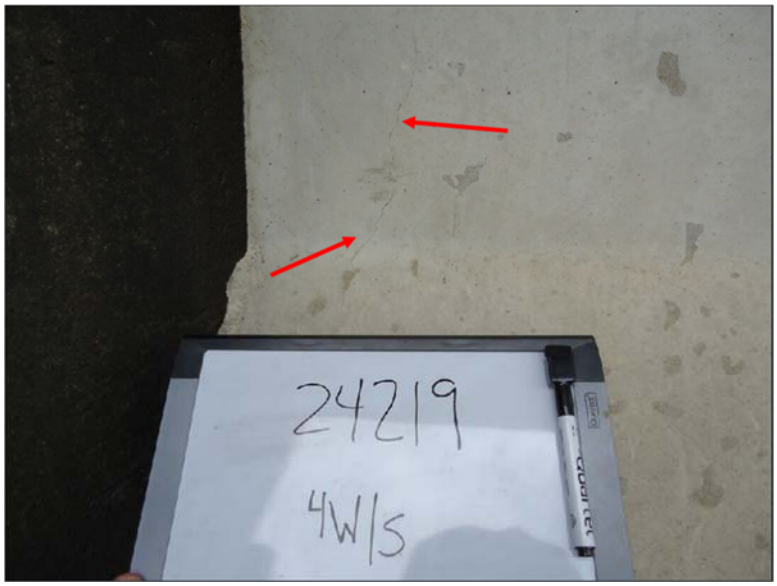

Figure D-4: Vertical crack from web through bottom flange (4W-S)

D.1.2. NBI# 19214, S.H. 150 & U.S. 69 SB, McIntosh County

This bridge was built in 1976, and is maintained by ODOT. The superstructure rating is 7, or good condition. The following highlights some key findings at this site:

- Corroded anchor bolts (Figure D-5)

Figure D-5: Corroded anchor bolt (1S-W)

- Underside of bridge deck corroded with exposed rebar (Figure D-6)

Figure D-6: Exposed rebar, showing insufficient concrete cover at end of bridge deck (1N-W)

- Example of concrete repair work likely to prevent further spalling of the concrete (Figure D-7). The repair seems to consist of mortar added to the surface of the existing girder end.

Figure D-7: Repaired concrete on girder end and corroded bolt (1S-W)

D.1.3. NBI# 19215, S.H. 150 & U.S. 69 NB, McIntosh County

The bridge was built in 1976, and is maintained by ODOT. The superstructure rating is 7, or good condition. The following highlights some key findings at this site:

- Diagonal cracking on the web of the beam (Figure D-8)

Figure D-8: Diagonal cracking on the web of the beam (3N-W)

- Repair to spalled back corner likely to prevent further spalling of the girder end (Figure D-9).

Figure D-9: Repair to spalled back corner (6N-W)

D.1.4. NBI# 15804, I-40 & Lotahwatah Rd. N41, McIntosh County

The bridge was built in 1963, and is maintained by ODOT. The superstructure rating is 5, or fair condition. The following highlights some key findings at this site:

- Back concrete diagonal crack in the beam (Figure D-10)

Figure D-10: Back diagonal crack in the beam end (3N-E)

- Separation at diaphragm and girder (Figure D-11)

Figure D-11: Separation at the diaphragm and girder end (1N-W)

D.2. FIELD DIVISION NO. 2

Field Division No. 2 (Figure D-12), located in southeastern Oklahoma, includes Atoka, Bryan, Choctaw, Latimer, Le Flore, McCurtain, Marshall, Pittsburg, and Pushmataha counties. On March 21, 2015, four bridges were visited in Field Division No. 2, as detailed in the following sections.

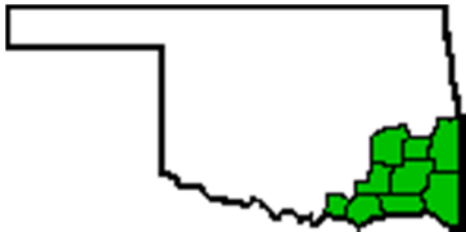

Figure D-12: Field Division 2 Jurisdiction [49]

D.2.1. NBI# 18554, S.H. 78 & U.S. 69 SB, Bryan County

The bridge was built in 1973, and is maintained by ODOT. The superstructure rating is 8, or very good condition. The following highlights some key findings at this site:

- Diagonal back corner cracking/spalling in the beam (Figure D-13)

Figure D-13: Spalled back corner of beam end (4E-N)

- Cracking and spalling at pipe interface with exterior of concrete girder (Figure D-14). It was not immediately clear the purpose of the pipe (e.g., drainage pipe, hole for diaphragm connection).

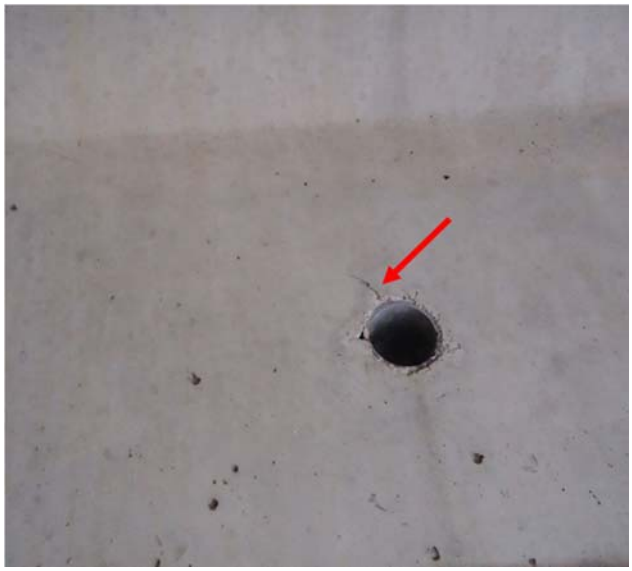

Figure D-14: Crack from interior pipe that runs through web of beam (4E-N)

- Diaphragm deterioration, exposed rebar showing corrosion (Figure D-15)

Figure D-15: Deterioration of an interior end diaphragm (6W-N); the diaphragm connects two interior beam ends

D.2.2. NBI# 18555, S.H. 78 & U.S. 69 NB, Bryan County

This bridge was built in 1973, and is maintained by ODOT. The superstructure rating is 8, or very good condition. The following highlights some key findings at this site:

- Spalling at pipe interface with exterior of concrete girder (Figure D-16)

Figure D-16: Spalling around pipe interface with exterior of concrete girder (3E-N)

- Heavily deteriorated anchor bolts (Figure D-17)

Figure D-17: Close-up of deterioration of anchor bolt, with necking at the top (4E-S). The pen is shown in the picture to illustrate the amount of necking occurring to the steel member.

- Hairline diagonal cracks from top flange/web interface towards embedded pipe (Figure D-18)

Figure D-18: Hairline diagonal cracks from top flange/web interface towards pipe on interior beam (5W-N)

- Back corner diagonal cracking in beam (Figure D-19)

Figure D-19: Back corner diagonal cracking of beam end (5W-S)

D.2.3. NBI# 17536, U.S. 271 & Indian Nation Turnpike, Pushmataha County

The bridge was built in 1969, and is maintained by the Oklahoma Turnpike Authority. The superstructure rating is 7, or good condition. The following highlights some key findings at this site:

- Spalling above support of corroding bearing plate, minor spalling horizontally along base of the girder, and cracking emanating from spalling location (Figure D-20 and Figure D-21)

Figure D-20: Corroded bearing plate and minor spalling above the bearing plate (1E-S)

Figure D-21: Diagonal crack in bottom flange of beam from corroding support (10W-N)

- Spalled back corner of girder and exposed prestressing strand ends (Figure D-22)

Figure D-22: Spalled back corner and exposed prestressing strands

D.2.4. NBI# 16606, S.H. 31/ U.P. R.R. & Indian Nation Turnpike, Pittsburg County

This bridge was built in 1965, and is maintained by the Oklahoma Turnpike Authority. The superstructure rating is 5, or fair condition. The following highlights some key findings at this site:

- Bottom of girders with exposed and deteriorating rebar and/or prestressing strands (Figure D-23)

Figure D-23: Exposed rebar due to spalled concrete on the bottom of an exposed, exterior girder (1N-E)

- Horizontal cracking along top flange/web interface (Figure D-24)

Figure D-24: Crack along intersection of the top flange and web

- Extremely corroded bearing plates (Figure D-25)

Figure D-25: Corroded, and deteriorated bearing plate (8N-E)

- Cracking near concrete/corroded bearing plate interface (Figure D-26)

Figure D-26: Cracking from corroded bearing plate into bottom flange (10S-W)

D.3. FIELD DIVISION NO. 3

Field Division No. 3 (Figure D-27), located in central Oklahoma, includes Cleveland, Coal, Garvin, Hughes, Johnston, Lincoln, McClain, Okfuskee, Pontotoc,

Pottawatomie, and Seminole counties. There was only one bridge that fell within the specified criteria, and that bridge was not inspected.

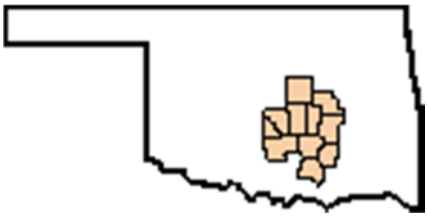

Figure D-27: Field Division 3 jurisdiction [49]

D.4. FIELD DIVISION NO. 4

Field Division No. 4 (Figure D-28), located in northcentral Oklahoma, includes Canadian, Garfield, Grant, Kay, Kingfisher, Logan, Noble, Oklahoma, and Payne counties. On October 24, 2015, three bridges were visited in Field Division No. 4, as detailed in the following sections.

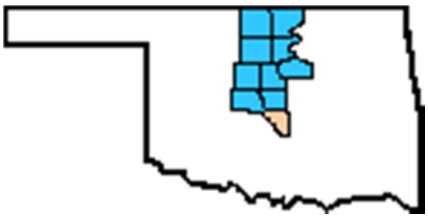

Figure D-28: Field Division 4 Jurisdiction [49]

D.4.1. NBI# 18497, Cimarron Turnpike & Co. Rd N3340, Pawnee County

This bridge was built in 1973, and is maintained by the Oklahoma Turnpike Authority. The superstructure rating is 7, or good condition. The following highlights some key findings at this site:

- Corroded bearing plate and resulting spalling above the support (Figure D-29)

Figure D-29: Corroded bearing plate and spalling along bottom of girder and girder end (3S-W)

- Spalling above the support and at end of girder (Figure D-28)

Figure D-30: Corroded anchor bolt and spalling along bottom of girder and girder end (5N-E)

D.4.2. NBI# 19028, U.S. 77 & Cimarron Turnpike, Noble County

This bridge was built in 1975, and is maintained by the Oklahoma Turnpike Authority. The superstructure rating is 7, or good condition. The following highlights some key findings at this site:

- Deterioration of girder and back wall due to moisture/water (Figure D-31)

Figure D-31: Deterioration of back wall and girder end due to moisture/water (1E-N). The exposed, exterior girder has a corroded bearing plate and spalling occurring at the end.

- Back corner spalled and prestressing strands exposed (Figure D-32)

Figure D-32: Exposed prestressing strands of an exposed, exterior girder (1W-N)

- Exposed prestressing strands and expanded, (“flaky”) bearing plates (Figure D-33)

Figure D-33: Corroded and flaky bearing plate (1W-S)

- Heavily corroded and broken anchor bolt (Figure D-34)

Figure D-34: Corroded anchor bolt that has been sheared in two (7E-S)

- Spalling above corroded bearing plates and missing anchor bolts (Figure D-35)

Figure D-35: Spalling above corroded bearing plate and missing anchor bolt (10E-S)

- Back corner diagonal cracking of beam end (Figure D-36)

Figure D-36: Back corner diagonal cracking on beam end (11W-S)

D.4.3. NBI# 19487, U.S. 64/U.S. 412 & S.H. 74, Garfield County

This bridge was built in 1978, and is maintained by ODOT. The superstructure rating is 6, or satisfactory condition. The following highlights some key findings at this site:

- Spalling and cracking at pipe in the web (Figure D-37)

Figure D-37: Spalling and cracking above pipe in web (1N-E)

- Diagonal crack in web toward bottom of girder from top of beam (Figure D-38)

Figure D-38: Diagonal crack in web from top flange towards bottom of beam (1N-W)

- Corroded anchor bolts (Figure D-39)

Figure D-39: Corroded anchor bolt (4S-E)

D.5. FIELD DIVISION NO. 5

Field Division No. 5 (Figure D-40), located in southwestern Oklahoma, includes Beckham, Blaine, Custer, Dewey, Greer, Harmon, Jackson, Kiowa, Roger Mills, Tillman, and Washita counties. Only one bridge in Division 5 fell within the specified criteria, and that bridge was not inspected.

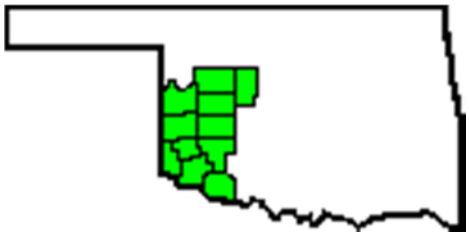

Figure D-40: Field Division 5 Jurisdiction [49]

D.6. FIELD DIVISION NO. 6

Field Division No. 6 (Figure D-41), located in northwestern Oklahoma (the Panhandle), includes Alfalfa, Beaver, Cimarron, Ellis, Harper, Major, Texas, Woods, and Woodward counties. There were no bridges that fell within the specified criteria in Division

6. Interestingly, the vast majority of bridges on the western side of the state (Divisions No. 5 and 6) were steel bridges, as opposed to concrete bridges.

Figure D-41: Field Division 6 Jurisdiction [49]

D.7. FIELD DIVISION NO. 7

Field Division No. 7 (Figure D-42), located in southcentral Oklahoma, includes Caddo, Carter, Comanche, Cotton, Grady, Jefferson, Love, Murray, and Stephens counties. On February 21, 2015, five bridges were visited in Field Division No. 7, as detailed in the following sections.

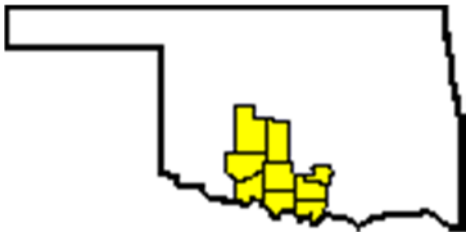

Figure D-42: Field Division 7 Jurisdiction [49]

D.7.1. NBI# 18793, UP R.R. & U.S. 62, Grady County

This bridge was built in 1963, and is maintained by ODOT. The superstructure rating is 8, or very good condition. The following highlights some key findings at this site:

- Back corner diagonal cracking and spalling (Figure D-43)

Figure D-43: Back corner diagonal crack of exposed, exterior beam (1E-N)

- Spalling above corroding bearing plate (Figure D-44)

Figure D-44: Corroded bearing plate and anchor bolt with spalling above the support (5E-S)

D.7.2. NBI# 18494, U.S. 81 & S.H. 7 EB, Stephens County

This bridge was built in 1973, and is maintained by ODOT. The superstructure rating is 8, or very good condition. The following highlights some key findings at this site:

- Back corner diagonal cracking (Figure D-45)

Figure D-45: Back corner diagonal cracking of exterior beam (1E-S)

- Spalling above corroded bearing plates (Figure D-46)

Figure D-46: Spalling above the corroded bearing plate (1W-N)

- Separation at diaphragm and girder interface (Figure D-47)

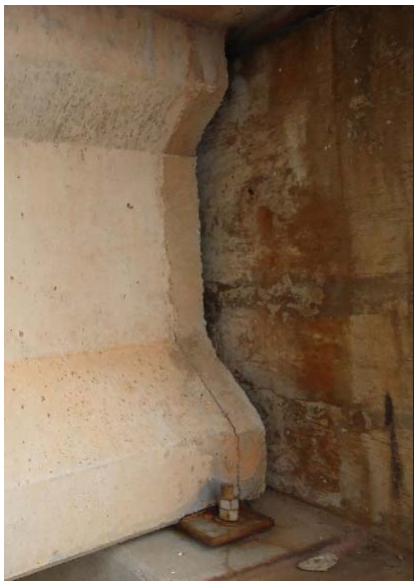

Figure D-47: Vertical separation of diaphragm and girder at interface (5E-S)

- Spalling and cracking at corroded bearing plate (Figure D-48)

Figure D-48: Corroded bearing plate and anchor bolt, with spalling and cracking above the corroded bearing plate (5W-N)

D.7.3. NBI# 15798, I-44 & Co. Rd. E1990, Cotton County

This bridge was built in 1963, and is maintained by ODOT. The superstructure rating is 7, or good condition. The following highlights some key findings at this site:

- Back corner spalled and exposed vertical rebar (Figure D-49)

Figure D-49: Exposed vertical rebar due to spalling at the end of exposed, exterior girder (1W-N)

- Concrete spalling at diagonal crack on back corner (Figure D-50)

Figure D-50: Spalling resulting from back corner diagonal crack (2E-N)

- Spalling at diaphragm and girder interface (Figure D-51)

Figure D-51: Spalling at diaphragm and girder interface (3W-N)

D.7.4. NBI# 18581, U.P. R.R./7th St. & S.H. 7 WB, Stephens County

This bridge was built in 1973, and is maintained by ODOT. The superstructure rating is 7, or good condition. The following highlights some key findings at this site:

- Heavily corroded bearing plate, anchor bolt, and nut; with spalling above support (Figure D-52)

Figure D-52: Corroded bearing plate, bolt, and nut along with spalling above the support of an exposed, exterior girder (1E-N)

- Corroded bearing plate and diagonal cracking at back corner (Figure D-53)

Figure D-53: Corroded bearing plate and spalling from a diagonal back corner crack with a maximum width of approximately four inches

- Corroded, flaky bearing plate (Figure D-54)

Figure D-54: Corroded, flaky bearing plate

- Vertical crack at back corner of girder and diaphragm interface (Figure D-55)

Figure D-55: Vertical crack along interface of girder end and diaphragm (1W-S)

D.7.5. NBI# 18582, U.P. R.R./7th St. & S.H. 7 EB, Stephens County

This bridge was built in 1973, and is maintained by ODOT. The superstructure rating is 7, or good condition. The following highlights some key findings at this site:

- Exposed rebar and corroded bearing plate (Figure D-56)

Figure D-56: Exposed rebar, corroded, flaky bearing plate, and spalling of concrete (5E-N)

- Vertical cracks near the top flange and web intersection in the beam (Figure D-57)

Figure D-57: Crack along the web of girder (5E-S)

- Diagonal back corner spalling and exposed, corroded prestressing strands (Figure D-58)

Figure D-58: Diagonal back corner spalling and exposed prestressing strands (5W-S)

- Corroded bearing plate and spalling back corner (Figure D-59)

Figure D-59: Corroded bearing plate, exposed rebar, and spalled back corner of girder (5W-S)

D.8. FIELD DIVISION NO. 8

Field Division No. 8 (Figure D-60), located in northeastern Oklahoma, includes Craig, Creek, Delaware, Mayes, Nowata, Osage, Ottawa, Pawnee, Rogers, Tulsa, and Washington counties. On October 17, 2015, three bridges were visited in Field Division No. 8, as detailed in the following sections.

Figure D-60: Field Division 8 Jurisdiction [49]

D.8.1. NBI# 18768, BNSF R.R./Co Rd & S.H. 167, Rogers County

This bridge was built in 1974, and is maintained by ODOT. The superstructure rating is 8, or very good condition. The following highlights some key findings at this site:

- Horizontal crack at top flange and web intersection for about a foot from beam and diaphragm interface (Figure D-61)

Figure D-61: Horizontal crack at top flange and web interface extending approximately one foot into the beam (1S-E)

- Corroded and necking anchor bolt and bearing plate covered with a protective coating (i.e. paint coating) (Figure D-62)

Figure D-62: Severely corroded anchor bolt and bearing plate covered with protective coating (1S-E)

- Crack at girder and diaphragm intersection (Figure D-63)

Figure D-63: Vertical crack at girder and diaphragm intersection (1S-W)

- Cracking in the back corner of the diaphragm (Figure D-64)

Figure D-64: Diagonal crack at back corner of girder end (2S-W)

D.8.2. NBI# 18076, S.H. 20 & U.S. 75 SB, Tulsa County

This bridge was built in 1971, and is maintained by ODOT. The superstructure rating is 5, or fair condition. The following highlights some key findings at this site:

- Vertical crack at girder/diaphragm intersection (Figure D-65)

Figure D-65: Vertical crack at girder/diaphragm interface (1N-W)

- Spalling at girder/diaphragm intersection (Figure D-66)

Figure D-66: Exposed rebar, back corner spalled (2S-W)

- Diagonal cracking from top flange/web intersection towards end of the beam (Figure D-67)

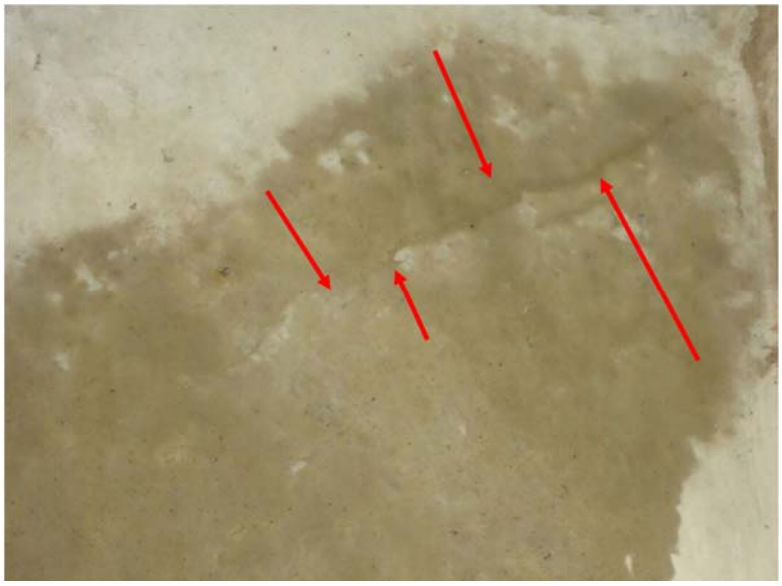

Figure D-67: Diagonal crack from top flange and web interface

- Underside corrosion on diaphragm between girders (Figure D-68)

Figure D-68: Corrosion on underside of end diaphragm with exposed and corroded rebar

D.8.3. NBI# 18077, S.H. 20 & U.S. 75 NB, Tulsa County

This bridge was built in 1971, and is maintained by ODOT. The superstructure rating is 5, or fair condition. The following highlights some key findings at this site:

- Cracking along top flange/web intersection, as well as cracks emanating from this region and going towards the bottom flange of the beam (Figure D-69)

Figure D-69: Diagonal web crack extending from top flange and web intersection (5N-W)

- Diagonal back corner spalling and exposed prestressing strands (Figure D-70)

Figure D-70: Diagonal back corner spalling of diaphragm and exposed prestressing strands (5S-W)

D.9. FHWA'S RECORDING AND CODING GUIDE FOR THE STRUCTURE INVENTORY AND APPRAISAL OF THE NATION'S BRIDGES

D.9.1 Superstructure Condition Ratings

N NOT APPLICABLE

9 EXCELLENT CONDITION

8 VERY GOOD CONDITION - no problems noted.

7 GOOD CONDITION - some minor problems.

6 SATISFACTORY CONDITION - structural elements show some minor deterioration.

5 FAIR CONDITION - all primary structural elements are sound but may have minor section loss, cracking, spalling or scour.

4 POOR CONDITION - advanced section loss, deterioration, spalling or scour.

3 SERIOUS CONDITION - loss of section, deterioration of primary structural elements. Fatigue cracks in steel or shear cracks in concrete may be present.

2 CRITICAL CONDITION - advanced deterioration of primary structural elements. Fatigue cracks in steel or shear cracks in concrete may be present or scour may have removed substructure support. Unless closely monitored it may be necessary to close the bridge until corrective action is taken.

1 "IMMINANT" FAILURE CONDITION - major deterioration or section loss present in critical structural components or obvious vertical or horizontal movement affecting structure stability. Bridge is closed to traffic but corrective action may put it back in light service.

0 FAILED CONDITION - out of service; beyond corrective action.

99 Miscoded Data